INEEL/EXT-04-01793

Multiphase Carbon-14 Transport in a Near-Field-Scale Unsaturated Column of Natural Sediments

Don T. Fox
Mitchell A. Plummer
Larry C. Hull
D. Craig Cooper

March 2004

Idaho National Engineering and Environmental Laboratory
Bechtel BWXT Idaho, LLC

INEEL/EXT-04-01793

Multiphase Carbon-14 Transport in a Near-Field-Scale Unsaturated Column of Natural Sediments

Don T. Fox
Mitchell A. Plummer
Larry C. Hull
D. Craig Cooper

March 2004

Idaho National Engineering and Environmental Laboratory
Idaho Falls, Idaho 83415

Prepared for the
U.S. Department of Energy
Assistant Secretary for Environmental Management
Under DOE Idaho Operations Office
Contract DE-AC07-99ID13727

ABSTRACT

Wastes buried at the Subsurface Disposal Area (SDA) of the Idaho National Engineering and Environmental Laboratory include activated metals that release radioactive carbon-14 (^{14}C) as they corrode. To better understand ^{14}C phase partitioning and transport in the SDA sediments, we conducted a series of transport experiments using ^{14}C (radio-labeled sodium carbonate) and nonreactive gas (sulfur hexafluoride) and aqueous (bromide and tritiated water) tracers in a large (2.6-m high by 0.9-m diameter) column of sediments similar to those used as cover material at the SDA. We established steady-state unsaturated flow prior to injecting tracers into the column. Tracer migration was monitored using pore-water and pore-gas samples taken from co-located suction lysimeters and gas ports inserted at ~0.3-m intervals along the column's length. Measurements of ^{14}C discharged from the sediment to the atmosphere (i.e., $^{14}CO_2$ flux) indicate a positive correlation between CO_2 partial pressure (pCO_2) in the column and changes in $^{14}CO_2$ flux. Though $^{14}CO_2$ diffusion is expected to be independent of pCO_2, changes of pCO_2 affect pore water chemistry sufficiently to affect aqueous/gas phase ^{14}C partitioning and consequently $^{14}C_2$ flux. Pore-water and -gas ^{14}C activity measurements provide an average aqueous/gas partitioning ratio, K_{ag}, of 4.5 (±0.3). This value is consistent with that calculated using standard carbonate equilibrium expressions with measured pH, suggesting the ability to estimate K_{ag} from carbonate equilibrium. One year after the ^{14}C injection, the column was cored and solid-phase ^{14}C activity was measured. The average aqueous/solid partition coefficient, K_d, (1.6 L kg^{-1}) was consistent with those derived from small-scale and short-term batch and column experiments using SDA sediments, suggesting that bench-scale measurements are a valid means of estimating aqueous/solid partitioning at the much larger spatial scale considered in these meso-scale experiments. However, limitations at the bench scale prevent observation of spatially- and temporally-varying parameters that affect contaminant transport in the natural environment. In addition to a temporally-variable $^{14}CO_2$ flux, in response to changes of pCO_2, we observed non-uniformities in K_{ag} and K_d that were not observed in bench-scale studies. Our results suggest that ^{14}C transport is effectively controlled by gas diffusion with minimal retardation by partitioning onto the solid phase, and little long-term retention. The implication for the SDA is that ^{14}C released via corrosion of activated metals is primarily transported by gas-phase diffusion rather than by liquid-phase advection. Calculations show that, because the atmospheric boundary is so much closer than the aquifer boundary at the SDA, most of the ^{14}C will diffuse upward to the atmosphere.

EXECUTIVE SUMMARY

Radioactive carbon released as gaseous $^{14}CO_2$ from wastes emplaced in the unsaturated surface (vadose zone) can be transported in both aqueous and gas form and may thus impact the overlying atmosphere and underlying groundwater. The presence of an estimated 500 Ci of ^{14}C buried in the Subsurface Disposal Area (SDA) of the Idaho National Engineering and Environmental Laboratory's Radioactive Waste Management Complex has led to analysis of ^{14}C release rates to both the air and water.

A radiological performance assessment completed in 2000 conservatively assumed that all ^{14}C released from the SDA would migrate downward, with infiltrating soil moisture, to eventually reach the Snake River Plain aquifer. Conversely, in assessing atmospheric exposures, all ^{14}C was assumed to migrate upward in the gas phase. In addition to these extreme simplifications of transport processes, the assessment omitted the effect of partitioning between aqueous and solid phases during liquid transport. To provide data for more realistic modeling of ^{14}C releases from the SDA, and thereby provide a stronger scientific basis for regulatory decisions, we conducted a series of transport experiments with conservative gas and liquid tracers as well as ^{14}C.

Parameters for contaminant transport modeling are typically based on bench-scale laboratory experiments. To determine flow and transport parameters at a spatial scale more applicable to the SDA, we conducted a set of transport experiments at unsaturated flow conditions in a near-field-scale (meso-scale) column filled with the sediment from the SDA. The column provides a physical model of vadose zone conditions at the SDA that allows us to monitor aqueous- and gas-phase transport over relatively long distances. Results of these transport experiments form the basis for future modeling efforts to determine the ability of transport parameters derived from small-scale and short-term experiments to predict ^{14}C behavior at scales approaching that of the field.

The meso-scale column consisted of a 2.9-m high by 0.91-m diameter stainless steel cylinder, sealed at both ends. The column contained approximately 1.7 m^3 of sediment, reaching a height of 2.6 m. We used SDA sediment, which is mineralogically relevant and assures geochemical variability commensurate with conditions at the SDA that have a major influence on ^{14}C partitioning and transport. The sealed headspace above the sediment was connected to an automated CO_2 and O_2 concentration monitoring and gas flow control system. Ambient air was circulated through the headspace at a rate of ~7 L min^{-1}. The circulation system allowed O_2 to diffuse into the sediment at atmospheric pressure and prevented accumulation of CO_2, thus providing a constant concentration boundary condition at the sediment surface (i.e., the sediment/atmosphere interface) for gas phase components. The column was instrumented at 30.5-cm intervals along its length. Instrumentation included four tensiometers, four water content reflectometers, eight water sampling lysimeters, eight gas sampling ports, and eight thermocouples.

The column was fitted with three separate injection arrays, each capable of injecting gas or liquid. Each array comprised twenty-four stainless steel tubes that could deliver fluid to evenly spaced locations in a horizontal plane within the

column. The uppermost array, on the sediment surface, supplied influent water. The two remaining arrays were situated within the sediment at 1.07 and 1.98 m above the bottom. Solutions for aqueous-phase transport experiments were injected into the middle array (at 1.98 m) to minimize nonuniform flow effects due to the periodic application of water at the sediment surface. Gas-phase tracers were injection into the bottom array (1.07-m height).

The sediment surface array used 24 syringe-pump-fed tubes to uniformly apply water to the surface at intervals of 40 min. This water was synthetic vadose zone water, formulated to approximate the composition of natural infiltrating soil moisture at the SDA. To limit microbial growth, the water was sterilized by autoclaving and treated with ultraviolet radiation immediately preceding application. Water application began at a hydraulic flux of ~5 L day^{-1}. After the wetting front reached the effluent lysimeters at the bottom of the column, the flux was reduced to ~1 L day^{-1} and held at that rate for the remainder of the experiments. To withdraw the infiltrating water, constant tension was applied to four 1.0-bar suction lysimeters located in a horizontal plane ~15 cm above the bottom. Thus, unsaturated hydraulic flow conditions in the column were maintained through application of a consistent flux at the top of the column and constant potential in the lysimeters. We tracked column water balance via periodic measurements of the column inflow, effluent water mass, mass removed for liquid sampling, and evaporative loss from the sediment surface. The latter was calculated from relative humidity measurements of ambient air and column headspace, combined with the headspace ventilation rate.

Prior to conducting the transport experiment with ^{14}C, we performed a set of experiments to examine the movement of water, gas, and conservative solute through the sediment. These experiments used injections of a highly insoluble gas tracer, sulfur hexafluoride, both before and after initiation of hydraulic flow, as well as injections of conservative liquid tracers, bromide and tritium, after reaching a quasi steady-state flow condition. Data from these experiments was used to estimate characteristics of the unsaturated flow system that would affect transport of ^{14}C, including average linear seepage velocity, dispersivity, and aqueous- and gas-phase diffusion coefficients. The ^{14}C transport test began with injection of an aqueous 1610 (± 16) microCi ^{14}C-labeled bicarbonate solution 0.6 m below the sediment surface, through the middle injection array (1.98-m height). For the next ~12 month, we monitored headspace and pore gas CO_2 and O_2 concentrations, sediment surface $^{14}CO_2$ flux, pore gas and pore water ^{14}C migration, pore water chemistry, sediment water content, hydraulic head and/or matric potential, and sediment temperature profiles. During the ^{14}C transport experiment, aqueous/gas ^{14}C partitioning ratios (K_{ag}) were calculated using two separate methods: aqueous and gas phase activity measurements and standard carbonate equilibrium expressions with measured pH. At conclusion of the ~12 month monitoring period, we cored the column and measured solid-phase ^{14}C sorption for calculation of the aqueous/solid ^{14}C sorption coefficient (K_d) and ^{14}C mass balance.

We determined seepage velocity and hydrodynamic dispersion coefficients by fitting analytical solutions to observed bromide (Br^-) breakthrough curves at each water sampling lysimeter. Consistent with the column's design, and despite its size, the Br^- breakthrough curves indicate that flow in the column was

effectively one-dimensional with an average linear seepage velocity of 0.52 cm day^{-1} and an aqueous diffusion coefficient of 1.8×10^{-5} cm^2 sec^{-1} during the transport experiments. We calculated an average hydraulic dispersion coefficient of 5.7×10^{-6} cm^2 sec^{-1} and average volumetric water content of 28% (± 3%). This water content range agrees well with the reflectometer and mass balance data. Additionally, the reflectometer and mass balance data indicate that this water content was relatively constant throughout the experiments. Calculated hydraulic dispersivity was effectively negligible, ranging from 0 to 7 mm. This is consistent with the results of Hull and Hohorst, who conducted saturated Br^- and tritium (^3H) transport tests with SDA sediment in 31-cm columns and found that dispersivity was on the order of 0.5 mm.

In aqueous systems ^3H readily partitions into water as ^3H_2O; therefore, the ^3H transport velocity is expected to be equivalent to that of the associated water. In our Br^- and ^3H tracer tests, the rate of ^3H transport was significantly slower than that of Br^-. Results of a second Br^- and ^3H tracer test indicate that anion (i.e., Br^-) exclusion was not the cause of this discrepancy. Furthermore, the good agreement between Br^- breakthrough curve results and independent water content determinations validates the use of Br^- data for flow system characterization. Therefore, the ^3H data was not considered in estimation of aqueous transport characteristics. We fit an analytical solution to observed ^3H breakthrough curves and calculated a ^3H sorption (retardation) coefficient, K_d, of ~0.08 mL g^{-1}. Measurement of ^3H retardation is significant because ^3H is commonly used as a conservative, nonreactive tracer in aqueous system studies. While the explicit mechanisms controlling ^3H retardation are unclear at this time, retardation is assumed due to the fixation of ^3H on clays and other common hydrated sediment minerals.

The sulfur hexafluoride (SF_6) gas tracer migrated rapidly through the column, with peak concentrations arriving at gas sampling ports located ~15-cm above and below the injection plane between 0.5 and 2 h following injection. Maximum late-time SF_6 concentrations are significantly higher in the second set of tests, performed under the higher water content associated with the quasi steady-state flow condition. This reflects the increased concentration gradient that developed in response to the increase in gas phase tortuosity with higher water content. Under this condition, least-squares analyses of SF_6 breakthrough curves using the standard Millington expression for gas phase tortuosity indicate a gaseous diffusion coefficient of 1.1×10^{-1} cm^2 sec^{-1} and a volumetric water content of 25%. The water content indicated by these analyses agrees relatively well with the other, more direct, measures of water content. Hull and Hohorst's experiments using air-dried SDA sediments in small-scale columns indicated that the reduction in the free-air diffusion coefficient due to tortuosity was slightly greater than that described by the Millington expression. However, we find that the standard Millington expression, with the commonly used *m* value of 7/3 or 2.33, provides an accurate description of SF_6 transport behavior in SDA sediments.

Gas-phase ^{14}C breakthrough curves at virtually all levels in the column display the same characteristic shape as the SF_6 curves, but lagged, consistent with gas-diffusion-dominated transport retarded by exchanges with other phases. ^{14}C concentrations at the nearest ports, for example, peaked after approximately

one day, as opposed to about an hour for SF_6. This $^{14}CO_2$ diffusion, with aqueous/gas phase exchange, allowed ^{14}C to distribute between pore-water and -gas volumes throughout the column within 7 days of the injection. Rapid diffusion produced a maximum $^{14}CO_2$ surface flux (22.37 microCi m^{-2} day^{-1}) within 25 days of the injection. After approximately one year, ^{14}C migration from the column was by surface flux (66.0%) and discharge of water from the bottom of the column (3.7%). Of the 21.6% of the total injected activity remaining in the column, 81.5% sorbed to the solid phase. Mass balances calculated from measurements of sorbed activity, aqueous and gaseous activities at the eight sampling levels, ^{14}C removed via gas and liquid samples, ^{14}C activity exiting via the lysimeters at the bottom, and ^{14}C venting into the headspace account for 93% of the injected ^{14}C activity. The inability to account for all of the injected activity is due to variability of sediment surface sample activities ($1.2 \times 10^{-4} \pm 33\%$ picoCi g^{-1} sediment), activity remaining within injection tubing, and cumulative measurement error.

In evaluation of $^{14}CO_2$ surface flux data, we observed a correlation between $^{14}CO_2$ flux and sediment temperature fluctuations. This observation is supported by a conceptual model that relates sediment temperature, which is the primary variable controlling microbial CO_2 production and thus CO_2 partial pressure (pCO_2) in the column, to the control of $^{14}CO_2$ aqueous/gas phase partitioning. Although gas-phase $^{14}CO_2$ diffusion is independent of pCO_2, changes in pCO_2 affect pore water chemistry (i.e., pH) sufficiently to affect aqueous/gas phase $^{14}CO_2$ partitioning. In the conceptual model, a decrease in sediment temperature causes a decline in pCO_2 that allows more partitioning of $^{14}CO_2$ to the aqueous phase than to the gas phase causing $^{14}CO_2$ flux out of the column to decrease. Conversely, an increase in sediment temperature allows more $^{14}CO_2$ to partition to the gas phase than to the aqueous phase and $^{14}CO_2$ flux out of the column increases. Therefore, a positive correlation between sediment temperature, pCO_2, and $^{14}CO_2$ flux is observed. Furthermore, microbial consumption of natural organic matter and O_2, and respiration of CO_2, produced an approximately exponential increase in pCO_2 with depth. The effect of nonuniform pCO_2 and, therefore, pH is observed in measurements of ^{14}C phase activity distributions.

^{14}C activity distributions are represented by aqueous/gas (K_{ag}) and aqueous/solid (K_d) partitioning ratios. We calculated K_{ag} using both aqueous- and gas-phase ^{14}C activity measurements at each co-located pore-water and -gas sampling port and measured pH with standard carbonate equilibrium expressions. K_d is calculated from aqueous- and solid-phase activity measurements at the time of coring. Typical pH values ranged from ~7.4 near the top of the column to ~6.9 near the bottom. This nonuniformity produced an increase in both K_{ag} and K_d near the top of the column, as significantly more ^{14}C was measured in the aqueous phase than in either the gas or solid phase near the top of the column. K_{ag} values ranged from ~9.0 near the top of the column to ~4.0 near the bottom. This range is consistent with that calculated using measured pH and standard carbonate equilibrium expressions, suggesting the ability to estimate K_{ag} based solely on carbonate equilibrium. K_d values range from 2.4 L kg^{-1} near the top of the column to 0.8 L kg^{-1} near the bottom. This range of K_d values is consistent with those derived from small-scale and short-term batch and column experiments using SDA sediments, suggesting that bench-scale measurements

are a valid means of estimating aqueous/solid partitioning at the much larger spatial scales considered in these meso-scale experiments. However, the effect of spatially-variable pH on K_{ag} and K_d was not observed in previous bench-scale studies. This is due largely to the size constraints of bench-scale studies. Subsequent to this report, the effect of a spatially-variable pH on ^{14}C transport parameters will be incorporated with numerical simulations of the column. These simulations form the basis for comparing meso-scale and bench-scale parameter estimations as well as extending ^{14}C behavior in those column studies to SDA transport problems.

Evaluations of our initial results suggest that ^{14}C transport in the column may be described by reactive diffusive transport in the gas phase with negligible aqueous phase transport. As estimated infiltration rates at the SDA are lower than that maintained in the column, gas movement also probably dominates ^{14}C transport at the SDA. Whether or not that includes an advective component, the flux to the atmosphere would be expected to be greater than the flux to the aquifer. Not only are these experimental conditions directly applicable to the vadose zone environment at the SDA, the sediment used is largely typical of the arid western United States. Therefore, the findings of this study may be useful for other vadose zone waste disposal sites where contaminant risk assessments or remedial efforts are under consideration.

In addition to describing ^{14}C behavior and transport model parameters, a secondary goal of this study was to identify the challenges of operating an unsaturated flow column at the meso scale. To constrain system variables, we sought to measure flow and transport parameters and ^{14}C migration under steady-state geochemical and hydraulic conditions. No significant challenges were encountered to prevent these measurements. However, establishing and maintaining steady-state conditions required consideration of four primary factors: excessive leaching of salts, stabilization of the hydraulic potential gradient, adequate sediment temperature control, and long-term depletion of microbial substrate.

Though an initial high infiltration rate minimized the time required to remove excess dissolved salts (i.e., nitrate) and to establish unsaturated flow, an extended period of steady hydraulic flux was needed to stabilize the hydraulic potential gradient following the initial high flux period. Stabilizing pore water chemistry (i.e., dissolved inorganic species) and establishing a quasi steady-state hydraulic potential gradient required 397 days. Quasi steady state was defined primarily by lysimeter properties and the hydraulic conductivity of sediments used ($K_{sat} \cong 4\text{x}10^{-5}$ cm sec^{-1}).

Sediment temperature and the availability of microbial substrate (i.e., easily metabolized organic carbon) affect microbial CO_2 production, which in turn is the primary variable affecting pH and $^{14}CO_2$ phase partitioning and transport. Due to rapid $^{14}CO_2$ discharge from the column, the long-term depletion of microbial substrate was relatively insignificant in these experiments. However, substrate depletion may impact studies sensitive to long-term pH and/or pCO_2 changes, such as the study of uranium mobility. Therefore, long-term reactive transport studies may find it necessary to control microbial substrate. Conversely, short-term temperature fluctuations produced significant fluctuations of $^{14}CO_2$

flux from the column. Therefore, as a spatial variable, pH affects K_{ag} and K_d uniformity, so a temperature-induced and temporally-variable pH should be considered when assessing ^{14}C transport in the near subsurface where variation of temperature with season and/or climate has the potential to affect K_{ag} and K_d.

Though considerable cost and time are required for meso-scale experiments, they provide a valuable means of observing complex behavior under conditions applicable to the field with control that is not possible in the field. In this study, we observed nonuniformities of K_{ag} and K_d that demonstrated the ability of meso-scale experiments to represent spatially-variable conditions that affect contaminant transport in the natural environment. Such transport parameters are typically measured with bench-scale experiments due to cost. However, the consistency of transport parameter estimations from previous bench-scale experiments and our meso-scale experiment demonstrates the value of meso-scale methods for extending bench-scale understanding to transport problems at the SDA and elsewhere.

ACKNOWLEDGEMENTS

The authors wish to thank Carolyn Bishop, Tim Kaser, Joe Lord, and Terri Nelson-Ireland for their commitment to the successful completion of this study.

CONTENTS

ABSTRACT iii

EXECUTIVE SUMMARY v

ACKNOWLEDGEMENTS xi

1. INTRODUCTION 1

2. EXPERIMENTAL DESIGN 3

3. MATERIALS AND METHODS 5

3.1 Column Construction and Packing 5

3.1.1 Device and Instrument Placement 5
3.1.2 Sediment Characteristics 7

3.2 Water Flow 13

3.2.1 Water Preparation and Composition 13
3.2.2 Establishing and Maintaining Unsaturated Flow 14

3.3 Sampling and Analysis 15

3.3.1 Water 15
3.3.2 Gas Concentration Measurements 17
3.3.3 Water Content Determination 19

3.4 Tracer Preparation, Injection, and Analysis 24

3.4.1 Sulfur Hexafluoride 24
3.4.2 Lithium Bromide 24
3.4.3 Uranium, Carbon-14, and Tritium Injection 25

4. RESULTS AND DISCUSSION 30

4.1 Hydro-Chemical Characterization 30

4.1.1 Water Content and Bulk Density 31
4.1.2 Water Chemistry 37
4.1.3 CO_2 and O_2 Gas Concentration Monitoring 44

4.2 Biological Assays 46

4.3 Tracer, Carbon-14, and Uranium Transport 46

4.3.1 Gas Tracer—Sulfur Hexafluoride 46
4.3.2 Aqueous Tracers—Bromide and Tritium 48
4.3.3 Carbon-14 Transport 52

5. CONCLUSION 62

6. REFERENCES 65

Appendix A—Measurement Accuracy 67

Appendix B—Sample Preparation Procedures 73

FIGURES

1. Relative locations of the INEEL, SDA/RWMC, and Snake River Plain aquifer 2

2. Timeline of key events in this research 4

3. Meso-scale column after packing (left) and during experiment (right) 6

4. Delivery point locations for injection arrays (plan view) 7

5. Elevation view of device placement. Note, the absolute bottom is 259.08-cm below the column surface. While level numbers indicate distance upward from the absolute bottom, Level "0" is actually at the mid-point between Level 1 and the absolute bottom. 8

6. Placement of monitoring and sampling devices at each level (plan view) 9

7. Syringe pump system for infiltration water delivery. Syringes and tubing are shown without pump motor housings. 15

8. Pore water pH measurement using inline electrode. Stainless steel lysimeter tubing and shut off valves are shown extending from the column 16

9. Linear fits used for low- and high-range CO_2 measurement corrections. Data points represent average gas standard measurements 19

10. Column coring for gravimetric water content and solid phase ^{14}C activity determinations 20

11. Injection of the ^{14}C, tritium, and uranium cocktail solution 26

12. Influent and effluent flow rates with effluent lysimeter head 33

13. Mass balance based cumulative volumetric water content 33

14. Moisture characteristic curve (a) and tensiometer and effluent lysimeter hydraulic heads (b) 34

15. Reflectometer (TDR probe) data. (a) volumetric water content and effluent-lysimeter hydraulic head, (b) wetting/dissolved-salts front breakthrough curves recorded by TDR probes, and (c) electrical conductivity time series 36

16. Aqueous chemistry and sediment CO_2 gas profiles (legend on next page) 42

17. Average CO_2, O_2, and pH profiles during ^{14}C transport study (dotted lines represent gas concentration ranges during the ~107 week study) 44

18. Sediment gas CO_2 and O_2 concentration time series at each column level 45

19. Bulk CO_2 surface flux. 45

20. SF_6 concentration in primary and replicate tests at packing (~10%) and experimental (~30%) water contents 47

21. Comparison of primary SF_6 tests at packing (~10%) and experimental (~30%) volumetric water content. (characters = ~30% test; lines = ~10% test) 47

22. Least-squares fit of SF_6 breakthrough curves at ~30% volumetric water content (i.e., the water content during transport study) 49

23. Bromide (Br^-) breakthrough curves and CXTFIT2 fit 50

24. Bromide (Br^-) and tritium (^3H) breakthrough curves 51

25. Measured sediment gas ^{14}C breakthrough curves at all eight column levels 52

26. ^{14}C sediment gas (a) and sediment water (b) activity profiles 53

27. ^{14}C surface flux (a), CO_2 surface flux (b), barometric pressure (c), and average sediment temperature (d) time series 55

28. Early time aqueous/gas phase partition ratios (K_{ag}) based on ^{14}C activity partitioning (a) and carbonate equilibrium (b) with pH (c) 56

29. Solid phase ^{14}C activity profile at end of study 57

30. Aqueous and gas phase ^{14}C activity profiles at end of study 58

31. Graphic representation of ^{14}C activity mass balance 59

32. K_d, K_{ag} (a), pH (b), bicarbonate alkalinity (c), and CO_2 (d) profiles at time of coring 60

TABLES

1. Column packing mass and bulk densities 6

2. Measurement of device locations 10

3. Measurement of initial (packing) water content, dry bulk density, wet bulk density, and porosity at time of column packing 11

4. Sediment drainage characteristics, from saturation 11

5. Unsaturated hydraulic properties 12

6. Saturated hydraulic conductivity 12

7. Bulk mineralogy of SDA sediments 12

8. General clay size fraction (<75 μm) SDA mineralogy 12

9. Surrogate vadose zone water components 13

10. Surrogate vadose zone water ion concentrations and chemistry 13

11. Average measured values of gas standards used for low- and high-range CO_2 measurement corrections 18

12. Tensiometer pressure transducer calibration expressions 22

13. Summary of water content determination by four independent methods 30

14. Water content determinations of porthole and core samples 31

15. Core sample bulk density determinations 32

16. Water chemistry and pore gas CO_2 concentration profiles relative to Br^- and isotope injections 38

17. pH, bicarbonate alkalinity, and CO_2 six days prior to ^{14}C injection 41

18. Average pH, CO_2, O_2, and bicarbonate profiles during transport study 41

19. Dissolved carbon results 43

20. Transport parameters used to model SF_6 and Br^- tracer breakthrough 49

21. Summary of transport parameters determined from CXTFIT2 analysis of conservative tracer tests 50

22. Sediment gas and sediment water ^{14}C activity time series 53

23. ^{14}C and bulk CO_2 surface flux data 54

24. Solid phase ^{14}C activity measurements 50 weeks after ^{14}C injection 57

25. Aqueous, gas, and solid phase ^{14}C activity measurements at end of study 58

26. ^{14}C activity injected, released, removed, and retained (mass balance determination) 59

27. K_d, K_{ag}, pH, CO_2, and bicarbonate measurements at time of coring 61

Multiphase Carbon-14 Transport in a Near-Field-Scale Unsaturated Column of Natural Sediments

1. INTRODUCTION

Since the 1950s, radioactive and hazardous wastes have been buried at the 40-hectare Subsurface Disposal Area (SDA) in the Idaho National Engineering and Environmental Laboratory's (INEEL) Radioactive Waste Management Complex (RWMC). Figure 1 shows the relative locations of the INEEL, SDA/RWMC, and the Snake River Plain aquifer. Wastes buried at the SDA include approximately 500 curries of carbon-14 (^{14}C) in materials such as beryllium reflector blocks and reactor core pieces (Case et al. 2000, McCarthy et al. 2000). As the beryllium reflector blocks (~20% of the total ^{14}C inventory) corrode, they release ^{14}C as carbon dioxide ($^{14}CO_2$). This released ^{14}C is the focus of a Comprehensive Environmental Response, Compensation, and Liability Act (CERCLA) risk assessment and a radiological performance assessment ordered by the Department of Energy. Current methods of assessing risk and performance assume, when considering the aquifer, that all the ^{14}C released will migrate downward, in a liquid and, when considering the atmosphere, that it will all migrate upward, as gas. This simplification ignores partitioning among solid, liquid, and gas phases in the unsaturated subsurface (vadose zone). While solid and liquid phase partitioning retard ^{14}C migration, gas phase partitioning is expected to increase vadose zone ^{14}C mobility (Thorstenson et al. 1983). Thus, a more realistic prediction of vadose zone ^{14}C migration would include multiphase partitioning and the effect of geochemistry on partitioning and transport.

Our primary goal was to define the relationships between multiphase partitioning and migration of ^{14}C within unsaturated SDA sediments at spatial-temporal scales sufficient to observe partitioning effects. A secondary goal was to identify the complications in operating an unsaturated flow column at a scale approaching that of the field (i.e., meso scale). We examined the movement of ^{14}C, water, gas, and conservative tracers in a meso-scale column of sediment similar to that used as SDA backfill, a playa-derived calcareous silty-clay. Our results will be used to calibrate contaminant transport models used to estimate ^{14}C inventories, assess risk, and evaluate remedial alternatives at active and inactive SDA waste burial sites. While these experimental conditions are directly applicable to the vadose zone environment at the SDA, the sediment used is largely typical of the arid western United States. Therefore, our findings may be useful for other vadose zone waste disposal sites where ^{14}C risk assessments are performed.

This report describes our experimental procedures, presents the results, and estimates ^{14}C specific factors, such as aqueous/gas (K_{ag}) and aqueous/solid (K_d) partitioning parameters, as well as factors that describe more general controls on the advective and diffusive transport of aqueous and gas phase contaminants.

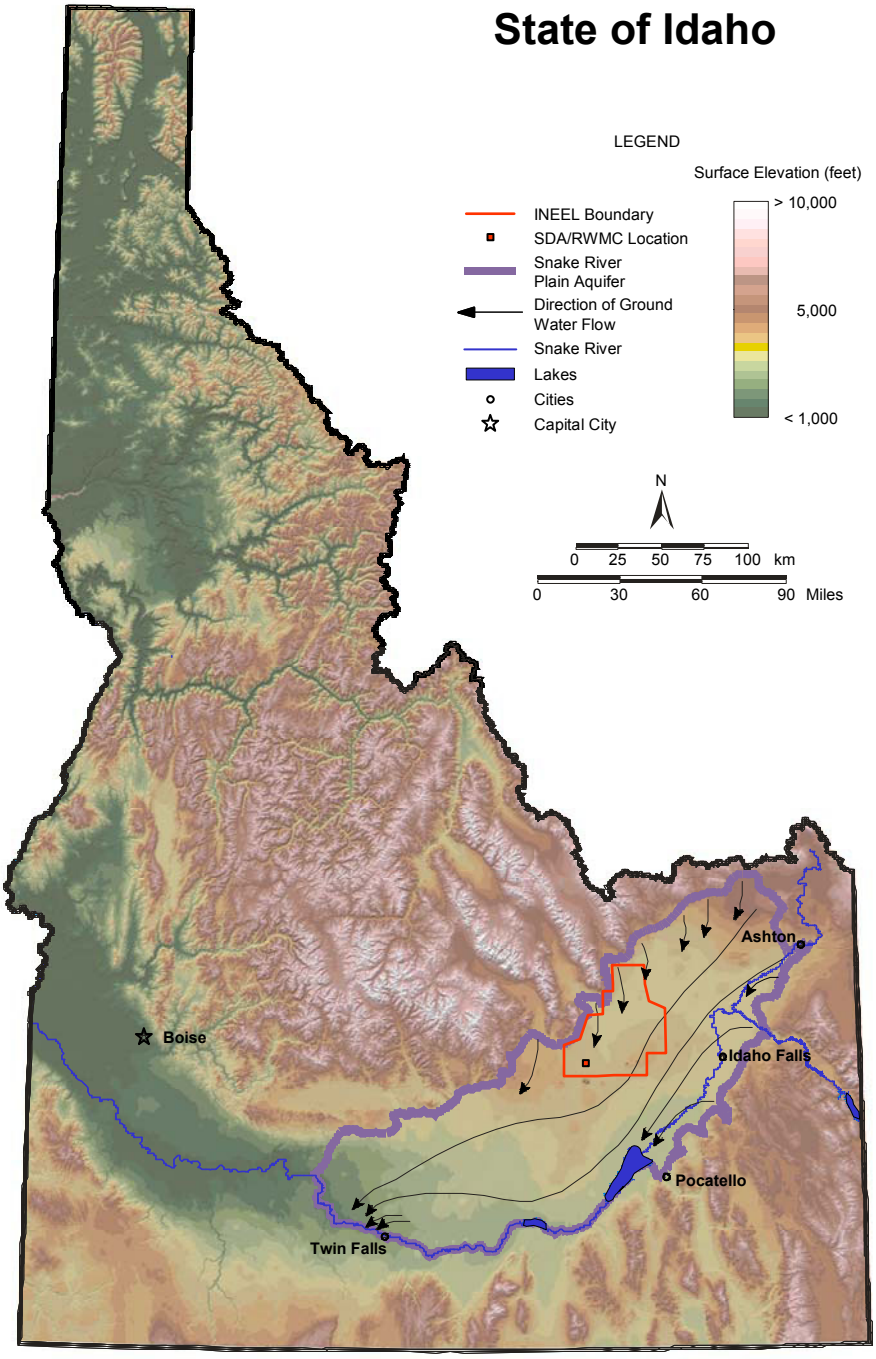

Figure 1. Relative locations of the INEEL, SDA/RWMC, and Snake River Plain aquifer.

2. EXPERIMENTAL DESIGN

We built a meso-scale column of SDA sediment and examined the movement of ^{14}C, water, gas, and conservative tracers. The column size—2.6-m high by 0.9-m diameter—was large enough to replicate field conditions while limiting the time required for data generation. We expected it to achieve proposed saturation conditions (~70%) in 300 to 500 days. Using SDA sediments (playa-derived calcareous silty-clay) was not only mineralogically relevant, it also assured an active microbial community producing a sediment-gas CO_2 profile commensurate with vadose zone conditions at the SDA.

The column's ends were sealed to form an enclosed headspace over the sediment surface; ambient air was circulated through the headspace to prevent accumulation of CO_2 and provide a constant concentration boundary condition at the sediment surface. Surrogate vadose zone water was applied to 24 evenly-distributed locations across the sediment surface. Downward unsaturated flow was maintained by vacuum applied to suction lysimeters located at the bottom of the column.

The column was instrumented in 30-cm intervals along its length with pore gas and pore water sampling ports. Four data and sample collection systems were used. The first system monitored hydrologic and temperature profiles. The second measured pH under nitrogen gas as water samples were taken (i.e., in situ pH). The third, an automated system, measured CO_2 and O_2 concentrations of ambient, headspace, and sediment gases. The fourth system captured headspace CO_2 gas for ^{14}C analysis.

As these systems indicated the approach of hydraulic and geochemical steady state, we performed experiments to estimate characteristics of the unsaturated flow system that affect ^{14}C transport, including average linear seepage velocity, dispersivity, and aqueous- and gas-phase tortuosity. These experiments included an infiltration test; injections of a highly insoluble gas tracer (sulfur hexafluoride, SF_6), both before water infiltration and after achieving steady-state hydraulic flow; and injection of conservative liquid tracers (tritium and lithium bromide) after reaching steady-state hydraulic flow. We injected 1610 (± 16) microCi of radiolabeled bicarbonate (^{14}C) into the column and monitored it for 350 days, after which we took core samples and measured solid phase ^{14}C sorption. A timeline of key events, relative to the start of water infiltration on July 11, 2001, is given in Figure 2. Boundary conditions for this work are listed below.

Effective column height (between water application and extraction)	2.44 m
Headspace	0.2 m^3; air was circulated through the headspace at ~7 L min^{-1}
Influent water	Average applied hydraulic flux of 0.93 L day^{-1} during ^{14}C tracer study; applied at 24 surface locations; average calculated seepage velocity of ~0.5 cm day^{-1} sustained by suction lysimeters at extraction point
Effluent water	Average extracted hydraulic flux of 0.74 L day^{-1} during ^{14}C tracer study

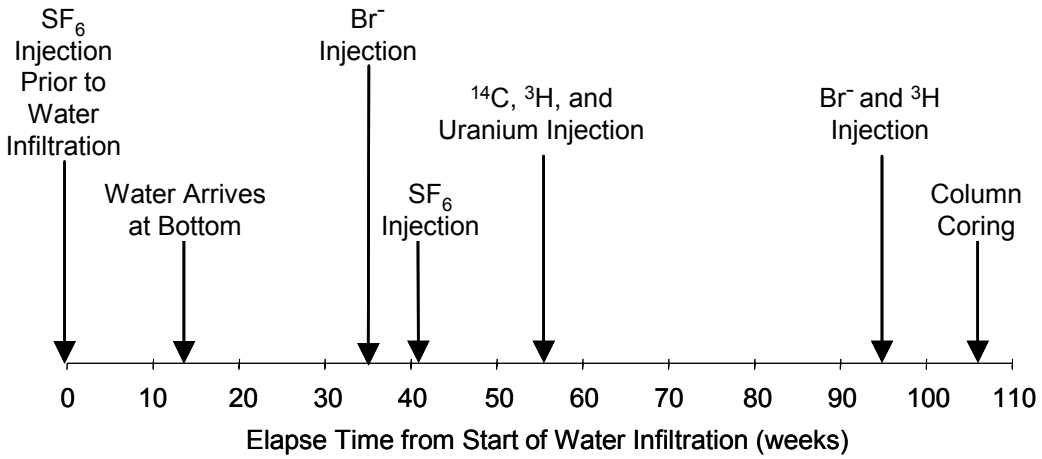

Figure 2. Timeline of key events in this research.

3. MATERIALS AND METHODS

This chapter describes each component of the study, from construction of the column to monitoring of injected tracers. We begin with column construction and packing, which includes the location of sampling, sensing, and injecting devices as well as soil characteristics. Next, we describe the methods used to prepare surrogate vadose zone water and the water and gas analysis methods. Then the process and systems used to establish and maintain unsaturated flow are described, followed by the methods used to monitor and determine soil water content. Finally, we outline tracer preparation, injection, and analysis. (The relative accuracies of analytic methods described in this chapter are given in Appendix A.)

3.1 Column Construction and Packing

Two 2.9-m high by 0.9-m diameter stainless steel (ASTM 240) cylinders were constructed in 1998.[a] Our experiment used one of these cylinders, which was located in the INEEL Engineering Demonstration Facility (IEDF). In 1999, the cylinder was packed with sediment from the Long Term Corrosion Test berm at the SDA that is representative of sediments used to backfill pits and trenches at the SDA. Sensors and sampling devices were placed in the sediment column during packing. The column was not used from 1999 to 2001. During this time, the headspace was continually purged with atmospheric air to maintain the exchange of atmospheric O_2 and microbially-generated CO_2 to and from the sediment, respectively. This study began in July 2001.

To facilitate homogenous packing of the cylinder, large fragments of plant roots were removed by passing the sediment through a 13-mm sieve. Only organic debris was removed, so the column represented SDA surface sediment particle sizes and mineral composition. The sieved sediment was placed in 208-L steel drums. The drums were sealed, then transported to the meso-scale column test site (IF-IEDF-E4, Bldg. 657). Air-dry sediment was transferred from the drums to the experimental cylinder using 19-L plastic buckets. The weight of sediment in each bucket was recorded. The sediment was manually compacted in ~15-cm lifts. Lift surfaces were scarified to avoid layering or segregation of soil by particle size prior to placing the next lift. Bulk density was calculated for the weight and volume of each lift. Sediment mass and bulk densities are presented in Table 1. *In situ* sensors and sampling devices were positioned on scarified surfaces; their tubes and/or wires were passed through adjacent cylinder portholes, which were sealed prior to placing the next lift. Portholes not used by devices were used as access for extracting sediment samples. The cylinder was filled to within 30.5-cm of the top flange, resulting in a 2.6-meter sediment column. A 0.2 m^3 headspace was created by sealing a 1.9-cm thick Plexiglas cover to the cylinder's top flange with silicone adhesive and C-clamps. Gas ports were positioned on opposing sides to allow atmospheric air and head gasses to mix prior to being evacuated from the headspace. The column was leak tested by applying ~34 kPa of gas pressure to the headspace. The column leaked down to ~14 kPa over a 10-hour period. Pictures of the column just after packing and during the study are given in Figure 3.

3.1.1 Device and Instrument Placement

The column was fitted with one influent water array, at the column surface, and two tracer injection arrays below the surface. Each array consists of a bundle of 24 stainless steel tubes (1.6-mm ID) that pass into the column through a 7-cm long stainless steel port (2.54-cm ID). The space between the tube bundle and the port's inside surface was sealed with epoxy. Within the column, the tubes spread out in a plane

a. LMITCO design drawing 454090, Lysimeter Mechanical Design Vessel Assembly.

Table 1. Column packing mass and bulk densities.

Column Level	Mass of Dry Sediment in Lift, adjusted for moisture (kg)	Dry Bulk Density (g cm^{-3})	Average Lift Dry Bulk Density (g cm^{-3})
1	128.1	1.28	1.39
	150.5	1.50	
2	137.9	1.38	1.20
	102.6	1.03	
3	125.2	1.25	1.26
	126.7	1.27	
4	118.7	1.19	1.28
	136.7	1.37	
5	123.9	1.24	1.26
	127.6	1.35	
6	135.2	1.57	1.46
	156.8	1.38	
7	137.9	1.29	1.34
	129.6	1.31	
8 to surface	130.9	1.22	1.26
	273.6	1.36	1.36
Average Lift Density			1.31 (± 0.05)
Total Sediment Mass	2241.9		

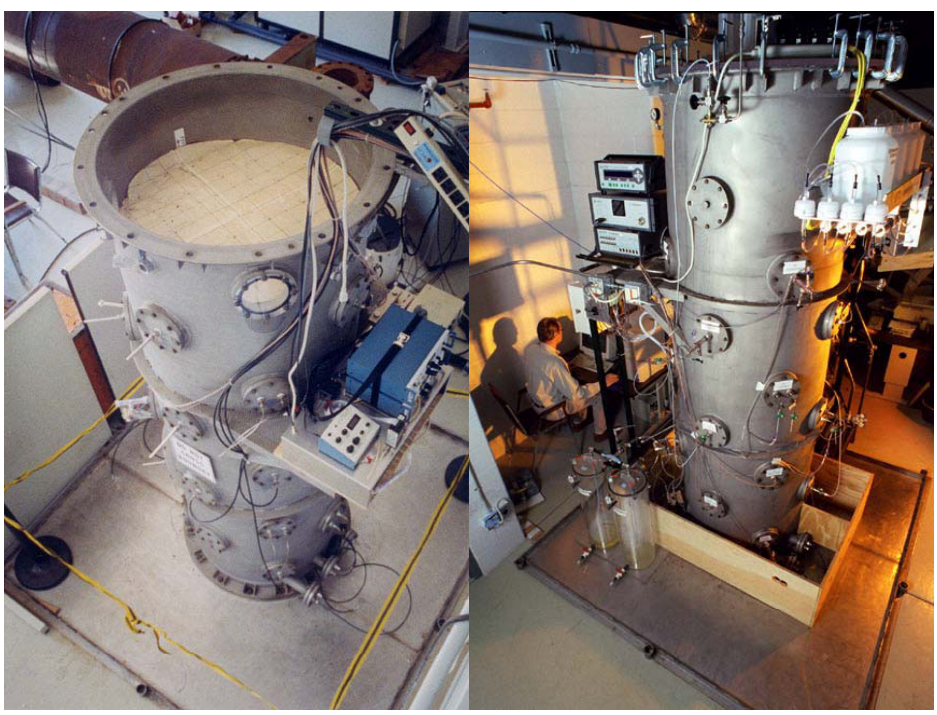

Figure 3. Meso-scale column after packing (left) and during experiment (right).

parallel to the sediment surface. The tube ends are placed as a grid with minimum intersection separation distances of 15 cm. The end point (i.e., delivery point) of each tube was recorded relative to numbers affixed to the tube-end extending outside of the column (see Figure 4).

The column was fitted with various devices for monitoring conditions and extracting samples. Drawings of the column with the vertical and circumferential placement of devices are given in Figures 5 and 6; the positions of each type of device are listed in Table 2.

3.1.2 Sediment Characteristics

To a large extent, the physical, mineral, and biological characteristics of a soil control transport. This section provides a brief discussion of the hydraulic characteristic of the sediment used in this study along with a general mineralogy description of surface sediments common to INEEL's SDA.

3.1.2.1 Hydraulic Properties. Water content, bulk density, and porosity determinations were performed, at the INEEL, for 265 sediment samples taken from 16 of the 18 drums of sediment used to pack the column. Standard methods and laboratory procedures for volume and mass measurements were used to determine water contents (ASTM D 2216-98) and bulk densities. Porosity was calculated using an average bulk density of 1.31 g cm^{-3} and an assumed particle density of 2.65 g cm^{-3}. Independent laboratory[b] determinations of water content, bulk density, porosity, saturated drainage characteristics,

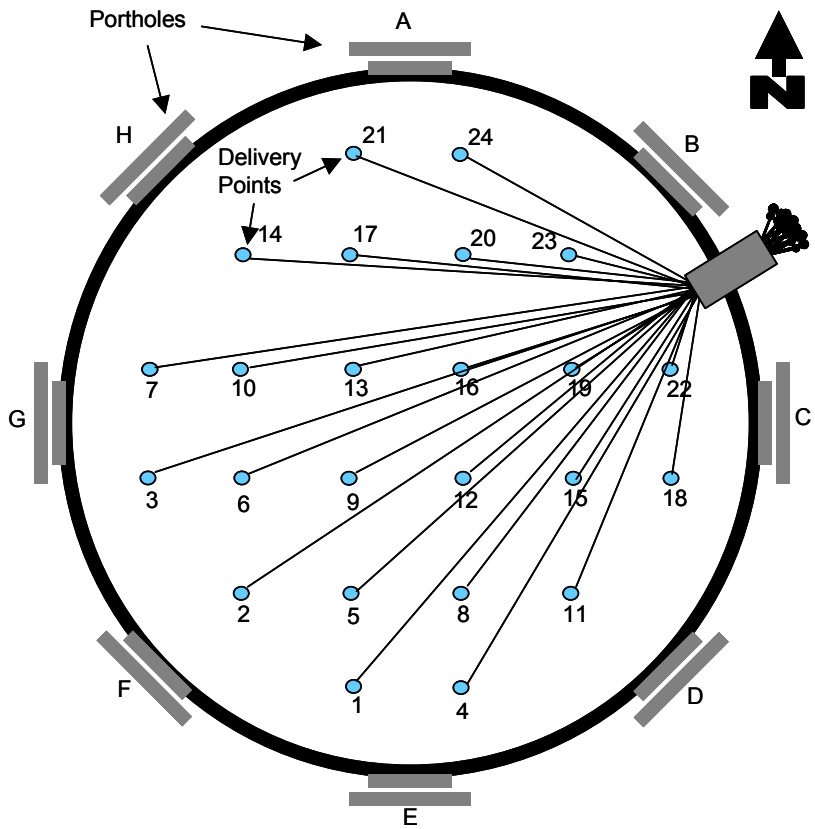

Figure 4. Delivery point locations for injection arrays (plan view). Letters A through H indicate geographic location.

b. D. B. Stevens, Albuquerque, N.M., January 22, 2002.

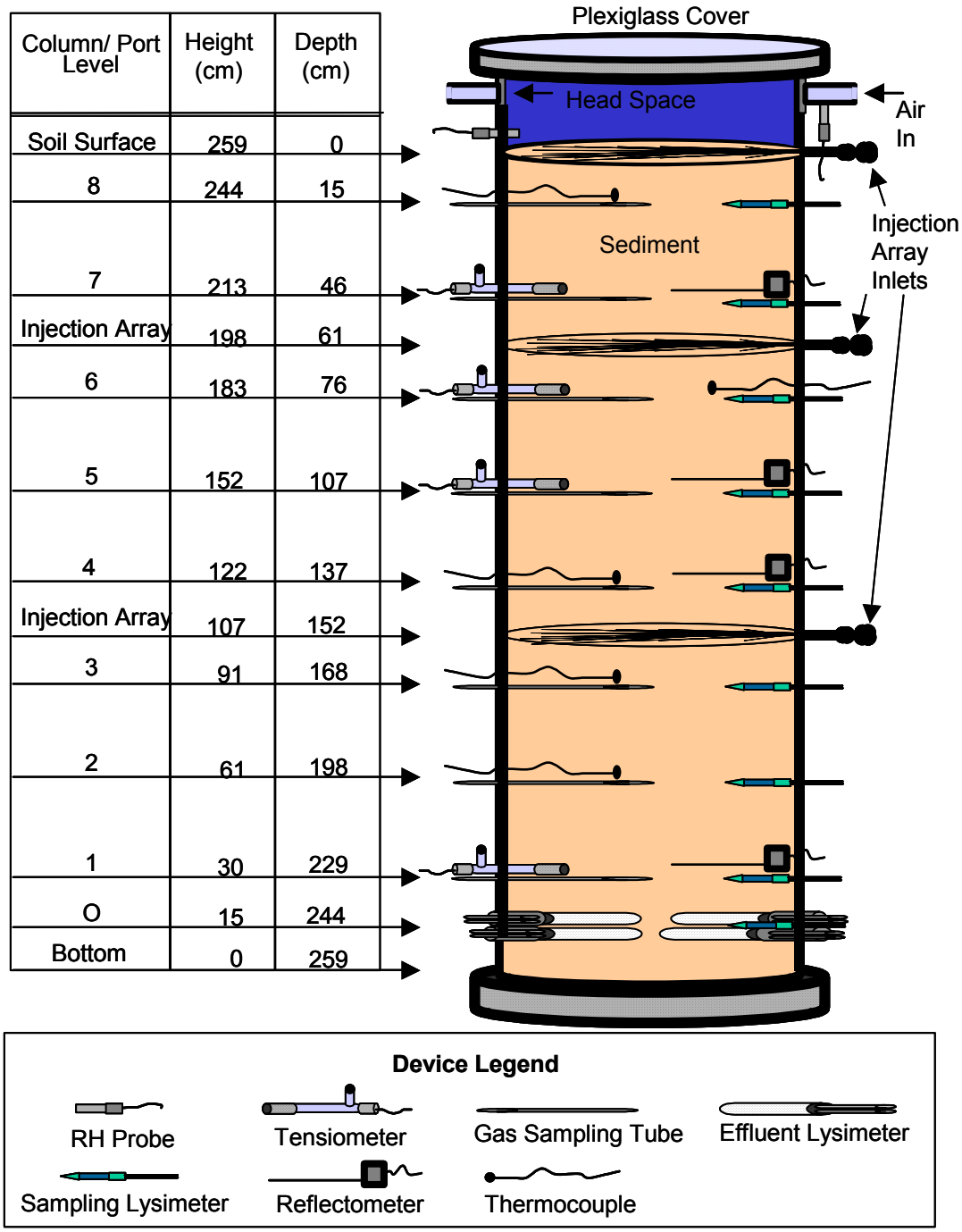

Figure 5. Elevation view of device placement. Note, the absolute bottom is 259.08-cm below the column surface. While level numbers indicate distance upward from the absolute bottom, Level "0" is actually at the mid-point between Level 1 and the absolute bottom.

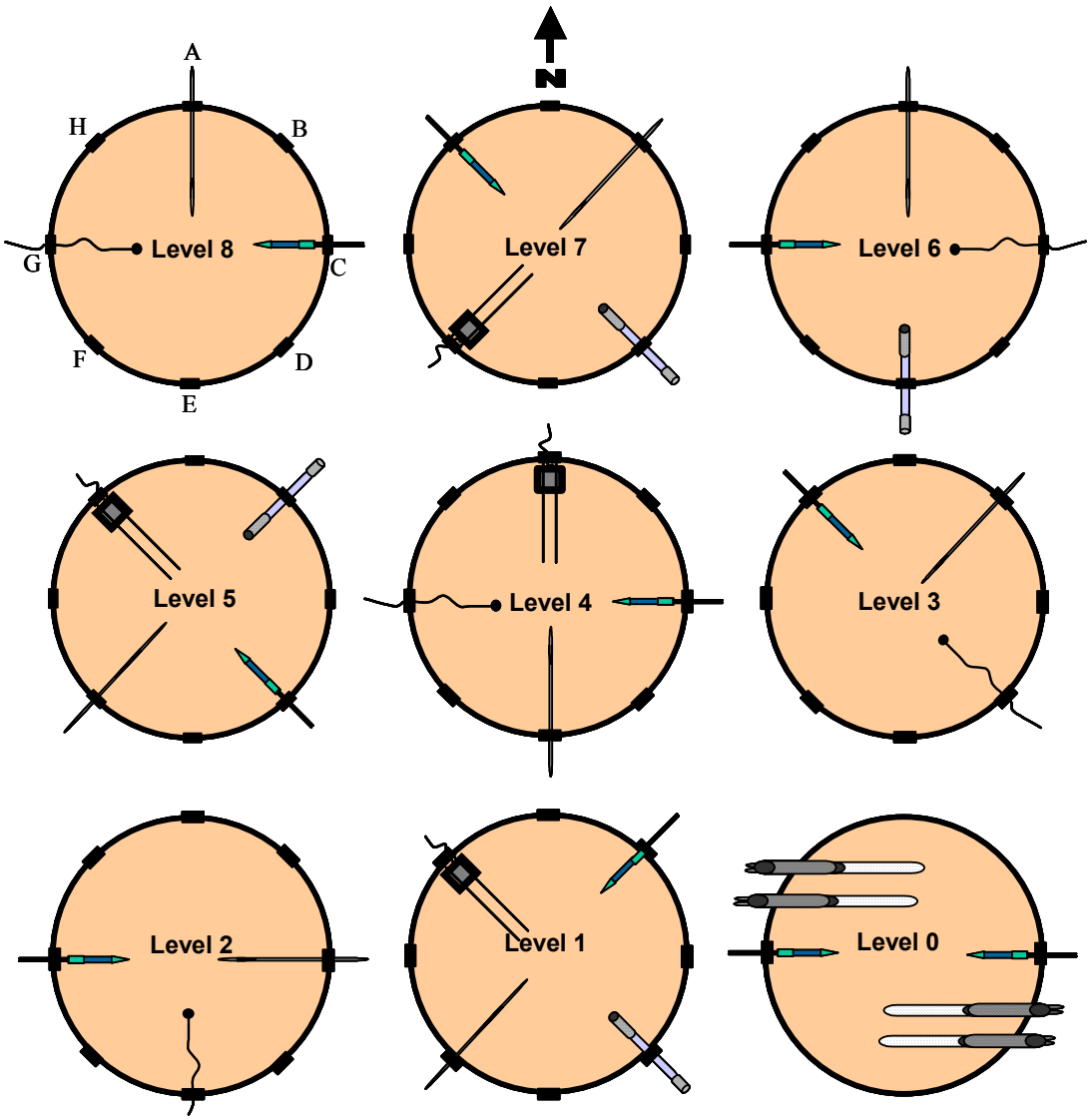

Figure 6. Placement of monitoring and sampling devices at each level (plan view). Letters A through H indicate geographic orientation. Effluent lysimeter positions are given in North-South and East-West coordinates. Note, although level numbers indicate distance upward from the absolute bottom, Level "0" is actually at the mid-point between Level 1 and the absolute bottom. See Figure 5 legend for device identification.

Table 2. Measurement of device locations.

Sensor/Sampler Type	Column Level (approximate distance from bottom in feet)	Depth Below Column Surface (cm)	Distance from Vertical Axis to Device Mid-Point (cm)
Tensiometers (Soilmoisture Equip. Corp., Model 2710A)	7, 6, 5, and 1	45.72, 76.20, 106.68, and 228.60	~30
Water Content Reflectometers (TDRs) (Campbell Scientific, Model 615)	7, 5, 4, and 1	45.72, 106.68, 137.16, and 228.60	~27
Thermocouples (common T-type)	8, 6, 4, 3, and 2	15.24, 76.20, 137.16, 167.64, and 198.12	~15
Soil Sampling Portholes	2, 3, and 8	198.12, 167.64, and 15.24	
Lysimeters, Pore Water Sampling (Soil Measurement Systems, Model SW-074)	8, 7, 6, 5, 4, 3, 2, 1, OC, and OG	15.24, 45.72, 76.20, 106.68, 137.16, 167.64, 198.12, 228.60, 243.84, and 243.84	~35
Effluent Lysimeters (Soilmoisture Equip. Corp., Model 1922)	O (6-in above the bottom)	4 at 243.84	2 at ~20 and 2 at ~30
Gas Samplers (common stainless steel tubing w/ perforations and nylon filter sleeves.)	8, 7, 6, 5, 4, 3, 2, and 1	15.24, 45.72, 76.20, 106.68, 137.16, 167.64, 198.12, and 228.60	~8

unsaturated hydraulic properties (i.e., van Genuchten parameters), and saturated hydraulic conductivity were performed for three additional samples. Two of these samples were taken from the drums and one, a 6.0-cm high by 5.7-cm diameter core sample, was taken from the top of the sediment column upon completion of packing. Results of gravimetric (weight %) and volumetric (vol%) water contents, bulk density, and porosity determinations are given in Table 3. Water potential-moisture content relationships (i.e., saturated drainage characteristics), unsaturated hydraulic property, and saturated hydraulic conductivity determinations are given in Tables 4, 5, and 6, respectively.

3.1.2.2 Mineralogy. The playa-derived sediments used in this study are representative of those used to cover the wastes buried at the SDA. In the Unified Soil Classification System, these sediments are classified as calcareous silty-clays. The bulk and clay size fraction mineralogy of SDA sediments have been analyzed by x-ray diffraction at the New Mexico Bureau of Mines and Mineralogical Resources;[c] the results are given in Tables 7 and 8. Mixed smectite-illite constitutes 50–70% of the clay minerals, and kaolinite, illite, and Ca-rich smectite comprise the remaining fraction.

c. Socorro, NM, USA.

Table 3. Measurement of initial (packing) water content, dry bulk density, wet bulk density, and porosity at time of column packing.

Sample ID	Initial (packing) Moisture Content		Dry Bulk Density ($g\ cm^{-3}$)	Wet Bulk Density ($g\ cm^{-3}$)	Calculated Porosity (%)
	Gravimetric (weight %)	Volumetric (vol%)			
INEEL Averages, n=265	—	14.2	1.31	1.46	51.0
Independent Lab					
Drum #1, n=1 (repack)	8.7	12.7	1.46	1.59	44.9
Drum #2 , n=1 (repack)	11.5	16.3	1.42	1.58	46.5
Core Sample, n=1 (not repacked)	10.9	15.6	1.43	1.59	46.0

Table 4. Sediment drainage characteristics, from saturation.

Sample ID	Water Potential (-cm water)	Moisture Content (vol%)
Drum #1, n=1 (repack)	0	42.8
	22	42.6
	52	42.2
	151	36.0
	510	26.9
	17031	15.5
	851293	5.9
Drum #2, n=1 (repack)	0	50.7
	22	50.5
	52	49.8
	151	44.1
	510	30.4
	17235	13.6
	851293	5.5
Core Sample, n=1 (not repacked)	0	50.2
	22	49.7
	52	48.5
	151	43.6
	510	31.4
	10096	18.7
	851293	5.6

Table 5. Unsaturated hydraulic properties (i.e., van Genuchten parameters).

Sample ID	Alpha (cm^{-1})	n (dimensionless)	θ_r	θ_s
Drum #1 (repack)	0.0122	1.2311	0.0165	0.4387
Drum #2 (repack)	0.0068	1.3953	0.0493	0.5155
Core Sample (not repacked)	0.0103	1.2342	0.0000	0.5109

Table 6. Saturated hydraulic conductivity.

Sample ID	K_{sat} (cm sec^{-1})
Drum #1 (repack)	0.000025
Drum #2 (repack)	0.000041
Core Sample (not repacked)	0.000040

Table 7. Bulk mineralogy of SDA sediments.

Mineral	Weight Percent
Quartz	50 to 75
Plagioclase and K-feldspar	10 to 25
Olivine and Pyroxene	<5
Calcite	<5
Iron	<5
Clay Minerals (primarily mixed smectite-illite, some kaolinite)	10 to 20

Table 8. General clay size fraction (<75 μm) SDA mineralogy.

Mineral	Weight Percent
Quartz	40 to 55
Plagioclase and K-feldspar	5 to 10
Calcite	5 to 10
Clay Minerals	30 to 45
Iron Oxides	5
Gypsum and Other Common Minerals	Trace amounts (<5)

3.2 Water Flow

3.2.1 Water Preparation and Composition

A surrogate vadose zone water was formulated to approximate the composition of rainwater with elevated dissolved solids due to concentration by infiltration. We prepared the water by adding accurately weighed (+0.001 mg) reagents to deionized water, see Table 9. Ion concentrations, both measured and calculated from component amounts, are given in Table 10.

Initially, hydrochloric acid (HCl) was used to adjust the influent water pH to 8.0 (± 0.2). On December 1, 2001 (~Week 20), this practice was discontinued and influent water pH was allowed to equilibrate by atmospheric exposure. This exposure occurred while the water was standing in the containers that supplied the pumps.

The influent water was sterilized by autoclave prior to storage and use. The volume of water was measured before and after autoclaving to ensure no volume gain or loss.

Though populations and densities of natural soil microorganisms were expected to out-compete microorganisms introduced by influent water, the introduction of a "foreign" biological component could impact physical and/or chemical properties of the soil. Therefore, a cursory characterization and count of influent water microorganisms was performed. Microbes associated with water storage and delivery systems were evaluated using a Zeiss Epifluorescent microscope with DAPI stain. Relative viability

Table 9. Surrogate vadose zone water components.

Compound	mg Added per L of Water
$NaHCO_3$	10.60
$MgCO_3$	3.17
$CaCl_2{:}2H_2O$	0.62
$CaSO_4{:}2H_2O$	10.03
$KHCO_3$	1.78

Table 10. Surrogate vadose zone water ion concentrations and chemistry.[a]

Ion	Calculated Concentration ($mg\ L^{-1}$)	Measured Concentration ($mg\ L^{-1}$)
Na^+	2.90	2.7
HCO_3^-	14.15	12.0
Mg^{+2}	0.90	0.9
Ca^{+2}	2.51	2.6
Cl^-	0.30	1.5[b]
SO_4^{-2}	5.60	5.4
K^+	0.7	0.7

a. Average measured: pH = 7.8; alkalinity = 36 ppm as $CaCO_3$; electrical-conductivity = 0.0315 mS cm^{-1}
b. Includes Cl from pH adjustment with HCl.

determinations were made using nutrient auger plates. A monoculture of rod-shaped microorganisms having single or double terminal lobes was observed in newly mixed water. The organisms, believed to be mold, were 2 to 3-µm wide. They formed multi-cellular chains ranging in length from 5 µm, in newly mixed water, to 35 µm, after average storage time. The concentration of this organism was ~1.8×10^5 organisms mL^{-1} of newly mixed water. During storage, additional filamentous and nonfilamentous organisms appeared in the water. The filamentous organisms were similar in size to the ones previously described and are believed to be mold or fungi. The nonfilamentous organisms are believed to be bacteria normally occurring in the environment. Auger plates of stored water produced statistically significant populations of microorganisms.

Water was delivered to the column surface using four banks of syringe pumps. Water entering each bank passed through a 1 GPH ultraviolet-light water purifier (mean purifier residence time ~40 min). Prior to isotope injection, nutrient auger plates were inoculated with water taken downstream from each purifier and incubated at room temperature for 10 days. Three of the four purifiers produced no viable cells. Water taken from a fourth purifier produced one round fleshy-beige colony having a uniform-regular border. In consideration of these results and the potential atmospheric deposition of microorganisms into the relatively open system, it was determined that no additional or unique microorganisms were added to the sediment by the surrogate vadose zone water. It should be noted that irregular green mats (10 ± 2-cm diameter) had colonized the column surface, around the water delivery points, at the time of isotope injection. At conclusion of this study, a community of photosynthesizing organisms had colonized ~80% of the surface. These organisms did not appear to affect hydraulic permeability.

3.2.2 Establishing and Maintaining Unsaturated Flow

Application (infiltration) of water began on July 11, 2001 at 12:00 p.m. This date is used throughout the study as the primary reference point for elapse time calculations. Water was delivered to the column by four syringe pumps (Figure 7). Each pump had six 10-cm^3 polyethylene syringes with one-way valves, and each syringe delivered water to one surface point via the surface injection array. Using individual syringes assured precise delivery and even distribution of water to the column's surface. The four pumps were programmed to periodically deliver ~29-mL of water to the column surface. Initially, the pumps were set to an eight-minute pause interval, which delivered ~5 L day^{-1}, to accelerate column wetting. As the wetting front approached the bottom of the column, the pause interval was increased to 41 minutes, delivering ~1 L day^{-1}; this setting was used for the duration of the study. The mass flow rate was monitored through periodic weighing of the four water supply containers.

To maintain steady-state hydraulic flow, four suction lysimeters[d] were located 15 cm above the bottom of the column. Each lysimeter consisted of a 25.4-cm long by 4.8-cm diameter ceramic cup with a -1.0-bar air entry pressure and a ~2-µm pore size. As the wetting front approached the column bottom, water was added to the lysimeters to establish a hydraulic connection between the lysimeter and the surrounding media, then vacuum was slowly increased until flow was established. A vacuum system applied a constant suction to the four lysimeters, continually drawing water from them and collecting the effluent in a container. (Using a common vacuum source potentially allows higher flow rates from lysimeters with higher hydraulic permeability. Nonuniform flow was expected to abate within a relatively short distance from the lysimeters.) The effluent water container was periodically emptied and the average mass flow rate was calculated. Initially, lysimeter suction was increased to maintain equivalent influent and effluent flow rates (i.e., ~1 L day^{-1}). However, on occasion, this suction led to air entry events that perturbed pore gas O_2 and CO_2 concentrations. Therefore, we did not apply the hydraulic potential

d. Soilmoisture Equipment Corp., Goleta, CA, Model 1922.

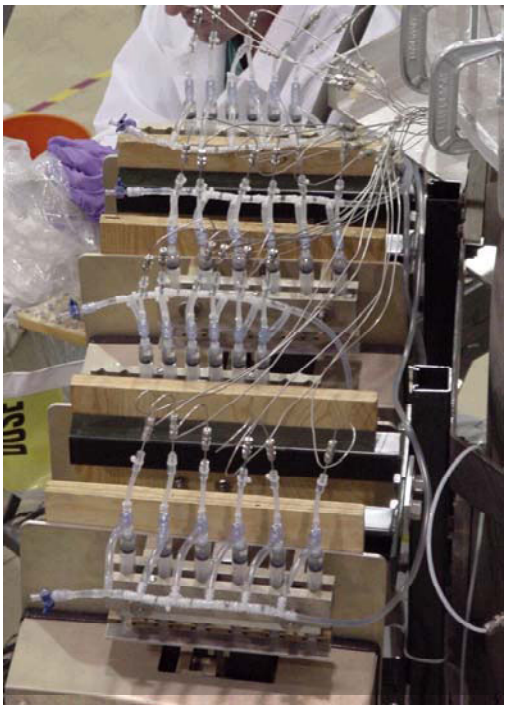

Figure 7. Syringe pump system for infiltration water delivery. Syringes and tubing are shown without pump motor housings.

necessary to maintain equivalent influent and effluent flows. Influent flow was not decreased to compensate for deficit effluent flow because decreased water content would have exacerbated the problem by increasing the lysimeter suction required to maintain equivalent influent and effluent flow. To avoid further pore gas perturbations, lysimeter suction was set at approximately -750-cm of total hydraulic head, which is just under the apparent air entry value (approximately –850-cm of total hydraulic head), for the duration of the study. This suction produced an average effluent flow rate of ~0.7 L day^{-1}, resulting in an inequality of influent and effluent flows. This inequality initially caused oxygen concentration to decline at the bottom of the column. To prevent anaerobic conditions, water was periodically removed from the bottom using the sampling lysimeters at Level 0. These extractions caused oscillations of matric tension. To avoid potential interference with tracer migration, the supplementary water extractions were discontinued and water content was allowed to equilibrate to the applied hydraulic potential.

3.3 Sampling and Analysis

3.3.1 Water

Sediment water samples were periodically collected using sampling lysimeters.[e] These lysimeters, constructed of stainless steel, have semi-porous walls through which water is drawn into the lysimeter under vacuum (-0.7 bar published bubbling pressure and an observed maximum pressure of -0.5 bar). Two stainless steel tubes, with shutoff values, extend from the lysimeters to the column's exterior (Figure 8). To extract samples, vacuum was applied, the shutoff values were closed, and sediment water entered until lysimeter vacuum was equilibrated with matric tension. Water samples were extracted under nitrogen gas. This was accomplished by venting one of the two lysimeter tubes to a Tedlar bag containing

e. Soil Measurement Systems, Tucson, AZ. Model SW-074.

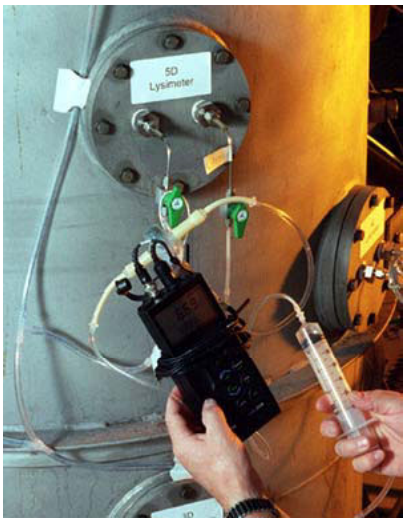

Figure 8. Pore water pH measurement using inline electrode. Stainless steel lysimeter tubing and shut off valves are shown extending from the column.

nitrogen gas and withdrawing the sample from the remaining tube using a syringe. The horizontal lysimeter orientation permitted the use of light suction for sample extraction. After sample extraction, shutoff valves were closed and the lysimeters were left containing nitrogen gas at neutral pressure.

3.3.1.1 Aqueous Species. Anion and metal analyses of water sample used ion chromatography (IC) and inductively coupled plasma (ICP) methods, respectively. The first three suites of water samples (collected in Weeks 26, 34, and 51) were analyzed at the INEEL Research Center (IRC) using a Dionex series 4500i IC and a Thermo Jarrell Ash IRIS Advantage series ICP. Water samples collected after isotope injection were analyzed at the INEEL Idaho Nuclear Technology and Engineering Center's (INTEC) laboratory. At INTEC, samples were analyzed using a Dionex IC[f] and a Jobin Yvon bench top ICP.[g] All samples to be analyzed for metals were preserved with nitric acid, at 0.1% (by volume). To prevent nitrite interference in the nitrate determination, the first three sets of anion samples were preserved with formaldehyde. This method allows samples to be stored for longer periods than with refrigeration alone. Nitrite was not present in the first three sample sets, so formaldehyde was not used with subsequent samples. Instead, anion samples were stored at 4°C prior to analysis.

Lysimeter samples were analyzed for dissolved carbon on two occasions. An aggregate Level 0 carbon sample was taken in Week 16 (41 weeks before the ^{14}C injection). This sample was analyzed at the IRC using a carbon analyzer.[h] The second sets of carbon samples were taken from lysimeters at each column level in Week 106 or (49 weeks after the ^{14}C injection). These samples were analyzed at INTEC using a carbon analyzer.[h]

3.3.1.2 Alkalinity, Electrical Conductivity, and pH. Total alkalinity was determined using colorimetric end point titration[i] of unfiltered samples; electrical conductivity was measured using a

---

f Model DX-500.

g Model JY 238.

h O.I. Analytical Model 700 College Station, TX.

i HACH digital titrator.

bench-top conductivity meter;[j] and soil water pH was determined using an inline electrode[k] with a portable pH meter.[l] Syringes were used to draw pore water samples from sampling lysimeters through the pH electrode, Figure 8. This configuration provided fast and stable pH measurements. While the pH electrode provided a fast response time, the stability of pH readings was attributed to isolation of water samples from the atmosphere (i.e., analysis under nitrogen gas). To prevent cross contamination, the electrode was rinsed with deionized water between measurements. Acidic solutions, including pH buffers, were removed from the column area to avoid unintentional release of radiolabeled CO_2 gas by acidification of water samples. Buffer solutions of 7.00 and 10.01 pH were used for instrument calibration. Though pH as low as 6.8 was occasionally measured, most measurements were 7.0 or greater. Therefore, the 7.00 to 10.01 calibration bracket was deemed acceptable.

3.3.2 Gas Concentration Measurements

The gas analysis system incorporated an infrared acoustic CO_2 analyzer[m] and a paramagnetic O_2 analyzer.[n] A 12-channel switching device[o] was used to select the source and route the gas sample to the analyzers. Gas was drawn from the source through the switching device and then into the analyzers by pumps onboard each analyzer. Background samples (i.e., laboratory air) were drawn from the headspace air intake tube. Headspace samples were drawn from the headspace outlet tube. Pore gas samples were drawn from perforated stainless steel tubes inserted in the column (~36-cm long by 0.6-cm diameter with 44 2-mm diameter perforations covered with woven nylon stocking material). Polyethylene tubing, with 0.16 cm wall thickness, was used to carry gas samples.

The analyzers and sample-channel selector were controlled by a LabVIEW-program that periodically recorded the CO_2 and O_2 concentrations of pore gas, headspace gas, and laboratory air samples. Each CO_2 measurement began with a sample chamber and tubing purge (3-s high speed, then 10-s low speed). The CO_2 analyzer was programmed to perform four measurements for each gas source; the recorded CO_2 concentrations are an average of the last three measurements. Discarding the first sample measurement provided stable (i.e., low variation) measurements. Each O_2 measurement began with a 15-s tubing and sample chamber purge. The O_2 analyzer performed dynamic measurements and reported the concentration every second. Thirty O_2 measurements were made from each gas source; the recorded O_2 concentrations are an average of these 30 measurements. Care was taken to avoid perturbing pore gas concentrations by excessive sampling. The amount of gas removed from the column during each column profile measurement was determined by measuring the sample exhaust rate of each analyzer. Flow rates were measured using a Gilibrator primary flow calibrator.[p] The CO_2 analyzer's 3-s tubing and 10-s sample chamber flow rates were 1713.6-cm^3 min^{-1} and 344.7- cm^3 min^{-1}, respectively. The O_2 analyzer produced a constant flow rate of 156.0- cm^3 min^{-1} for 45 s. Given these rates and durations, 4.37 L of pore gas was extracted from the column during each weekly soil profile measurement, compared to a pore gas volume of 356 L at 30% volumetric water content.

3.3.2.1 Gas Measurement Corrections. The CO_2 analyzer was calibrated by the manufacturer to be linear for SF_6 measurement in the range experienced in this study (1% error). No post measurement

---

j. Denver Instruments, Model 250.

k. Cole-Parmer No. 05992-64.

l. Orion Model 250.

m. INNOVA Model 1312.

n. INNOVA Model 1313.

o. INNOVA Model 1309.

p. INEEL Calibration Lab. #714817.

SF_6 calibrations were performed for reported data. However, duplicate samples were used to determine relative uncertainty of SF_6 measurements (Appendix A).

CO_2 measurements are nonlinear over the range of concentrations experienced in this study. While the analyzer was equipped with both low (0 to 1%vol) and high (1 to 25%vol) range CO_2 filters, the automated analysis system was not designed to select a CO_2 filter based on concentration. This prevents column perturbation by excessive gas sampling. We measured CO_2 concentrations using the analyzer's high-range filter and corrected the measurements with periodic measurements of certified CO_2 gas standards (Table 11). High-range filter measurements are expected to be linear within both low- and high-concentration ranges. Therefore, low- and high-range correction expressions were developed from linear fits (Figure 9) of the measurements of the certified CO_2 standards. These corrections are given in Equations (1) and (2), respectively. Headspace and room air measurements were corrected using Equation (1), while pore gas concentrations were corrected using Equation (2). CO_2 concentration measurements used to determine efficiency of the headspace CO_2 trap were not corrected because the low-range filter was used exclusively for these measurements.

$$CO_{2_{\text{LowRange}}} = 0.90 * \text{Measured } CO_2 + 45.68 \tag{1}$$

$$CO_{2_{\text{HighRange}}} = 0.98 * \text{Measured } CO_2 - 505.60 \tag{2}$$

where CO_2 is measured in ppmv.

The CO_2 analyzer does not automatically compensate for sample temperature and pressure at the time of each measurement. For this study, it calculated CO_2 concentrations based on fixed pressure and temperature values of 84.33 kPa and 25°C, respectively.

The O_2 analyzer was calibrated using ambient air, assumed to be 20.95 volume percent O_2, (vol%) and a pure nitrogen zero gas. The analyzer performs automatic sample temperature and pressure compensation. Measurements are expected to be linear over the range of 0 to 22 vol% (1% error). An ambient air measurement was included with each column O_2 profile measurement. Ambient air was consistently measured 0.9 to 1.2 vol% greater than 20.95 vol%. Prior to reporting O_2 concentrations, the differences between measured and assumed (i.e., 20.95 vol%) ambient air concentrations were subtracted from profile measurements, per Equation (3).

$$[O_2]_{\text{Reported}} = [O_2]_{\text{Measured}} - \left([O_2]_{\text{Measured ambient air}} - 20.95\right) \tag{3}$$

Table 11. Average measured values of gas standards used for low- and high-range CO_2 measurement corrections.

Date	CO_2 (ppmv)					
	Pure N_2 Gas	1,000 Std.	5,030 Std.	10,100 Std.	50,300 Std.	201,000 Std.
10/18/01	80	1,210	5,382	11,130	52,630	204,870
7/2/02	-54	913	5,390	10,811	52,287	206,810
8/29/02	-94		5,377		51,317	
11/21/02	-90	1,060	5,379	11,150	52,489	205,640
2/27/03	-95		5,384		51,233	
Averages	-51	1,061	5,382	11,030	51,991	205,773

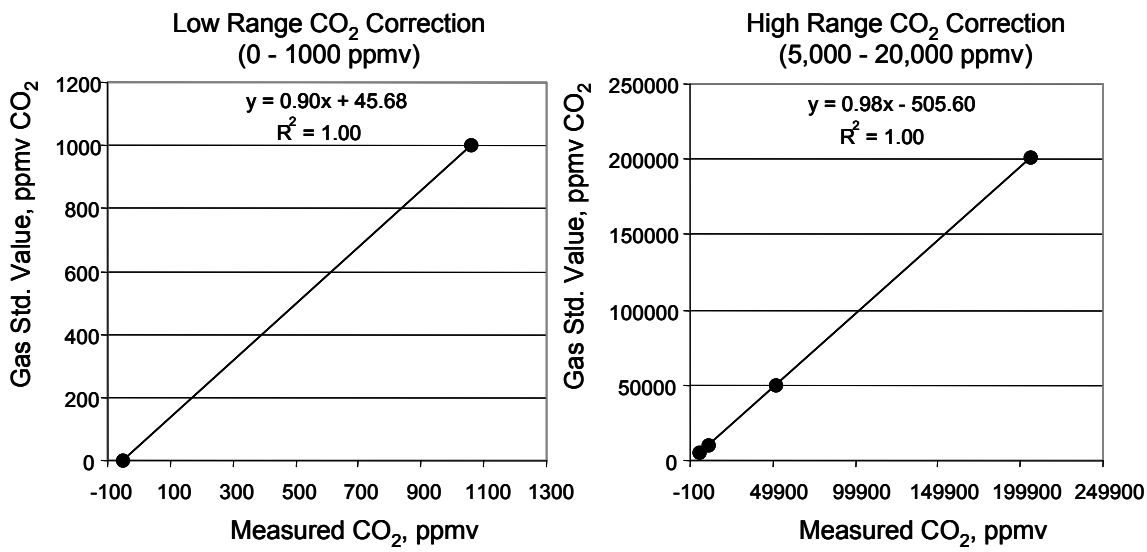

Figure 9. Linear fits used for low- and high-range CO_2 measurement corrections. Data points represent average gas standard measurements.

3.3.2.2 CO_2 Surface Flux. The surface flux of CO_2, by microbial metabolism, is calculated as the change in atmospheric CO_2 concentration as it passed through the headspace. We calculated CO_2 flux using the universal gas law with the change of CO_2 concentration, air temperature, column surface area, headspace ventilation rate, and barometric pressure. The headspace volume is directly proportional to the volume concentration of CO_2; therefore, headspace residence time may be ignored in flux calculations, assuming steady state conditions. The headspace ventilation rate was held constant by an MKS mass flow controller[q] that was calibrated at operating humidity and temperature by INEEL's Calibration and Standards Laboratory. The ventilation rate was set and recorded manually using the controller's digital display. Maintaining a constant ventilation rate for headspace gas at high relative humidity was complicated by water condensation in the flow controller. Condensation was largely prevented by using heat tape to elevate controller and tubing surface temperatures to ~35°C.

The barometric pressure used in flux calculations was recorded at the National Oceanic and Atmospheric Administration's station in Idaho Falls. Because a building's heating and ventilation system may affect laboratory air pressure, these barometric pressure measurements may not represent true ambient air pressure. Ambient air pressure measurements were not made in this study.

3.3.3 Water Content Determination

Four methods were employed to determine column water content: (1) gravimetric determinations, (2) mass balance of inflow and outflow waters, (3) sediment water (matric) potential, and (4) water content reflectometry. The sensors used in these methods were read every 5 s and hourly; running averages of theses readings were recorded using a Campbell Scientific data logger[r] with a PC208W software interface.

3.3.3.1 Gravimetric Water Content Determinations. Two benchmark water content determinations were made using core samples (ASTM D 2937). Water content and bulk density determinations were made in Week 35 for 6.0-cm high by 5.7-cm diameter horizontal cores taken from

q. Model 1559A-020L-SV.

r. Model CR10X.

Portholes 8B and 2F, with respective column depths of ~15 and ~198 cm. In Week 107, six vertical cores were taken to determine water content, bulk density, and solid phase ^{14}C activity (Figure 10). These cores were taken at six injection points along the North-South column transect, identified by numbers 1, 5, 9, 13, 17, and 21 in Figure 4. These cores represent the sediment profile extending from the column surface through the isotope injection plane to Level 6, a depth of ~76-cm. Two core samples, an upper sample (surface to Level 7) and a lower sample (Level 7 to Level 6) were taken from each of the six locations using two separate, 4.5-cm diameter, coring tubes. Additional bulk samples were taken from Portholes 3F and 2F, at respective depths of ~168 and ~198 cm, one day after the vertical cores. These samples were extracted from porthole areas adjacent to but not disturbed by previous sediment sampling. Vertical cores and bulk samples were used to determine water content at Levels 8, 7, 6, 3, and 2. Bulk densities were determined for upper and lower core samples. Standard laboratory methods were followed for water content (ASTM D 2216-98) and bulk density (ASTM D 2937) determinations.

Figure 10. Column coring for gravimetric water content and solid phase ^{14}C activity determinations.

3.3.3.2 Mass Balance Water Content Determination. Water content by mass balance was calculated as the difference in total inflow and total outflow plus a packing water content of 10%. (The packing water content was established through evaluation of reflectometry water content measurements). Total inflow included the surrogate vadose zone water and tracer solutions. Total outflow included

column effluent, sample extractions, and headspace evaporative loss. While injected and extracted waters were easily tracked by direct measurements, determination of headspace evaporative loss required monitoring the relative humidity, temperature, and headspace ventilation rate. The relative humidity of laboratory air and headspace gas was monitored using MET-One relative humidity sensors.[s] The headspace temperature was assumed equal to the laboratory air temperature. The headspace ventilation rate was monitored via the mass flow controller's digital display.

We determined evaporative water loss by modifying the ideal gas law to calculate the number of water molecules (moles) removed from the headspace. Because this calculation involves vapor-phase water, a functional relationship describing water-vapor pressure as a function of temperature was developed from published vapor-pressure values over a 0 to 35°C temperature range (Olmsted and Williams 1994). This functional relationship was combined with the difference in supply air and headspace humidity to modify the ideal gas law for moles of water removed as a function of temperature and humidity (Equation (4)). The mass removal rate is obtained using the headspace ventilation rate and the molecular weight of water (Equation (5)). Under steady state conditions, the change in headspace volume is proportional to the change in water vapor concentration; therefore, residence time may be ignored and the unit volume drops out of the expression.

$$n_{\text{Removed}}\left(t, RH\right) = \left[\frac{V\left(VP_{\text{H}_2\text{O}}\left(t\right)\left(\frac{\Delta RH}{100\%}\right)\right)}{RT}\right] \tag{4}$$

$$\text{H}_2\text{O}_{\text{Removed}}\left(t, RH\right) = Q\left(n_{\text{Removed}} * MW_{\text{H}_2\text{O}}\right) \tag{5}$$

where

$n_{\text{Removed}}\left(t, RH\right)$	=	moles of water removed from headspace as a function of temperature and relative humidity, °C and %
V	=	unit volume of gas, L
$VP_{\text{H}_2\text{O}}\left(t\right)$	=	water-vapor pressure as a function of temperature = $0.0063e^{0.0634*t}$, atm
t	=	gas temperature, °C
ΔRH	=	difference of supply air and headspace relative humidity, %
R	=	the gas constant = 0.08206 L atm mol^{-1} K^{-1}
T	=	gas temperature = °C + 272.15, K
$\text{H}_2\text{O}_{\text{Removed}}\left(t, RH\right)$	=	water removal rate, g day^{-1}

s. Model 083D.

Q	=	volume flow rate of headspace gas, L day^{-1}
MW_{H_2O}	=	molecular weight of water = 18.0 g $mole^{-1}$.

3.3.3.3 Matric Potential Determinations. Matric potential was recorded using ceramic cup tensiometers[t] with Honeywell pressure transducers.[u] The ceramic cups were 5.1-cm long by 2.5-cm diameter with a published -1-bar air entry pressure. The pressure transducers were calibrated at INEEL's Calibration and Standards Laboratory. The calibration expressions used to convert transducer output (millivolt) to water potential (millibar of negative pressure) are given in Table 12.

Prior to taking measurements, water was added to the tensiometers until a hydraulic connection was established between the ceramic cup and surrounding media. Having established the hydraulic connection, the matric potential became increasingly negative as the added water equilibrated with the sediment. Excessive air bubbles resulted in the occasional loss of matric potential readings until the air bubbles were flushed from the tensiometer.

The matric head was calculated by converting matric potential (i.e., -millibar of pressure) to total hydraulic head (i.e., -cm of H_2O), then subtracting the elevation head from each tensiometer level (assuming pore gas and solute heads are negligible). Water content was inferred from matric head using the drainage moisture characteristic curve (MCC) and van Genuchten curve fitting parameters given in Tables 4 and 5, respectively.

Table 12. Tensiometer pressure transducer calibration expressions.

Tensiometer (depth below surface)	Conversion Expressions (mV = transducer millivolt output)
Level 1 (229 cm)	Millibar = 4.8565 mV+22.96
Level 5 (107 cm)	Millibar = 4.8527 mV-4.956
Level 6 (76 cm)	Millibar = 4.8954 mV-15.71
Level 7 (46 cm)	Millibar = 4.8565 mV-20.12

3.3.3.4 Water Content Reflectometers. Volumetric water content was determined using water content reflectometers.[v] This method is a form of time domain reflectometry (TDR); therefore, we refer to the reflectometers as TDR probes. TDR probes measure the period of an electromagnetic wave as it propagates along the probe's wave guides. Parameters influencing wave propagation are water content, solid/aqueous phase electrical conductivity, media texture/lithology, and temperature. Water content, electrical conductivity, and media texture parameters are incorporated into conversion of probe measurements to water content by calibrating the probes to known water contents in the current sediments. Calibration provides an expression describing water content as a function of wave period. Once converted to water content, probe measurements are corrected for thermal interference.

Prior to installation, the four TDR probes used in this study were calibrated as follows.

1. Water was mixed with SDA sediment in a plastic tub.

---

t. Soilmoisture Equip. Corp., Model 2710A.

u. Model #26PCCFA6D.

v. Campbell Scientific Inc. Model CS615.

2. The four TDR probes were embedded in the tub of moistened sediment.

3. Sediment samples were taken for volumetric water content determination.

4. Probe measurements (wave periods) were recorded.

This process was repeated for three sediment water contents (dry, moistened, and water saturated). The recorded wave periods and corresponding water contents were given to Campbell Scientific Inc.[w] for derivation of the expression for water content as a function of wave period, τ, that is given in Equation (6). This equation is derived in part from the expression for bulk electrical conductivity, σ_{bulk}, given in Equation (7). Equation (7) incorporates volumetric water content, ϑ_{υ}, and a sediment-specific transmission term, T, with the electrical conductivity of both solid, σ_{solid}, and aqueous, $\sigma_{aqueous}$, phases. The sediment-specific transmission term and solid-phase electrical conductivity were not determined in this study. Therefore, bulk electrical conductivity was assumed equivalent to that determined for a sediment-water leachate (i.e., $\sigma_{bulk} = \sigma_{aqueous}\vartheta_{\upsilon}$).

$$\vartheta_{\upsilon}(\tau) = -0.205 + 0.232 * \tau + 0.069 * \tau^2 \tag{6}$$

$$\sigma_{bulk} = \sigma_{aqueous}\vartheta_{\upsilon}T + \sigma_{solid} \tag{7}$$

Sediment temperatures were used for thermal interference corrections. Thermal corrections published by Campbell Scientific are given in Equations (8) and (9). A thermal interference that affects probe measurements more than approximately ±1.6% cannot be corrected using these equations. Beyond this threshold, the probes are more responsive to changes in temperature than to changes in water content.

$$\mathrm{Coef}_{\mathrm{Temperature}} = -3.46 * 10^{-4} + 0.019 * \vartheta_{\upsilon}(\tau) - 0.045 * \vartheta_{\upsilon}(\tau)^2 \tag{8}$$

$$\vartheta_{\upsilon-\mathrm{Corrected}} = \vartheta_{\upsilon}(\tau) - \left[(t-20) * \mathrm{Coef}_{\mathrm{Temperature}}\right] \tag{9}$$

where

$\mathrm{Coef}_{\mathrm{Temperature}}$	=	temperature correction coefficient
ϑ_{υ}	=	volumetric water content, from Equation (6)
τ	=	TDR probe measurement (i.e., wave period)
$\vartheta_{\upsilon-\mathrm{Corrected}}$	=	volumetric water content corrected for thermal interference
t	=	temperature of sediment in contact with probe wave guides.

w. Jim Bilskie, soil physicist, Campbell Scientific Inc., 435-750-9580.

3.4 Tracer Preparation, Injection, and Analysis

Both nonreactive and reactive tracers were used to examine physical and chemical properties of contaminant transport. The nonreactive tracers were sulfur hexafluoride (gaseous SF_6), bromide (lithium bromide solution), and tritium (^3H as water); reactive tracers were solutions of radiolabeled sodium carbonate (^{14}C) and uranium (depleted U). Methods of tracer preparation, injection, and analysis are described in this section.

3.4.1 Sulfur Hexafluoride

Sulfur hexafluoride (SF_6) tracer tests were performed at the initial (packing) water content (~10 vol%) and again at the experimental water content (~30 vol%, the water content for the isotope study). Replicates were performed for each of these two tests, for a total of four tests. The packing water content test was performed 17 weeks prior to start of water application (infiltration) with a replicate 3 weeks later. Between these tests, residual SF_6 was evacuated from the column by applying vacuum to the gas ports and drawing atmospheric air from the column surface through the sediment. The experimental water content test was performed in Week 41, with the replicate test 6 weeks later. Residual SF_6 was not flushed from the sediment between these tests, but was allowed to naturally attenuate.

For each tracer test, ~10-cm^3 of a certified SF_6 gas standard (99.995%vol) was injected through the injection array located 152 cm below the column surface. This injection depth was selected to maximize the distance over which diffusion was monitored. Five 10-cm^3 disposable syringes, each containing ~2-cm^3 SF_6, were connected to the Number 4, 6, 7, 16, and 18 injection tubes and simultaneously discharged. The SF_6 remaining in the injection tubes was not flushed; therefore, slow diffusion of that SF_6 into the column would be expected. We estimated that ~1.8-cm^3 of SF_6 remained in the tubing after each tracer injection (based on an estimated total tube length of 365.76-cm and a 0.0794-cm inside diameter.)

Sediment gas SF_6 profiles were monitored using the INNOVA 1312 analyzer. During the experimental water content tests, approximately 4.37-L of gas was removed from the column during each gas profile measurement. Although the gas volume extracted was not determined for the two tests conducted at packing water content, it is probably similar to that for the other tests. For the packing water content tests, 10 gas profile measurements were made in the first ~15 h of both the primary and replicate tests. Thus, for a measurement volume of 4.37-L per gas profile, 43.7-L would be removed during the first ~15 h of these tests. For the first experimental water content test, 17 gas profile measurements were made in the first ~15 h. This represents 74.3-L of gas removed during the initial ~15 h. The effect of sample gas extraction on SF_6 diffusion was evaluated by decreasing the sampling interval, and thus the total amount of gas removed, during the replicate experimental water content test. For this test, 7 gas profile measurements were made in the first ~15 h. This represents 30.6-L of gas removed during the initial ~15 h of the test. A total pore gas volume of 356 L is calculated for a 30 vol% water content.

3.4.2 Lithium Bromide

An aqueous lithium bromide (LiBr) tracer was injected into the column on two occasions, at 36 then 94 weeks. The first LiBr injection was made as steady-state chemical and hydraulic conditions were approached. In comparing transport rates of this Br^- test and that of a subsequent tritium tracer test, ^3H transport appeared to be significantly retarded. This could be the result of either anion (i.e., Br^-) exclusion or tritium sorption. To test which mechanism was the cause, a tritium tracer was included with the second LiBr injection.

The first LiBr injection used 240-mL of 9.89 mg Br^- mL^{-1} in surrogate vadose zone water; the second used 238-mL of 10.75 mg Br^- mL^{-1} in equal parts of pore water extracted from Levels 6 and 7.

These concentrations were calculated to ensure detection after migration to the column bottom. The Br^- solutions were injected at 60.96 cm below the column surface. This depth was selected to maximize monitoring distance for downward detection of solutes. To minimize perturbation of local hydraulic potential, the first Br^- spike was added under gravitational and capillary force. This was accomplished by placing ~10-mL aliquots of solution in a bank of 24 syringes (open-ended, 10 cm^3) mounted 58 cm above the injection plane and allowing the solution to drain into the column under atmospheric pressure. Parafilm was used to minimize evaporative losses. This gravity/capillary force injection took 3.7 h. The second Br^- spike was injected by force using 24 individual syringes, each containing ~10-mL of injectate. This injection took 1 h.

For the first test, Br^- samples were promptly analyzed, without refrigeration, at the IRC. The second test occurred after ^{14}C injection. Those water samples were collected and stored at 4°C prior to being shipped to INTEC for analysis.

3.4.3 Uranium, Carbon-14, and Tritium Injection

An aqueous cocktail of uranium, ^{14}C, and tritium was prepared. Uranium was in the form of an inductively coupled plasma (ICP) analyzer depleted U standard, ^{14}C as radiolabeled sodium carbonate, and tritium (^3H) as water. The ^{14}C and ^3H activities were selected to comply with facility isotope limits while providing activities above analytic detection limits. The mass of uranium was selected, through rigorous geochemical solubility calculations, to prevent uranium precipitation upon injection while providing concentrations above detection limits.

Maintaining uranium solubility in the tracer cocktail required a ~3-L injection volume. However, injecting this volume would create severe chemical and hydraulic perturbations. To minimize these perturbations, water was extracted from the column, mixed with the tracers, and injected back into the column. Although this process was performed as rapidly as possible, it took 11 days. Injectate water extraction began at ~55 weeks. This water was extracted from sampling lysimeters located 15.2-cm above and below the injection plane (i.e., Levels 6 and 7). The extracted water was combined daily and stored at -10°C in a 5-L polypropylene container with an airtight lid. The total mass of water extracted and stored was 3,070.95-g.

To prepare for tracer injection, ~2.0 mL of 1-microCi $^{14}C\ g^{-1}$ and ~0.9 mL of 1-microCi $^3H\ g^{-1}$ were combined with 50 mL of pore water in a 100-mL volumetric flask with a glass stopper. This solution was stored at 4°C until sufficient water was extracted. On the day of injection, the ^{14}C and ^3H solution was added to the extracted pore water. Then, a 5.3333-g (± 0.0001) aliquot of a 1-g U L^{-1} ICP standard was added to the mixture. The cocktail was allowed to equilibrate to room temperature, then mixed. Its pH was measured (~8.0) and a 220.88-g sample was taken for ^{14}C, ^3H, and U analysis.

The isotope cocktail was injected via the array located 60.96-cm below the column surface in Week 57. One 125-mL Pyrex syringe was used to inject cocktail into each of the 24 injection tubes, Figure 11. The amount injected through each tube was determined by weighing the syringe before and after each injection; 2,849.97 g was injected into the column or ~119 g per injection point. To push the cocktail from the injection tube into the column, each injection was followed by an injection ~3 cm^3 of air. Nevertheless, some cocktail is expected to have remained in the stainless steel injection array and polyvinyl chloride manifold tubing.

As described in the section on lithium bromide, a combined ^3H and Br^- injection was made because the first ^3H and Br^- tracer tests, initiated ~20 weeks apart, indicated significant retardation of ^3H movement relative to Br^- movement. A simultaneous injection was made in Week 94 to evaluate anion exclusion (i.e., accelerated Br^- movement) as the cause of apparent ^3H retardation. For this injection,

Figure 11. Injection of the ^{14}C, tritium, and uranium cocktail solution. The injection syringe, polyvinyl chloride tubing, and Luer fittings are shown. To contain water vapor and prevent the spread of radiological contamination, the syringe was enclosed in a plastic bag.

approximately 0.9 mL of a 1.0-microCi ^{3}H g^{-1} solution and 2.78-g of LiBr were added to ~251 g of pore water extracted from Levels 6 and 7. A ~16-g aliquot was taken for ^{3}H and Br^{-} analysis and 238.44-g was injected using the array 60.96-cm below the surface (~9.9-g per injection point). To push the cocktail from the injection tube into the column, each injection was followed by an injection ~3 cm^{3} of air.

3.4.3.1 Uranium Analysis. Lysimeter water samples were used to monitor uranium (U) movement. U analyses were performed using a Chemcheck[x] automated laser-induced kinetic phosphorescence analyzer (KPA) with Uraplex[y] scintillating cocktail. This method reports uranium as total U with a minimum detection limit of 0.5 μg L^{-1}. The KPA was calibrated using solutions prepared by serial dilution of an inductively coupled plasma (ICP) analyzer depleted U standard. KPA results were verified by analysis of sample splits using a Thermo Electron[z] inductively coupled plasma mass spectrometer at INEEL's Test Reactor Area ICP-MS laboratory.

Approximately one year after U injection (i.e., ~50 weeks), water samples collected from Level 6, 15-cm below the injection plane, did not show uranium migration. At this time (~107 weeks after start of infiltration), the column was cored, as described in Section 3.3.3.1, Gravimetric Water Content

x. Model KPA-L.

y. Chemcheck Industries.

z. Series X ICP-MS.

Determinations. Vertical cores were taken that represent the sediment profile from the column surface through six of the cocktail delivery points to Level 6. At the time of this report, the extent of U movement is being evaluated by acid slurry extraction of U from core subsamples. The extent of U movement and the uranium sorption coefficient will be the focus of a later report.

3.4.3.2 Carbon-14 and Tritium Analysis. ^{14}C and ^{3}H activities were measured using a Beckman[aa] liquid scintillation counter (LSC) at the IRC, following procedures given in Appendix B. Two separate scintillation cocktails were used to accommodate alkaline and acid sample matrices—Ultima-flo AF[bb] with alkaline samples and Ecolum[cc] with acidified samples.

Pore water samples were collected from lysimeters for ^{3}H and ^{14}C activity analysis. In mixed isotope samples, ^{14}C interferes in ^{3}H counting. We minimized this interference by lowering the sample pH to ~2. At low pH, ^{14}C may defuse from solution as radiolabeled CO_2 gas ($^{14}CO_2$). However, CO_2 gas is highly soluble in water; therefore, ^{14}C activity was not completely eliminated. Nevertheless, this method worked well for ^{3}H counting at observed activities. Relatively low ^{3}H energy allowed ^{14}C counting without effort to reduce ^{3}H background. We made alkaline dilutions of ^{14}C water samples to prevent gas phase partitioning and loss of $^{14}CO_2$.

Pore gas samples were collected for $^{14}CO_2$ activity analysis using a 1-L gas syringe. The automated gas sampling system was disconnected and gas samples (each 200 mL) were taken from the stainless steel sampling tubes. Immediately following extraction, each gas sample was injected into a 1-L Tedlar bag containing a known mass of CO_2 trap solution [0.5M sodium hydroxide (NaOH)] and shaken vigorously to trap the $^{14}CO_2$ gas. Aliquots of the CO_2 trap solutions were weighed for ^{14}C analysis.

^{14}C flux at the column surface was monitored by LSC analysis of headspace $^{14}CO_2$ samples. A split of the total headspace flow was bubbled through a 2 molar NaOH trap solution (~1300 mL) to collect CO_2 samples. Though the headspace ventilation system provided a constant total gas flow, accurate measurement of both the total and trap flow rates is critical to ^{14}C surface flux calculations. During CO_2 sample collection periods, headspace exhaust and CO_2 trap flow rates were occasionally measured using a Gilibrator primary flow calibrator.[dd] CO_2 trap efficiency was calculated using INNOVA 1312 analyses of headspace gas entering and exiting the CO_2 trap. A sample collection period of approximately seven days found an average trap efficiency of 96% (±1.4%). At the end of each collection period, the trap volume was recorded, sample aliquots were taken, and the trap solution was replaced with new solution. ^{14}C surface flux is calculated from the average activity of three separate aliquot determinations. Aliquot mass and isotope disintegration counts were combined to calculate aliquot activity (Equation (10)). Equation (10) is combined with CO_2 trap efficiency, gas flow rates, and total trap mass to calculate ^{14}C activity flux (Equation (11)). Total ^{14}C activity released by surface flux is determined by plotting Equation (11) over time and integrating the area under the curve.

$$\mathrm{Act}_{\mathrm{Sample}} = \frac{\mathrm{C} * \mathrm{DPM}}{\mathrm{m}_{\mathrm{Sample}}} \tag{10}$$

aa. Model LS 6000LL.

bb. PerkinElmer Analytical

cc. ICN Biomedical.

dd. INEEL Calibration Lab. #714817.

$$F_{14C} = \frac{Act_{Sample} * Q_{Total} * m_{Trap}}{\Delta t * Q_{Trap} * \left(\frac{EFF}{100\%}\right)} \quad (11)$$

where

Act_{Sample}	=	activity per gram of aliquot, microCi g^{-1}
C	=	conversion factor, 4.5E-7 microCi disintegration^{-1} min^{-1}
DPM	=	disintegration's per minute (liquid scintillation counts)
m_{Sample}	=	mass of aliquot, g
F_{14C}	=	^{14}C flux, microCi day^{-1}
m_{Trap}	=	total mass of CO_2 trap solution, g
Q_{Total}	=	total headspace flow (ventilation), liters min^{-1}
Q_{Trap}	=	CO_2 trap flow (split of total headspace flow), liters min^{-1}
Δt	=	period of CO_2 trapping, days.
EFF	=	CO_2 trap efficiency, %.

Solid phase ^{14}C activity at Levels 8, 7, 6, 3, 2, and the column surface were determined from vertical core and bulk sediment samples described in Section 3.3.3.1, Gravimetric Water Content Determinations. Surface activity was measured for ~0.3-cm thick samples of the vertical cores taken at the sediment/atmosphere interface. At the time of vertical coring, the column surface had a significant community of photosynthesizing organisms. We expect solid phase ^{14}C activity to be associated primarily with inorganic species; therefore, biological uptake is not included in our determination of solid phase ^{14}C. Solid phase ^{14}C was extracted by acidification of sediment aliquots and capture of liberated $^{14}CO_2$ gas using a sodium hydroxide trap solution. Trap solution activity was measured by LSC. These measurements represent an aggregate solid, liquid, and gas phase ^{14}C activity. Liquid and gas phase ^{14}C activity profiles, determined five days prior to coring, were used with aliquot water contents, determined from sample splits, and aliquot mass (~5-g) to subtract liquid and gas phase activity from trap solution measurements. The resulting solid phase activities were divided by dry aliquot mass, calculated from sample split water contents, to produce an average vertical solid phase activity distribution (i.e., ^{14}C activity per gram of dry sediment) from the six core and two bulk samples.

^{14}C activity, partitioned in solid, aqueous, and gas phases, was used to calculate the aqueous/gas (K_{ag}) and aqueous/solid (K_d) ^{14}C partition ratios at the time of vertical coring (approximately one year following the isotope injection). The total residual solid phase activity was calculated by plotting the average activity distribution over dry sediment mass then integrating the area under the curve. The average lift density given in Table 1 (1.31g cm^{-3}) was used with measurements of vertical core and bulk sediment water contents (Section 3.3.3.1, Gravimetric Water Content Determinations) to calculate dry sediment mass. Total aqueous and gas phase activities, on the day of coring, were calculated by plotting

their activity profiles over respective water content and gas-filled pore volume profiles, then integrating the area under the curves. Residual (retained) ^{14}C activity partitioned in solid, aqueous, and gas phases was combined with the activity removed by sampling, effluent water, and surface flux to calculate a ^{14}C activity mass balance (percent of injected activity).

4. RESULTS AND DISCUSSION

This chapter is divided into three sections, hydro-chemical characterization, biological assays, and tracer and ^{14}C transport. In Section 4.1, measurements of water content, bulk density, chemistry, and sediment-gas concentrations are presented to establish hydraulic and chemical state in relation to the ^{14}C transport study. Preliminary bioassay results are discussed in Section 4.2. Results of the tracer, ^{14}C, and uranium transport tests are presented in Section 4.3. Errors associated with these measurements are discussed in Appendix A.

4.1 Hydro-Chemical Characterization

In this study, hydraulic steady state is defined as an extended period during which hydraulic flux and volumetric water content do not change with time. The hydraulic state was monitored using four independent methods: gravimetric, mass balance, matric potential, and TDR probes. These methods indicate that relatively constant hydraulic flux (~1.0 L day^{-1}) and volumetric water content (~28%) were maintained during the transport study. Below, water content measurements and the interpretation of data sets are discussed for each method. We present a summary of water content determinations, relative to ^{14}C and the first Br^- injections in Table 13.

Table 13. Summary of water content determination by four independent methods.

Method of Water Content Determination	Column Level	Water Content at Time of Br^- Injection #1 (vol%)	Water Content at Time of SF_6 Test #2 (vol%)	Water Content at Time of ^{14}C, ^3H, and U Injection (vol%)	Water Content 26 Weeks After ^{14}C, ^3H, and U Injection (vol%)	Water Content 50 Weeks After ^{14}C, ^3H, and U Injection (vol%)
Weeks after start of infiltration (approximate)		35	41	57	83	107
Core and porthole gravimetric determinations (average values)	8	24.0				25.3
	7					26.1
	6					25.7
	3					24.2
	2	27.2				24.6
	Average	25.6				25.2
Mass balance	Average	29.8	29.9	29.7	30.1	29.3
Tensiometer/ matric potential estimation	7	~29	~29	~29	~29	~29
	6	~29	~29	~29	~29	~29
	5	~29	~29	~29	~29	~29
	1	~29	~29	~29	~29	~29
	Average	~29	~29	~29	~29	~29
TDR probes	7	27.7	27.3	26.2	27.6	27.7
	5	27.9	27.7	26.1	27.6	28.1
	4	29.2	28.1	25.8	30.6	28.4
	1(excluded)					
	Average	28.3	27.7	26.0	28.6	28.1

4.1.1 Water Content and Bulk Density

The general consistency of the four independent approaches (i.e., gravimetric, mass balance, tensiometer, and TDR probe) and the reliability of the mass-balance method, suggest a volumetric water content of 30% (± 1%) during the transport experiments. This water content value will be compared to those estimated by fitting analytical solutions to Br^- and SF_6 tracer breakthrough curves in Section 4.3.

4.1.1.1 Gravimetric Water Content Determination. Results of three gravimetric water content determinations are given in Table 14. The first determinations were made, for Level 8 and 2 portholes, in Week 35 (23 weeks before ^{14}C injection) when influent and effluent water flow rates indicated approach of hydraulic steady state. We extracted the second set of Level 8 and 2 porthole samples in Week 89, 32 weeks after the ^{14}C injection when radiological hazards associated with handling sediment samples diminished. A third set of water content determinations were made from the six vertical cores extracted 107 weeks after the start for inflow or 50 weeks after the cocktail injection. The six cores, consisting of two sections each, were extracted at six sampling locations and extended from the column surface to a depth of ~76 cm. Due to air voids resulting from excessive compaction, water contents were not determined for some core subsamples (e.g., Levels 8 through 6 at Point 9). These voids are believed to be sufficient to reduce sediment water content through vapor phase loss. Water contents were determined for the remaining vertical cores. Measurements are reported as volumetric water contents by converting gravimetric measurements to volumetric equivalences, assuming a pore water density of 0.998 g cm^{-3} at 20°C.

Between the first and second determinations, the water content increased by 3.9% (from 24.0 to 27.9 vol%) at Level 8 and by 4.1% (from 27.2 to 31.3 vol%) at Level 2 (Table 14). These apparent increases represent a relatively small change occurring over a relatively long period, 55 weeks. The third determinations show the water contents to be virtually identical at Levels 3 and 2 (24.2 and 24.6 vol%, respectively). This consistency of Level 3 and 2 water contents suggests lower column vertical

Table 14. Water content determinations of porthole and core samples, vol%.

Elapse Time and Sample Type	Level 8	Level 7	Level 6	Level 3	Level 2
Week 35					
Porthole Samples	24.0				27.2
Week 89					
Porthole Samples	27.9				31.3
Week 107					
Point 1 Core	23.9	25.8	25.6		
Point 5 Core	26.3	26.6	25.7		
Point 9 Core					
Point 13 Core	25.2	24.2	24.0		
Point 17 Core	25.6	26.6	28.2		
Point 21 Core		27.2	25.2		
Porthole Samples				24.2	24.6
Core Averages (n)	25.3(4)	26.1(5)	25.7(5)		

homogeneity. However, slight horizontal heterogeneity of the upper column is suggested by the variation observed in vertical-core water contents. The greatest variation is observed at Level 7, where an average 26.1 ± 3.3% water content is measured (Table 14). Between the second and third porthole determinations (i.e., in the last 18 weeks of the ^{14}C study), the Level 2 water content declined by 6.7%. This decline is consistent with determinations made for the Level 8 porthole and its nearest vertical core subsample (i.e., Level 8 of core taken at Point 17), which indicates an upper column decline of 2.3% (from 27.9 to 25.6 vol%). Results of gravimetric determinations indicate that average water content increased ~4% (i.e., from ~26 to ~30 vol%) during the 23 weeks before and 32 weeks after the ^{14}C injection. The water content during these weeks is of most significance, because of the rapid discharge of ^{14}C following the injection. Results of gravimetric determinations indicate that the average volumetric water content during this time was ~28 vol%. During the last 18 weeks of the study, the water content returned to a range consistent with that determined before the cocktail injection (i.e., between 24 and 27 vol%).

4.1.1.2 Bulk Density Determinations. Results of bulk density determinations are given in Table 15. The bulk densities of vertical cores from Points 9 and 21 were not calculated due to uncertainty of core volumes resulting from incomplete core recovery. Settling was not apparent during the study; therefore, density differences observed between the two coring dates are believed due to coring location (i.e., porthole versus center of column) rather than column settling. The horizontal cores were extracted from portholes where control of packing density was less easily achieved. Therefore, densities of vertical cores are assumed more representative of the column at the time of the tracer studies. Upper and lower core average densities (Table 15) are consistent with densities recorded for these levels (i.e., surface-to-Level 7 and Level 7-to- Level 6) during column packing (Table 1). Results of post-study bulk density determinations, by coring, are generally consistent with the average bulk density (1.31 ± 0.05 g cm^{-3}) calculated during column packing.

4.1.1.3 Mass Balance. An approach based on mass balance is, perhaps, the most reliable way to determine water content. Using this approach, a 0.4% increase in water content (i.e., from 29.7 to 30.1 vol%) is calculated for the 26 weeks following ^{14}C injection (Table 13). This increase is due to the average 0.27 L day^{-1} greater influent than effluent flow observed during this period. Influent and

Table 15. Core sample bulk density determinations.

Elapse Time and Sample Type	Upper Core Samples (Surface to Level 7)		Lower Core Samples (Level 7 to Level 6)	
	Dry Bulk Density (g cm^{-3})	Wet Bulk Density (g cm^{-3})	Dry Bulk Density (g cm^{-3})	Wet Bulk Density (g cm^{-3})
Week 35				
Level 8 porthole core	1.05	1.29		
Level 2 porthole core			1.19	1.46
Week 107				
Point 1 vertical core	1.28	1.52	1.35	1.60
Point 5 vertical core	1.37	1.63	1.44	1.69
Point 13 vertical core	1.37	1.62	1.34	1.58
Point 17 vertical core	1.32	1.56	1.50	1.78
Average of vertical cores (n=4)	1.34	1.58	1.41	1.66

effluent flow rate time series are presented, with applied effluent lysimeter head, in Figure 12. Although lysimeter suction was held relatively constant, slight variation of effluent flow is observed. The effluent flow rate gradually converges with the influent rate after ^{14}C injection (Figure 12). This change of effluent flow is believed due to long term changes in the hydraulic potential gradient and/or lysimeter permeability. A decline in water content of 0.8% (i.e., from 30.1 to 29.3 vol%) is calculated for the last 24 weeks of the study (Table 13). This decline results in a water content that is within 0.4% of that calculated for the ^{14}C injection date. Given the reliability of the cumulative mass balance approach and this relatively small water content fluctuation, water content is believed to have remained effectively constant during the transport study (Figure 13) at 30 vol% (± 1 vol%).

4.1.1.4 Matric Potential. The moisture characteristic curve (MCC) and tensiometer total hydraulic head are given in Figure 14a and b. To aid interpretation, applied effluent lysimeter head is included in the tensiometer plot. Initially, a brief period of upper column (Levels 5, 6, and 7) drainage and Level 1 wetting was observed (Figure 14b). This may be due in part to either slight drainage of upper levels, following reduction of the hydraulic flux from ~5 to ~1 L day^{-1}, and the wetting of the column bottom or to tensiometer conditioning. Variations in the hydraulic gradient due to changes in lysimeter suction are most pronounced at Level 1. With relatively constant suction, the hydraulic head at Level 1 approached values comparable to those of Level 5, 6, and 7 immediately before ^{14}C injection at Week 57.

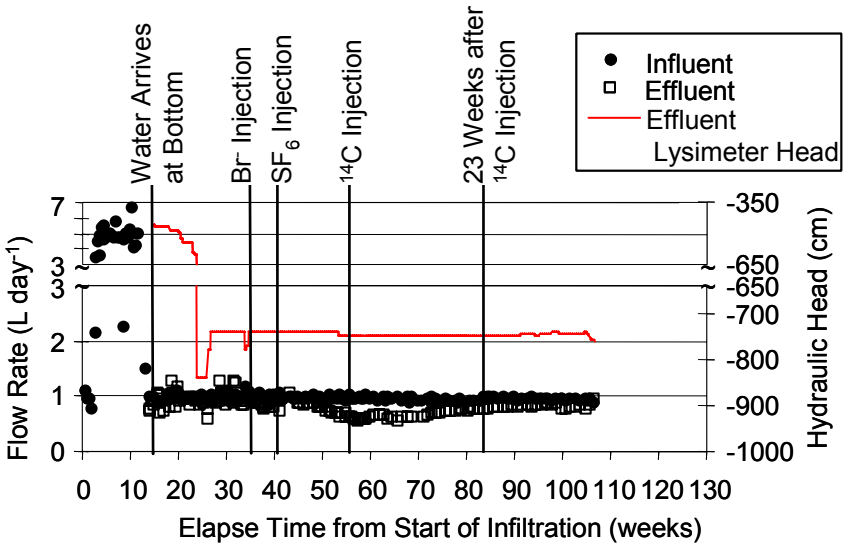

Figure 12. Influent and effluent flow rates with effluent lysimeter head.

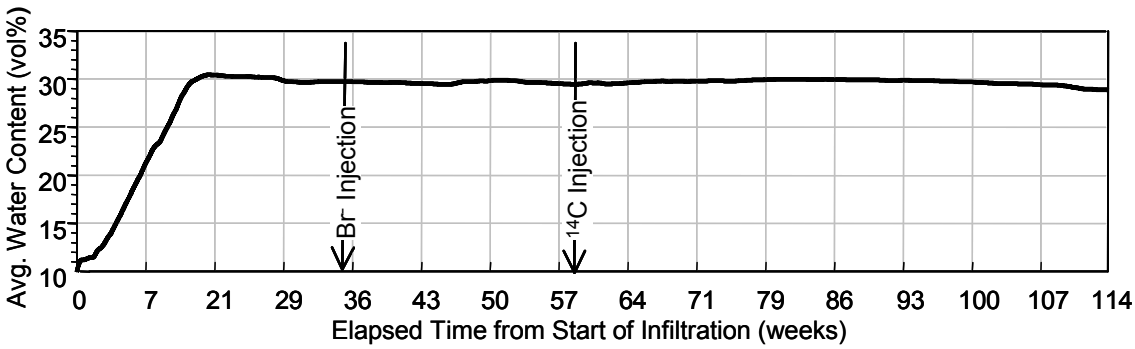

Figure 13. Mass balance based cumulative volumetric water content.

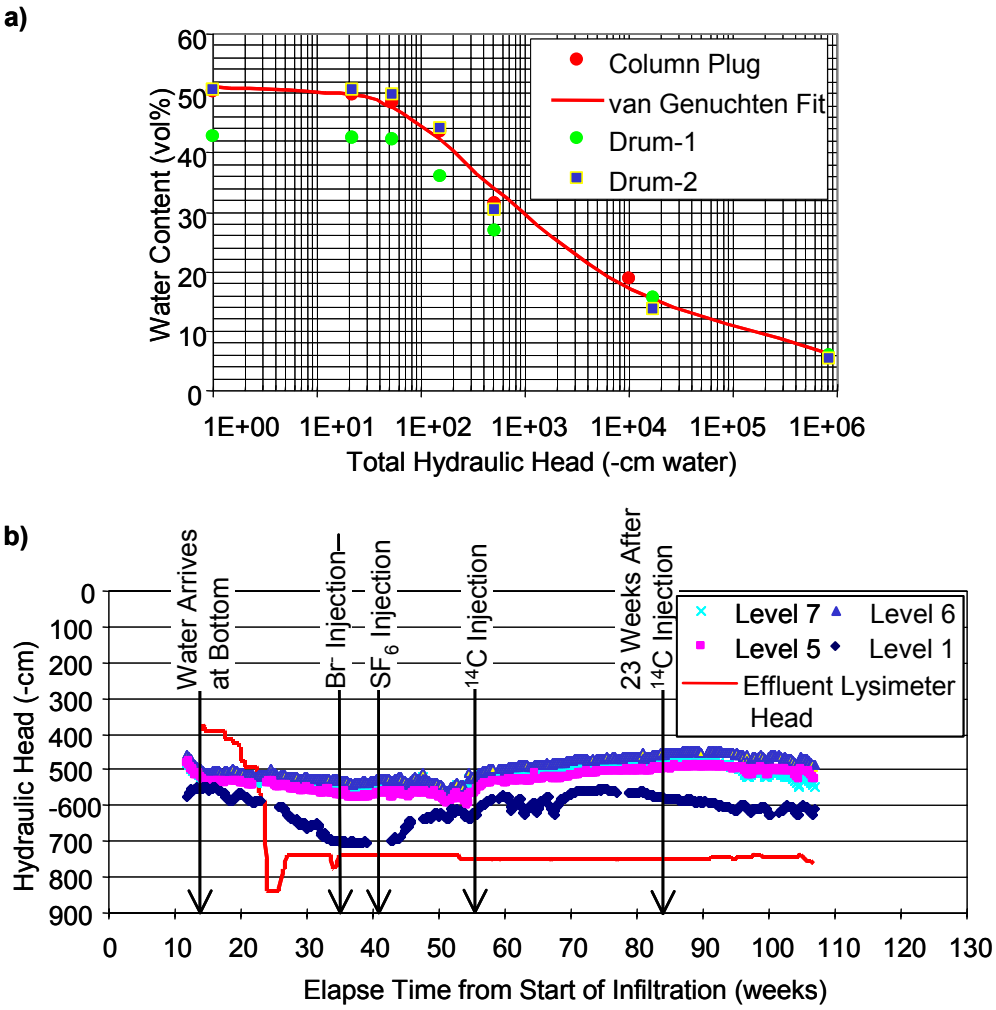

Figure 14. Moisture characteristic curve (a) and tensiometer and effluent lysimeter hydraulic heads (b).

Extracting water to make the isotope injectate lowered the hydraulic head during the 10 days prior to ^{14}C injection (Figure 14b). Following injection, the effluent flow rate was supplemented by extracting water from the sampling lysimeters at Level 0 on three occasions. The extraction cycles appear as three successive peaks and valleys at Level 1 between 60 and 70 weeks (Figure 14b). While these hydraulic head fluctuations were not observed above Level 1, we stopped supplemental water extractions to prevent potential changes of upper level seepage velocity that might affect the aqueous phase transport rate. The supply of influent and extraction of effluent were both paused while column was cored; the response of the hydraulic gradient was observed in tensiometer readings at Week 107 (Figure 14b). If we ignore the MCC provided by the van Genuchten fit and consider the drum and plug sample values (Figure 14a), tensiometer measurements yield a ~27 to ~31 vol% water content (29 vol% average) for the mean hydraulic head (-540-cm) at the time of ^{14}C injection. The lack of sensitivity in tensiometer-MCC-based approaches produces a similar range of water contents for the mean hydraulic head (-546-cm) recorded 50 weeks after the cocktail injection. This lack of sensitivity produces a consistent water content estimate of 29 vol% during the entire transport study (Table 13). While tensiometer-based estimates are generally consistent with gravimetric and mass balance approaches, fluctuations of water content are not observed due to the lack of sensitivity. For this reason, the tensiometer data is most useful as an indicator of relative hydraulic potential rather than water content.

4.1.1.5 Reflectometry. TDR water content data are plotted in Figure 15a. These measurements have been corrected for pore water electrical conductivity and thermal interference using Equation (9). A 10% volumetric water content was recorded by TDR probes prior to application of water. This is the only measure of initial (packing) water content. (The sediment had been stored approximately 2 years.) A 10% packing water content is reasonable, given the measured ~14 to ~16% range at the time of column packing. With initiation of water flow, four probe responses were noted in the TDR time series. First, the probes respond to changing pore water conductivity with passage of the infiltration front. Second, the Level 1 probe consistently produces questionably high readings. Third, all probes respond to thermal interference in excess of the probe's correction limit. Fourth, the readings of all probes instantaneously increase then gradually return to near initial values. The apparent cause of each of these responses is next discussed.

The probes respond to changing pore water conductivity as the infiltration front moves. This response produced artificial rises and declines in water contents (Weeks 5 through 20, Figure 15a). Highly soluble solids leach from sediment surfaces as water infiltrates. As the water percolates down, dissolved solids are transported and concentrated along the infiltration (wetting) front, causing a spike of relatively high ionic strength pore water. Because the TDR probes were calibrated to record changes of water content at a constant and relatively low aqueous ionic strength, breakthrough curves were observed for each probe with passage of the ion spike. As the spike eluted, relatively constant conductivity, representative of probe calibration conditions, was established by the slow and steady leaching of soluble solids and the probes began to respond to changes of conductivity due to water content. The TDR probe time series is expanded in Figure 15b to show the ion spike breakthrough curves. Water sampling began as the wetting front approached the bottom of the column. Thus, conductivity breakthrough curves were only recorded at levels below 2. The ion spike's arrival and elution is observed in pore water conductivity measurements at Levels 1, 0C, and 0G (Figure 15c). TDR readings cannot be corrected for the ion spike without knowing the water content of the spike.

Following passage of the ion spike, the Level 1 TDR probe consistently recorded water contents that were considerably greater than those recorded by probes at upper levels (Figure 15a). The Level 1 TDR probe is located ~15-cm above the west effluent lysimeter pair (Figures 5 and 6). Elevated water content near this probe could be due to the use of a common effluent lysimeter suction source and water collection manifold. Applying a uniform suction at all lysimeters could limit water extraction and increase solute residence time near lysimeters having relatively low hydraulic conductivity. However, the consistency of Level 0C and 0G conductivity breakthrough curves (Figure 15c) suggests similarity of residence times for both lysimeter pairs. Therefore, it is believed that the Level 1 TDR probe readings are erroneous. This response, or malfunction, may be due, at least in part, to improper pre-emplacement calibration or accidental alteration of the waveguide separation distance during emplacement.

All probes indicated a rise and decline of water content during the summer months (approximately Weeks 50 and 100, Figure 15a). This is due to thermal interference that approached the correction limit (1.6%); see Section 3.3.3.4, Water Content Reflectometers, for more detail. Because this thermal interference is minimal at Levels 4, 5, and 7, and the TDR measurements during cool weather periods of laboratory thermal stability are believed to represent those during the spike, additional thermal correction is unnecessary. (The pronounced response of the Level 1 probe to this thermal interference, compared to the Level 4, 5, and 7 probes, is further evidence of its malfunction.)

The fourth notable response—that the readings of all probes instantaneously increase then gradually return to near initial values—involves two step-changes recorded by probes at Levels 4, 5, and 7 between Weeks 60 and 80, Figure 15a. This response is believed to be due to a hardware connection fault. It is followed by a gradual return to values near those recorded prior to these step changes.

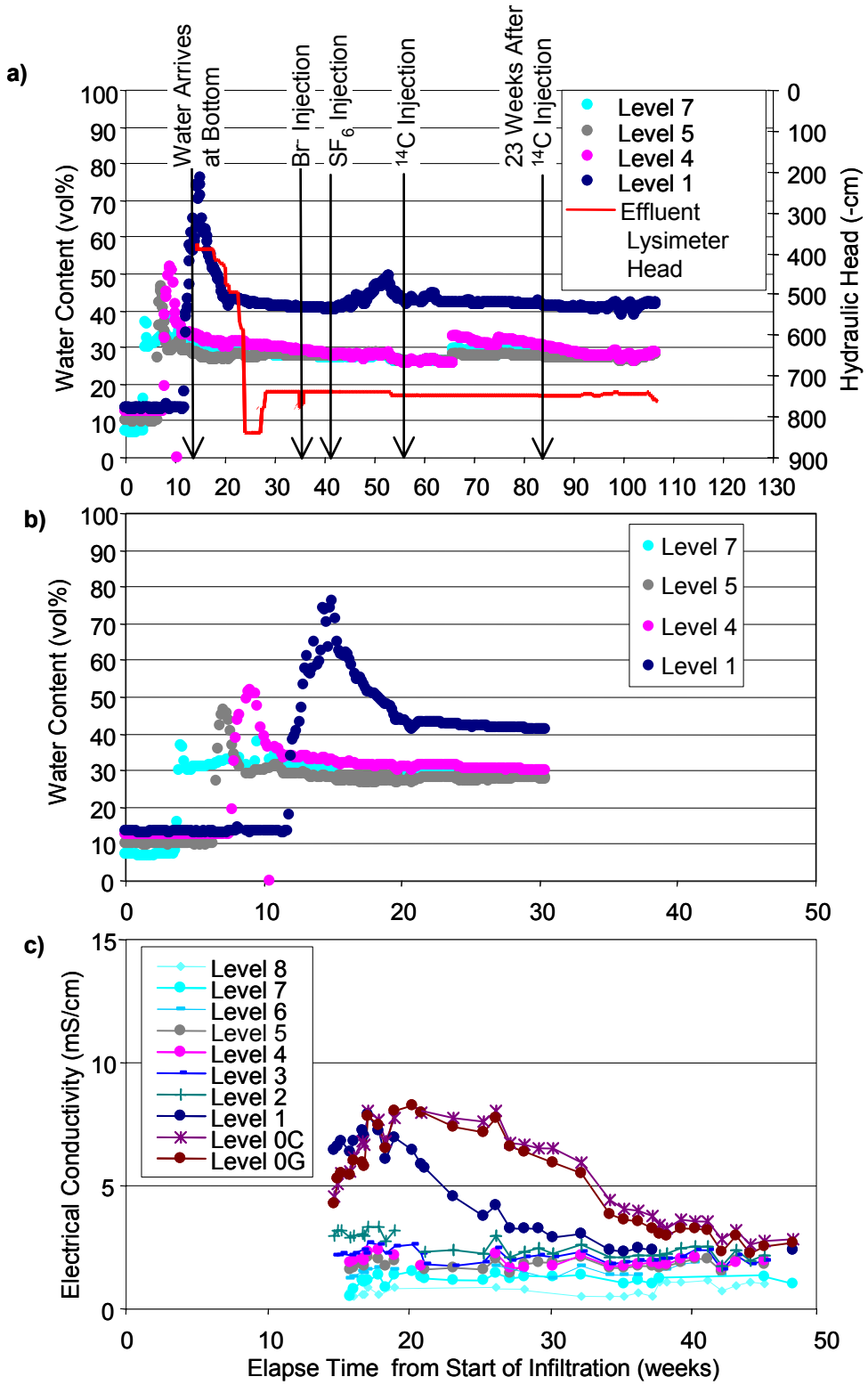

Figure 15. Reflectometer (TDR probe) data. (a) volumetric water content and effluent-lysimeter hydraulic head, (b) wetting/dissolved-salts front breakthrough curves recorded by TDR probes, and (c) electrical conductivity time series.

The Level 4, 5, and 7 TDR probes yield an average 26.0% volumetric water content on the day of ^{14}C injection. While measurements following the assumed hardware fault are somewhat questionable, probe readings return to an average 28.4% (± 2%) following those events. With the exception of transient pore-water conductivity, thermal, and hardware fault events that produce errant readings, TDR water content measurements are generally consistent with those made using gravimetric, tensiometer, and mass balance methods.

4.1.2 Water Chemistry

For this study, chemical steady state is defined to be an extended period over which water chemistry at each column level is constant. Slow leaching of dissolved species and thermally induced fluctuations of microbially generated CO_2 affect maintenance of steady-state conditions. However, pH, electrical conductivity, and alkalinity measurements indicated near steady-state conditions for three months before the ^{14}C, uranium, and tritium cocktail was injected. Linear fits of pH, electrical conductivity, and alkalinity measurements during these three months produce respective slopes of -4×10^{-4}, -3×10^{-4}, and 1×10^{-2}. Water chemistry is given, relative to bromide and ^{14}C injections, in Table 16. The electro neutrality (% error) in Table 16 is calculated as

$$\left(\sum Cations - \sum Anions\right) / \left(\sum Cations + \sum Anions\right) * 100 ,$$

where *Anions* and *Cations* are in units of milliequivalence. While observed fluctuations of ionic species are relatively insignificant to the ^{14}C transport study, changes in $CO_{2(gas)}$ will affect aqueous/gas partitioning of ^{14}C. However, we were unable to fully constrain microbial CO_2 production due, largely, to fluctuations of sediment temperature. Table 17 gives pH, bicarbonate alkalinity, and $CO_{2(gas)}$ concentrations measured six days before the isotope injection to establish the initial chemical state for the transport study. Average pH, bicarbonate alkalinity, CO_2, and O_2 measurements recorded during the 50-week transport study are given in Table 18. A discussion of water chemistry and aqueous species analyses follows.

Measurement of pH, electrical conductivity, and alkalinity began as the wetting front approached the bottom of the column. Therefore, the chemistry of the passing front was not recorded at upper levels. The most notable aspect of these data is for column wet up. An initial increase in conductivity occurred as highly soluble solids accumulated along, and traveled with, the wetting front. This effect is pronounced in conductivity measurements for Levels 1 and 0 (Figure 15c). At the column's bottom, solute residence time increases because excess dissolved salts are extracted via nonuniform flow paths converging at effluent lysimeters located ~15-cm above the bottom. The increased residence time is evident in the relatively persistent tail of the Level 0 (i.e., the effluent lysimeter level) conductivity breakthrough curve (Figure 15c). As the excess dissolved salts elute, the slow and steady leaching of soluble solids established relatively constant conductivity for the duration of the transport study.

The elimination of excess dissolved solids is apparent in a comparison of ionic species over time. Aqueous chemistry and CO_2 sediment gas concentration profiles are given for 26, 34, 51, 79, and 106 weeks after start of water infiltration in Figure 16. From these profiles, excess dissolved salts are shown to be eliminated and relatively constant ion concentrations established prior to and after the ^{14}C injection. We found relatively high nitrate (NO_3^-) concentrations among the ionic species eliminated. Elevated NO_3^- concentrations are not uncommon in desert vadose zone sediments (Hartsough et al. 2001, Walvoord et al. 2003).

Results of dissolved carbon analysis show organic carbon, at Level 0, to be reduced by a factor of 10.8 over the 90-week sampling interval (Table 19). This reduction is believed due to both microbial metabolism and elution by effluent water.

Table 16. Water chemistry and pore gas CO_2 concentration profiles relative to Br^- and isotope injections.

	Level	Ca (mg/L)	Fe (mg/L)	K (mg/L)	Li (mg/L	Mg (mg/L)	Na (mg/L	Sr (mg/L)	F (mg/L)	Cl (mg/L)	NO_3 (mg/L)	SO_4 (mg/L)	HCO_3 (mg/L)	Electro Neutrality (% error)	pH	CO_2 (vol%)	Cond (mS/cm)
															(1/10/02)	(1/10/02)	(1/10/02)
Week 26 (1/10/02)	8	90.1	0.022	2.79	0.008	23.66	6.83	0.53		1.90	1622.2	25.33	366	0.01	7.42	1.71	0.86
	7	152.7	0.026	3.94	0.016	41.55	19.66	0.85		2.09	1662.1	28.40	622	1.11	7.19	5.01	1.45
	6	188.8	0.038	4.64	0.020	53.09	23.31	1.10		2.41	2079.7	30.21	744	1.12	7.16	7.33	1.76
	5	226.8	0.050	5.32	0.024	63.68	25.94	1.29		2.16	1772.5	36.39	744	0.82	7.10	8.75	2.06
	4	248.6	0.044	5.14	0.024	70.40	26.90	1.44		2.05	1841.5	54.24	915	0.77	7.04	9.98	2.22
	3	288.2	0.054	6.11	0.028	80.48	30.12	1.55		2.11	1814.4	97.95	927	0.65	7.02	10.96	2.48
	2	340.9	0.056	6.22	0.030	96.20	32.80	1.94		2.81	2026.4	175.71	903	0.64	6.98	11.81	2.94
	1	489.8	0.074	8.13	0.042	133.10	41.09	2.82		12.45	2710.5	142.94	842	0.59	6.92	13.00	4.21
	OC	995.8	0.114	11.40	0.064	243.00	59.39	5.46		48.24	4982.5	78.59	744	-2.34	6.8		8.03
	OG	1053.0	0.122	11.67	0.066	256.50	61.23	5.90		48.39	5449.4	78.10	732	-0.07	6.83		7.75
Week 34 (3/7/02)															(3/13/02)	(3/7/02)	(3/13/02)
	8	106.5	0.026	3.25	0.012	27.39	7.20	0.54			52.4	12.90	397	1.86	7.29	2.37	0.53
Bromide Injection on 3/13/02	7	160.6	0.038	4.41	0.020	46.80	20.32	0.90		0.99	137.3	19.25	645	-1.23	7.08	6.83	0.99
	6	209.6	0.042	5.23	0.026	58.34	22.96	1.19		1.65	205.7	20.78	778	-0.34	7	9.66	1.36
	5	261.8	0.054	5.88	0.030	72.31	26.23	1.38		1.83	328.8	27.18	849	1.26	7.02	11.15	1.67
	4	277.6	0.056	5.99	0.030	77.02	27.00	1.55		1.58	317.2	35.45	927	1.13	7	12.64	1.73
	3	301.0	0.060	6.49	0.034	83.43	28.44	1.65		1.52	354.4	56.89	952	1.71	6.99	13.71	1.86
	2	343.2	0.064	6.69	0.034	96.89	31.14	1.93		1.80	432.3	123.31	983	1.85	6.98	14.64	2.08
	1	389.8	0.070	7.07	0.038	110.40	34.92	2.09		3.35	568.9	161.29	998	2.14	6.92	15.63	2.33
	OC	682.7	0.100	10.56	0.058	177.70	47.21	3.75		25.54	2114.0	111.38	895	-0.63	6.82		4.06
	OG	605.3	0.094	10.17	0.054	159.60	44.09	3.34		22.24	1781.5	114.47	894	-0.82	6.9		3.60

Table 16. (continued).

	Level	Ca (mg/L)	Fe (mg/L)	K (mg/L)	Li (mg/L	Mg (mg/L)	Na (mg/L	Sr (mg/L)	F (mg/L)	Cl (mg/L)	NO_3 (mg/L)	SO_4 (mg/L)	HCO_3 (mg/L)	Electro Neutrality (% error)	pH	CO_2 (vol%)	Cond (mS/cm)
Week 51 (7/3/02)															(7/3/02)	(7/4/02)	(7/11/02)
	8	115.1	0.017	3.85	0.014	28.27	6.79	0.57		1.02	75.0	13.37	387	3.56	7.68	3.14	1.06
6 weeks before ^{14}C injection (8/12/02)	7	175.2	0.022	5.22	0.022	44.38	16.08	1.02		0.83	144.1	17.63	599	1.61	7.04	9.28	1.44
	6	217.8	0.031	6.15	0.028	55.69	24.01	1.16		0.83	199.7	23.53	743	2.36	7.22	13.23	1.74
	5	266.0	0.040	7.02	0.030	70.64	26.75	1.50		2.09	295.3	24.68	843	4.00	7.26	15.58	1.98
	4	297.7	0.041	7.20	0.036	79.58	29.32	1.62		1.93	390.1	30.45	910	-3.81	7.04	17.53	2.13
	3	323.4	0.045	6.83	0.034	85.82	30.59	1.88		1.88	472.2	36.49	906	3.26	7.13	18.95	2.30
	2	347.4	0.046	8.36	0.043	94.06	32.75	1.91		2.02	527.2	63.20	950	3.66	7.03	19.96	2.38
	1	370.6	0.048	7.28	0.037	99.79	34.21	2.15		2.07	501.0	107.73	1002	1.78	7.1	20.79	2.485
	OC	435.4	0.067	9.23	0.053	117.40	38.84	2.38		4.32	668.6	145.67	1033	5.00	7.01		2.67
	OG	427.0	0.055	8.67	0.046	113.60	37.37	2.47		3.84	672.0	150.94	980	3.01	7.1		2.59
Week 79 (1/16/03)															(1/16/03)	(1/16/03)	(1/16/03)
	8	73.5	0.001	1.74	0.013	18.81	10.35	0.47	0.31	1.05	41.5	11.9	371	-10.34	7.28	1.60	0.55
22 weeks after ^{14}C injection	7	130.0	0.001	2.93	0.019	32.33	16.41	0.74	0.22	1.05	943.8	19.4	517	-2.60	7.07	4.59	0.90
	6	157.8	0.001	3.68	0.013	45.34	24.38	1.01	0.23	0.96	192.4	27.6	608	-3.45	7.00	6.59	1.21
	5	199.3	0.004	4.32	0.026	54.19	30.11	1.19	0.12	1.45	128.2	30.9	730	3.59	7.01	7.80	1.54
	4	243.5	0.003	4.37	0.026	59.66	29.54	1.35	0.07	1.32	373.3	34.2	742	-1.18	6.98	8.85	1.71
	3	249.8	0.003	4.89	0.029	71.25	34.33	1.53	0.21	1.48	479.7	37.3	769	-2.86	6.99	9.70	1.90
	2	270.4	0.002	5.11	0.029	79.01	34.81	1.74	0.06	1.81	523.5	47.1	798	-2.06	6.94	10.50	2.09
	1	301.4	0.004	5.84	0.032	94.77	34.50	1.92	0.11	2.31	621.7	49.7	825	-0.27	6.91	11.32	2.32
	OC	336.7	0.006	6.52	0.032	108.27	43.63	2.16	0.05	2.62	689.7	103.7	817	2.00	6.85		2.65
	OG	372.2	0.005	6.04	0.032	111.91	42.58	2.23	0.12	3.52	735.5	122.1	837	2.71	6.92		2.69

Table 16. (continued).

	Level	Ca (mg/L)	Fe (mg/L)	K (mg/L)	Li (mg/L	Mg (mg/L)	Na (mg/L	Sr (mg/L)	F (mg/L)	Cl (mg/L)	NO_3 (mg/L)	SO_4 (mg/L)	HCO_3 (mg/L)	Electro Neutrality (% error)	pH	CO_2 (vol%)	Cond (mS/cm)
Week 106 (7/24/03) 49 weeks after ^{14}C injection.															(7/24/03)	(7/24/03)	(7/24/03)
	8	75.3	0.004	3.08	0.014	20.91	4.99	0.43	0.48	3.63	56.6	12.13	366	-11.52	7.46	2.16	0.059
	7	130.3	0.004	4.42	0.021	35.06	9.11	0.72	0.40	3.39	112.8	16.65	534	-5.35	7.18	6.19	0.92
	6	156.5	0.014	4.98	0.140	44.87	17.27	0.86	0.43	3.23	166.2	23.28	661	-6.38	7.09	8.78	1.11
	5	190.4	0.005	5.87	0.028	55.25	24.13	1.07	0.28	2.90	230.8	29.94	710	-2.57	7.18	10.28	1.4
	4	211.0	0.008	5.80	0.028	60.97	25.40	1.15	0.00	2.92	380.5	33.79	769	-7.42	7.09	11.65	1.51
	3	469.4	0.006	6.06	0.030	65.84	27.35	1.18	0.00	3.56	357.1	33.29	781	2.23	7.13	12.72	1.66
	2	262.9	0.006	6.38	0.031	77.92	29.74	1.40	0.00	3.22	487.5	42.76	847	-3.89	7.06	13.56	1.88
	1	291.9	0.005	6.30	0.032	86.33	31.06	1.62	0.00	3.43	584.4	45.75	871	-3.19	7.05	14.44	2.08
	OC	344.6	0.009	7.19	0.035	94.26	39.53	1.77	0.00	4.31	689.7	75.16	964	-3.08	7.06		2.29
	OG	317.2	0.008	6.92	0.033	92.79	35.02	1.79	0.00	4.32	715.8	73.66	971	-7.19	7.17		2.34

Table 17. pH, bicarbonate alkalinity, and CO_2 six days prior to ^{14}C injection.

	Column Level							
	1	2	3	4	5	6	7	8
pH (± 0.3%)	6.91	6.94	6.99	7.00	7.03	6.97	7.09	7.36
HCO_3, mg L^{-1} (±10 mg L^{-1})	998	964	911	834	886	809	627	399
CO_2, vol% (± 1%)	16.21	15.13	14.03	12.78	11.18	9.33	6.42	2.16

Table 18. Average pH, CO_2, O_2, and bicarbonate profiles during transport study (Weeks 56 through 106 of water infiltration).

Column Level	Depth from Surface (cm)	pH (± 0.3%)	CO_2 (± 2 vol%)	O_2 (± 1 vol%)	HCO_3 (±10 mg L^{-1})
8	15.2	7.39	1.73	19.25	361
7	45.7	7.16	4.99	15.94	552
6	76.2	7.08	7.12	13.72	676
5	106.7	7.07	8.36	12.59	745
4	137.2	7.03	9.53	11.47	773
3	167.6	7.03	10.44	10.55	798
2	198.1	6.99	11.25	9.72	831
1	228.6	6.98	12.08	8.78	880
OC	243.8	6.94	—	—	901
OG	243.8	6.97	—	—	892

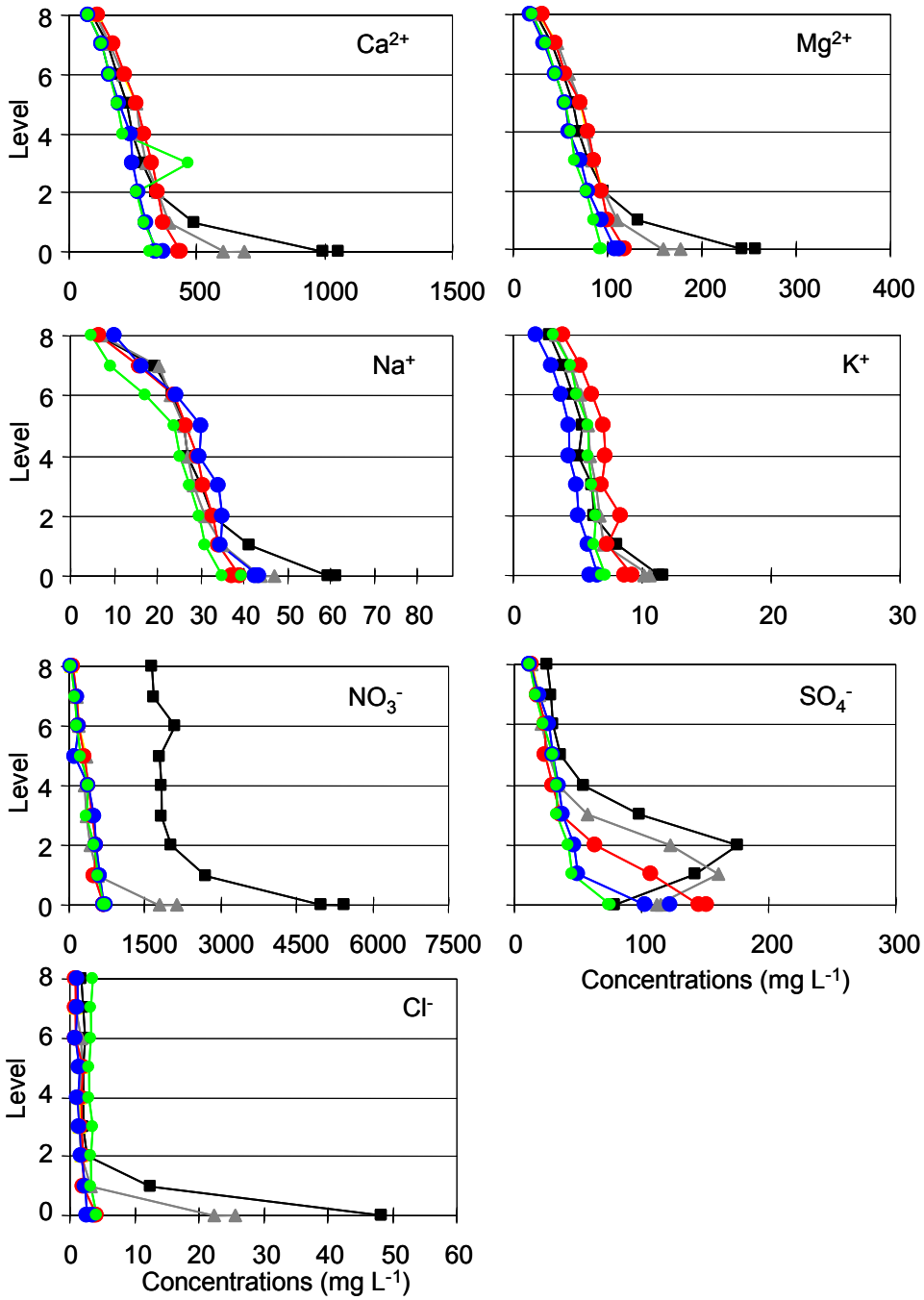

Figure 16. Aqueous chemistry and sediment CO_2 gas profiles (legend on next page).

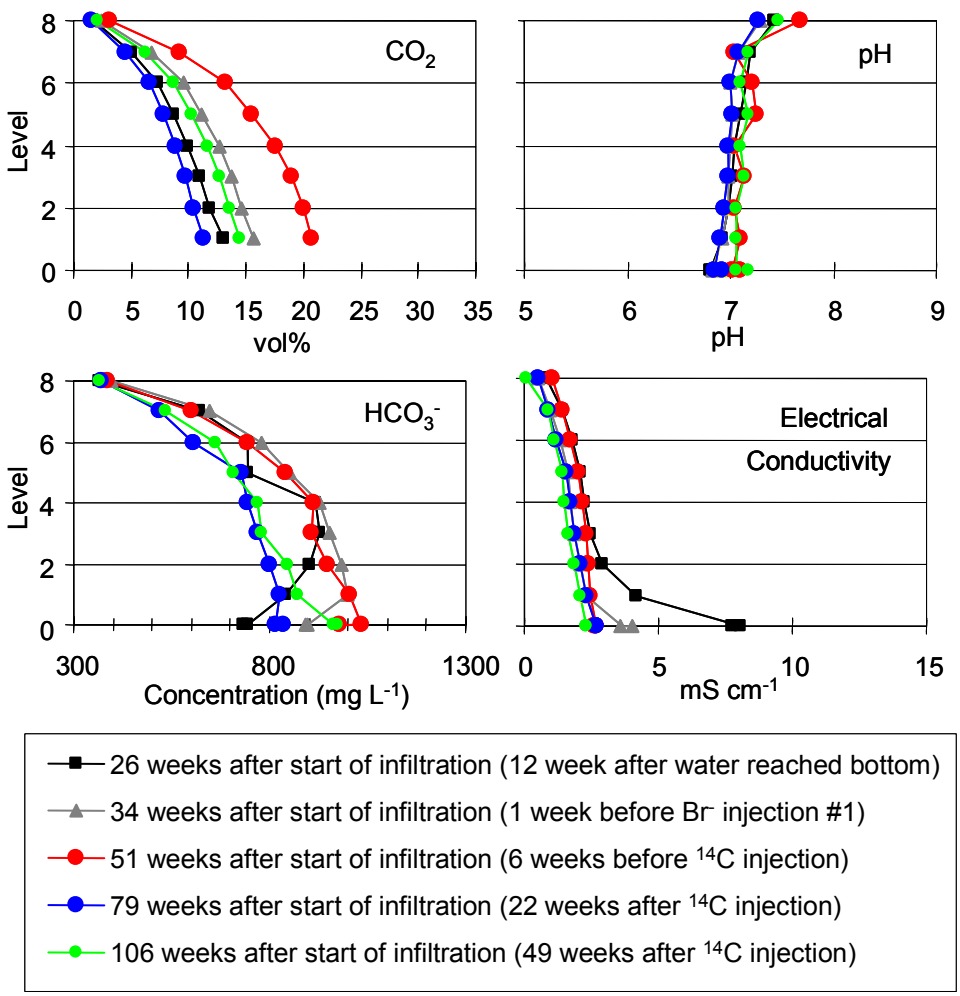

Figure 16. (continued).

Table 19. Dissolved carbon results.

Elapse Time	Level	Total Carbon (mg L^{-1})	Inorganic Carbon (mg L^{-1})	Organic Carbon (mg L^{-1})
Week 16 (11/1/01) or 41 weeks before ^{14}C injection	0C-0G	326	143	183
Week 106 (7/24/03) or 49 weeks after 14C injection	0C	168	151	17
	0G	195	178	17
	1	164	151	13
	2	167	155	12
	3	155	143	12
	4	152	143	9
	5	146	137	9
	6	130	125	5
	7	113	109	4
	8	71	67	4

4.1.3 CO_2 and O_2 Gas Concentration Monitoring

In the vadose zone, aqueous/gas partitioning of carbonate species is primarily controlled by microbially-generated CO_2. At the SDA, microbial metabolism of organic debris produces sediment gas CO_2 concentrations as high as 10 vol% (Hull and Bishop 2003). Similar CO_2 concentrations were observed during the 12-month transport study (Figure 17). CO_2 and O_2 concentration time series from the start of water application is given in Figure 18. Variations of pore gas CO_2 and O_2 concentrations are primarily due to sediment temperature fluctuations (Figure 19). A narrative about the CO_2 and O_2 concentration time series in Figure 18 is provided next to aid interpretation of these data.

The first notable event affecting the data in Figure 18 was an equipment failure that resulted in the loss of data from Weeks 5 to 11 and 35 to 37. Early in the study, pore gas concentrations were disrupted when excessive suction was applied to the effluent lysimeters and atmospheric air was drawn down through the column from the surface. These disruptions, and resulting rebounds of gas concentration, are observed from Weeks 12 to 16 and 26 to 29.

Temperature fluctuations significantly affected pore gas concentrations. Rising temperatures during summer months stimulated microbial O_2 consumption and CO_2 production. Increased microbial metabolism produced the two relatively large CO_2 peaks and O_2 valleys observed between Weeks 45 and 60 and again at Week 107 (Figure 18). Given the dynamic nature of the sediment temperature and pore gas relationship, and the fact that the laboratory is heated but not cooled, an autumn date was selected for ^{14}C injection to allow ^{14}C migration to be monitored over the longest possible period of temperature stability. The ^{14}C, uranium, and tritium cocktail was injected on August 12, 2002 as declining autumn temperatures allowed pore gas CO_2 to approach pre-summer concentrations. Following the injection, a steady decline in CO_2 and increase in O_2 concentration was observed (Figure 18). The relatively stable sediment temperature and water content (Figures 19 and 13, respectively) over this period of steadily declining CO_2 surface flux (Weeks 65 through 95, Figure 19) suggests the steady depletion of easily metabolized carbon. This depletion is further suggested by the dissolved carbon analysis (Table 19).

Control and measurement of the column's headspace ventilation rate was critical to bulk CO_2 and $^{14}CO_2$ surface flux calculations. Control of the ventilation rate was hampered by internal condensation in

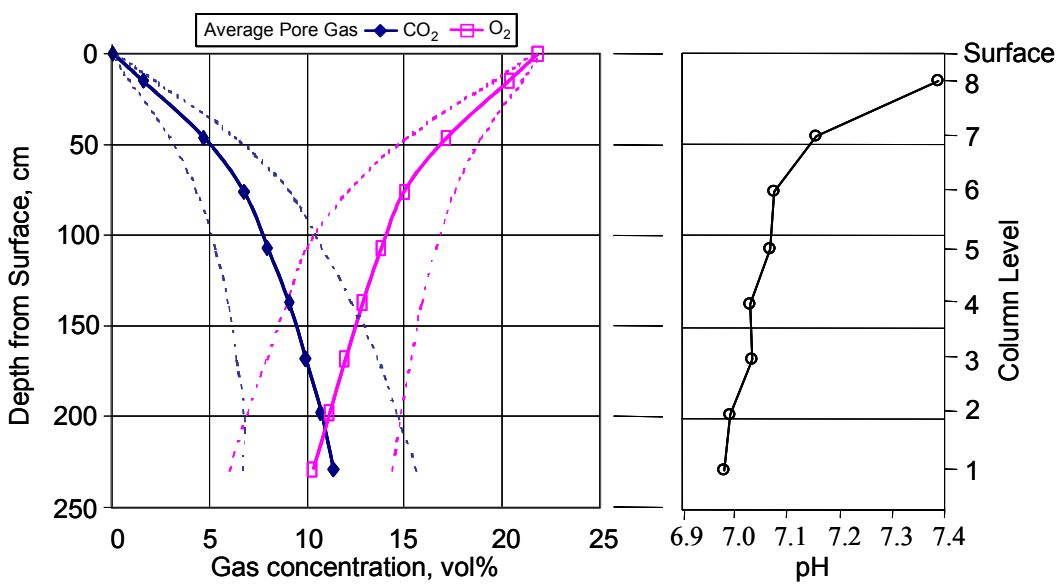

Figure 17. Average CO_2, O_2, and pH profiles during ^{14}C transport study (dotted lines represent gas concentration ranges during the ~107 week study).

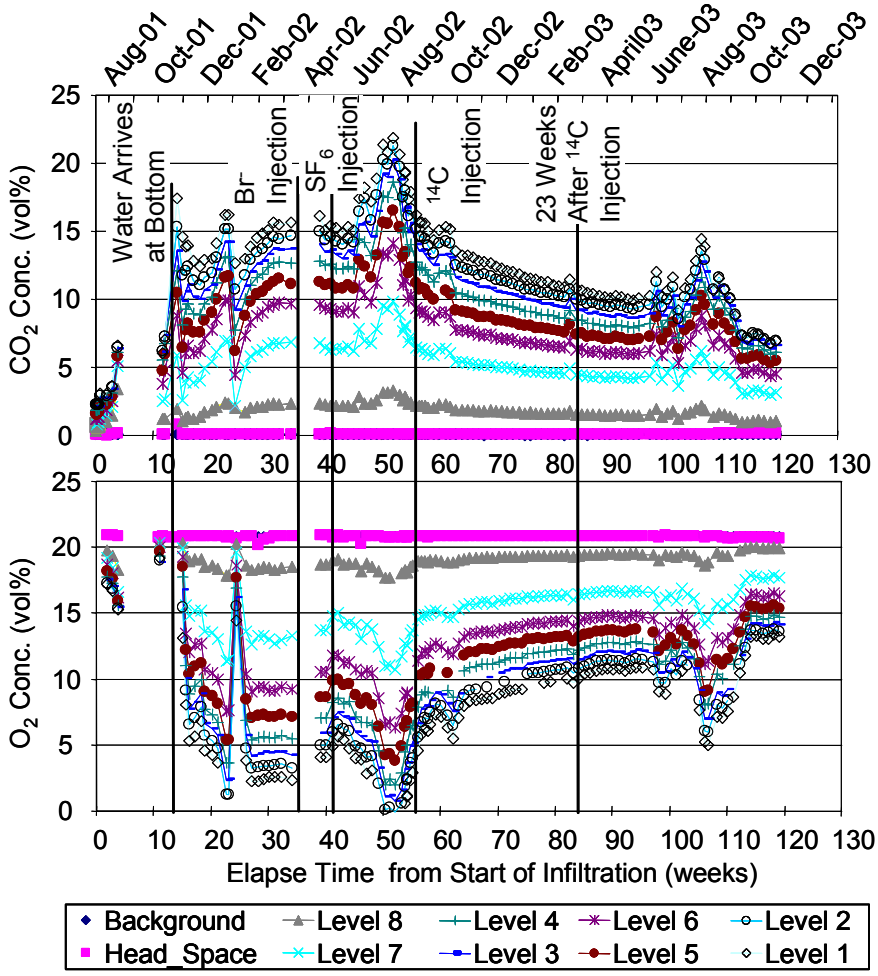

Figure 18. Sediment gas CO_2 and O_2 concentration time series at each column level.

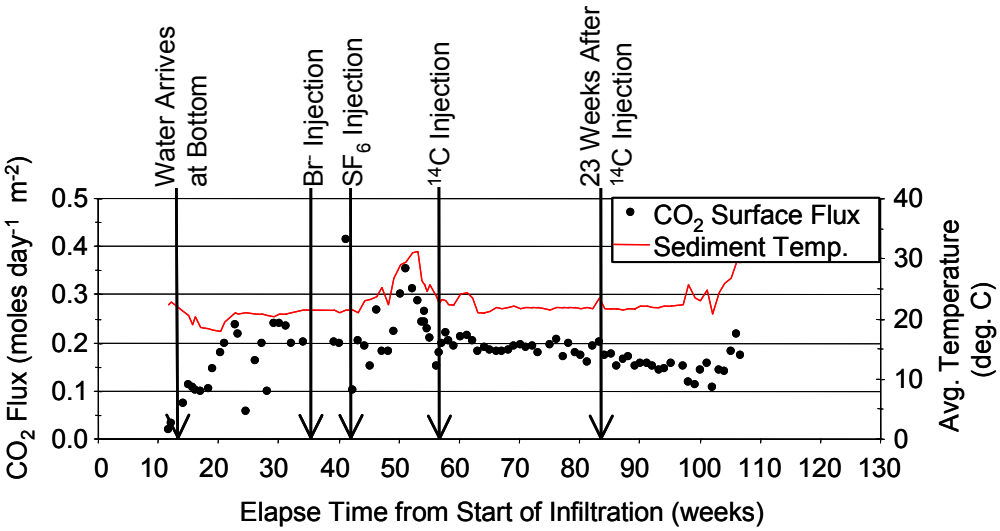

Figure 19. Bulk CO_2 surface flux.

the mass flow controller due to the high relative humidity of headspace gases. Using heat tape to keep controller and tubing surfaces at an elevated temperature was largely effective, but the flow controller did experience condensation and lose control during the later portion of the study. Though the condensation event caused undefined deviation of the headspace ventilation rate, the rate indicated by the controller was consistent with the desired set point value (~7 L min^{-1}). Therefore, calculation of CO_2 surface flux using the flow rate indicated by the controller produces the fluctuations observed between Weeks 75 and 85 (Figure 19). The condensation event may have been due to an inadvertent lowering of controller and tubing surface temperatures, from ~35° to ~25°C. Following this event, water was removed from the controller, surface temperatures were increased, and flow control was reestablished. The electronic controller did not indicate loss of control, which demonstrates the need for independent flow control and measurement validation.

4.2 Biological Assays

The sediment's biological community was not characterized prior to initiation of the transport study. Sediment samples taken in Week 36 from column Levels 2, 3, and 8, are currently undergoing analysis to identify microbial communities. Complete results are not yet available; however, preliminary results indicate a diverse community that changes in structure with depth. Change in community may be due to shifts in CO_2 and O_2 concentration with depth. Upon completion of the transport study, in January of 2004, additional sediment samples were taken from all column levels for biological assay. These samples are currently undergoing analysis and will be discussed in a future report.

4.3 Tracer, Carbon-14, and Uranium Transport

To examine the movement of water, gas, and conservative solute through the sediment, we injected a highly insoluble gas, sulfur hexafluoride, both before and during the water infiltration period, and conservative liquid tracers, lithium bromide and tritium, after reaching a quasi steady-state flow conditions. Data from these experiments is used to estimate characteristics of the unsaturated flow system that affect transport of ^{14}C, including average linear seepage velocity, dispersivity and flow path tortuosity.

To examine reactive transport of uranium (U) and ^{14}C through the sediment, we injected an aqueous cocktail of U and ^{14}C, with the conservative tritium tracer. At the end of the ^{14}C transport study (50 weeks after U injection), uranium had not been detected at the sampling lysimeter located 15.2-cm below the injection plane, suggesting a K_d greater than 2.5 L kg^{-1}. Uranium migration results will be discussed in a subsequent report on the analysis of sediment core subsamples.

4.3.1 Gas Tracer—Sulfur Hexafluoride

The breakthrough curves for the sulfur hexafluoride (SF_6) tracer tests are shown in Figure 20. The similarity of the primary and replicate test curves indicates good reproducibility. During the tests at experimental water content, we evaluated the effect of sampling on SF_6 movement by extracting ~41% more sample gas during the first ~15 h of the primary test than was extracted during the same period of the replicate test. Given this difference in sample gas removal and the consistency of the primary and replicate breakthrough curves (~30% test in Figure 20), gas sampling is believed to have had an insignificant effect on SF_6 movement.

The diffusivity of gas in unsaturated sediments is dependent upon water saturation, which controls tortuosity of the pore space available for gas movement. The ~10 and ~30% volumetric water content tests were performed to collect data needed to estimate the relationship between water content and tortuosity. Comparing the breakthrough curves of the primary tests in Figure 21, the effect of water content is evident. Though virtually identical SF_6 concentrations were used, higher concentration peaks

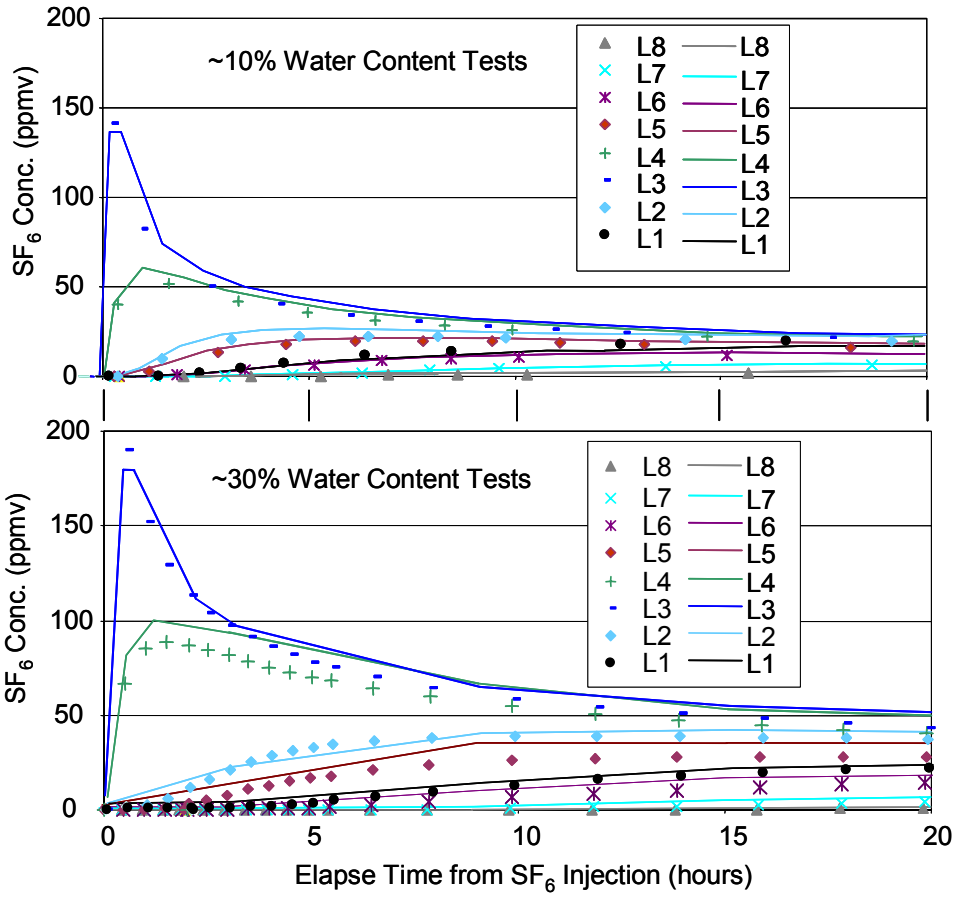

Figure 20. SF_6 concentration in primary and replicate tests at packing (~10%) and experimental (~30%) water contents. (characters = primary tests, lines = replicate tests, L = column level.)

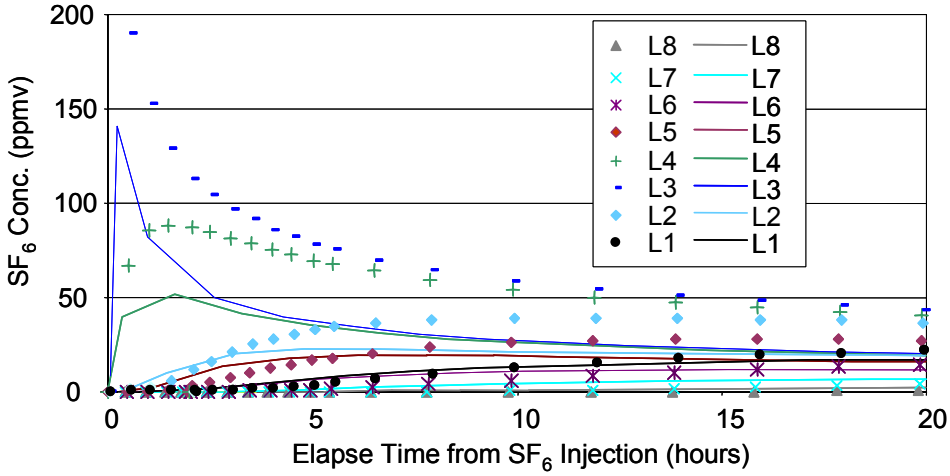

Figure 21. Comparison of primary SF_6 tests at packing (~10%) and experimental (~30%) volumetric water content. (characters = ~30% test; lines = ~10% test).

are observed for the test at ~30% than for the one at ~10%. This is due to minimization of tortuosity at relatively low water content, which allows gas to diffuse from the column faster. However, SF_6 migrated rapidly throughout the column during both tests, with concentration peaks arriving at the nearest levels (Levels 4 and 3) within 0.5 to 2 h of the injections.

The effective gas-phase diffusion coefficient in a porous medium is less than the free-air diffusion coefficient because of the tortuosity of the diffusion paths in the pores. As pores fill with water, the air space available for diffusion decreases, and the tortuosity of the diffusion paths increases. This phenomenon is described by a tortuosity parameter defined by Millington (1959) as:

$$\tau = \frac{\phi_T^2}{\phi_g^m} \tag{12}$$

where

τ	=	tortuosity parameter (dimensionless)
ϕ_T	=	total porosity (cm^3/cm^3)
ϕ_g	=	volumetric gas content (cm^3/cm^3)
m	=	empirical parameter for exponential dependence of diffusion on gas-filled porosity.

Millington (1959) proposed a value of 2.33 for *m*. Hull and Hohorst (2001) performed gas diffusion experiments in air-dried SDA sediments and obtained an *m* value of 2.6 by fitting their experimental data.

To obtain estimates of gas-phase diffusion parameters for the meso scale column, we performed a least-squares fit of the analytical solution to the one-dimensional diffusion equation to measured break-through curves from the column. Comparisons were made to curves from multiple column levels and for tests conducted at ~10% and ~30% water content. The results from fitting the 30% water content test are shown in Figure 22. Using water content as a fitting parameter, this analysis indicates an initial (packing) water content of 11% and an experimental water content of 25%, which are generally consistent with values determined using gravimetric, tensiometer, TDR probe, and mass balance methods. The coefficient of determination for these fits was 0.86 using the *m* value (2.33) recommended by Millington (1959). Additional least-squares analyses of the observed breakthrough curves, using *m* as the fitting parameter, did not significantly improve the observed breakthrough curve fits. Given the good agreement achieved between the data and the analytical solution, we conclude that the standard Millington equation provides an accurate estimate of SF_6 transport and of the relationship between water content and tortuosity in SDA sediments. Furthermore, physical transport parameters determined for SF_6 experiments appropriately describe gas phase diffusion in the current system (Table 20).

4.3.2 Aqueous Tracers—Bromide and Tritium

Bromide (Br^-) breakthrough curves were fit to an analytical solution to the advection dispersion equation (ADE) for equilibrium transport of a conservative ion slug (CXTFIT2, Toride et al. 1995), Figure 23. A good fit (i.e., a mean R^2 of 0.97 and a standard deviation of 0.04) was achieved using this approach. Results of curve fitting, at each column level, indicate one-dimensional flow with an average linear seepage velocity range of 0.46 to 0.55 cm day^{-1} and a dispersion coefficient ranging from 4.6×10^{-6} to 7.9×10^{-6} cm^2 sec^{-1} (Table 21). Calculated hydraulic dispersivities were negligible, ranging from 0 to 7 mm. This is consistent with the results of Hull and Hohorst (2001), who conducted saturated bromide and tritium transport tests with SDA sediment in 31-cm columns and found that dispersivity was on the order of 0.5-mm.

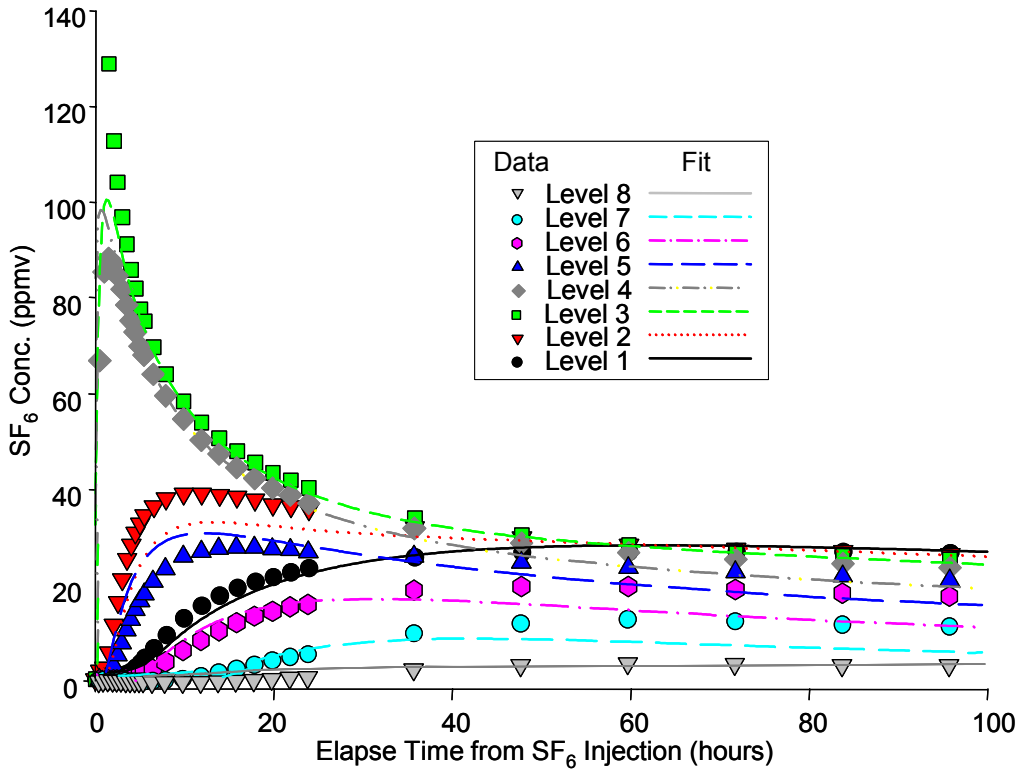

Figure 22. Least-squares fit of SF_6 breakthrough curves at ~30% volumetric water content (i.e., the water content during transport study).

Table 20. Transport parameters used to model SF_6 and Br^- tracer breakthrough.

Conservative Tracer	Aqueous Diffusion Coefficient	Gaseous Diffusion Coefficient
SF_6	—	1.1×10^{-1} cm^2 sec^{-1}
Bromide	1.8×10^{-5} cm^2 sec^{-1}	—

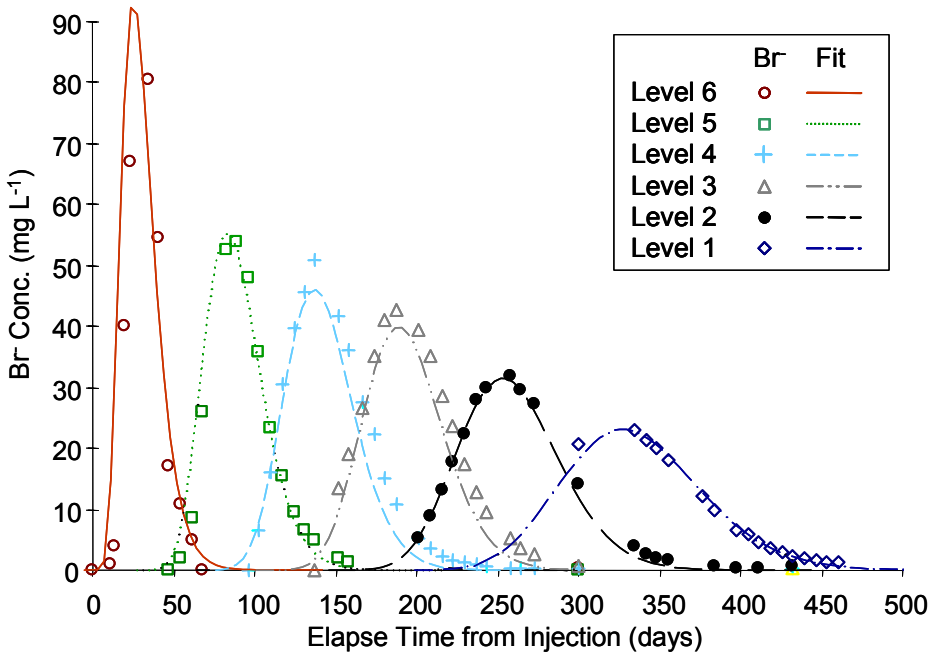

Figure 23. Bromide (Br^-) breakthrough curves and CXTFIT2 fit.

Table 21. Summary of transport parameters determined from CXTFIT2 analysis of conservative tracer tests.

CXTFIT2 Basis	Average Linear Seepage Velocity (cm day^{-1})	Inferred Volumetric Water Content	Hydrodynamic Dispersion Coefficient (cm^2 sec^{-1})	Correlation Coefficient
Injection to Level 6	0.46	0.31	4.6E-06	0.940
Injection to Level 5	0.51	0.28	5.2E-06	0.994
Injection to Level 4	0.55	0.27	5.2E-06	0.949
Injection to Level 3	0.55	0.26	5.4E-06	0.927
Injection to Level 2	0.51	0.27	6.0E-06	0.993
Injection to Level 1	0.51	0.29	7.9E-06	0.994
Averages	0.52	0.28	5.7E-06	0.966

Because Br^- moves into larger pore-water flow paths by mutual Br^- and soil-surface electrostatic repulsion (i.e., anion exclusion), Br^- transport is commonly observed to be accelerated, producing a two-region type of breakthrough curve (Bond et al 1982; James and Rubin 1986). We did not observe this anion exclusion effect. However, we evaluated anion exclusion by first fitting a nonequilibrium type transport solution to the ADE. This approach did not significantly improve the Br^- breakthrough curve fits. Next, we divided the applied hydraulic flux of 1-L day^{-1} (or 0.15-cm^3 cm^{-2} day^{-1}) by the mean linear Br^- seepage velocity (0.52-cm day^{-1}) and estimated a 28% (± 3%) average volumetric water content during the ^{14}C transport portion of the study (Table 21). This water content is consistent with TDR, mass balance, and gravimetric determinations. Therefore, we believe Br^- acceleration is insignificant in these transport measurements, which validates the use of Br^- data in determining physical transport parameters (Table 20).

We also estimated water content using the tritium (^3H) tracer test data. We divided the applied hydraulic flux (0.15-cm^3 cm^{-2} day^{-1}) by the mean linear ^3H seepage velocity (0.38-cm day^{-1}) and estimated a ~40% average volumetric water content. This water content is inconsistent with estimations based on SF_6 tracer, Br^- tracer, TDR, gravimetric, and mass balance approaches. Therefore, we disregard the ~40% water content suggested by the ^3H data and base our water content estimation on the other approaches. From these independent methods, we selected a most probable volumetric water content of ~28% during the transport experiments.

In aqueous systems, tritium (^3H) readily partitions into water, as ^3H_2O. Therefore, the ^3H transport velocity is expected to be equivalent to that of water. Comparing the Br^- and ^3H breakthrough curves in Figure 24 shows that the rate of ^3H transport is significantly slower than that of Br^-. Validation of the Br^- data suggests that the difference in rate is due to ^3H retardation. We conducted a second tracer test to confirm this unexpected retardation of ^3H, an assumed nonpartitioning conservative tracer. Results of the combination $^3H/Br^-$ tracer injection (not presented in this report), initiated in Week 94, confirm the apparent ^3H retardation. Inconsistencies of ^3H and Br^- transport could be explained, at least in part, by tracer losses. However, conservation of ^3H and Br^- mass was confirmed through fitting the ADE to ^3H and Br^- breakthrough curves using CXTFIT2. Alternatively, the inconsistencies could be an artifact of residual contamination of sampling lysimeters. However, apparent ^3H retardation was confirmed by the combined ^3H and Br^- tracer test, and residual contamination would be expected to have an equivalent effect on both ^3H and Br^- samples. The inability to explain apparent ^3H retardation by experimental method or design errors led us to conduct a brief literature search. We found that although precipitation and sorption processes are not expected to significantly affect the movement of ^3H, the potential for fixation of isotopic water on clays and other hydrated soil minerals does exist (Ames and Rai 1978). Further, Thibault et al. (1990) reviewed published studies and reported a ^3H sorption coefficient, K_d, range of 0.04 to 0.1 mL g^{-1} in saturated sandy soils. We calculate a K_d of ~0.08-mL g^{-1} for the current ^3H breakthrough curves, which is consistent with that reported by Thibault for saturated sands. Given the unsaturated condition and abundance of clay minerals in the current system, the observed ^3H retardation may not be an artifact of method or design error but a true measure of sorption processes.

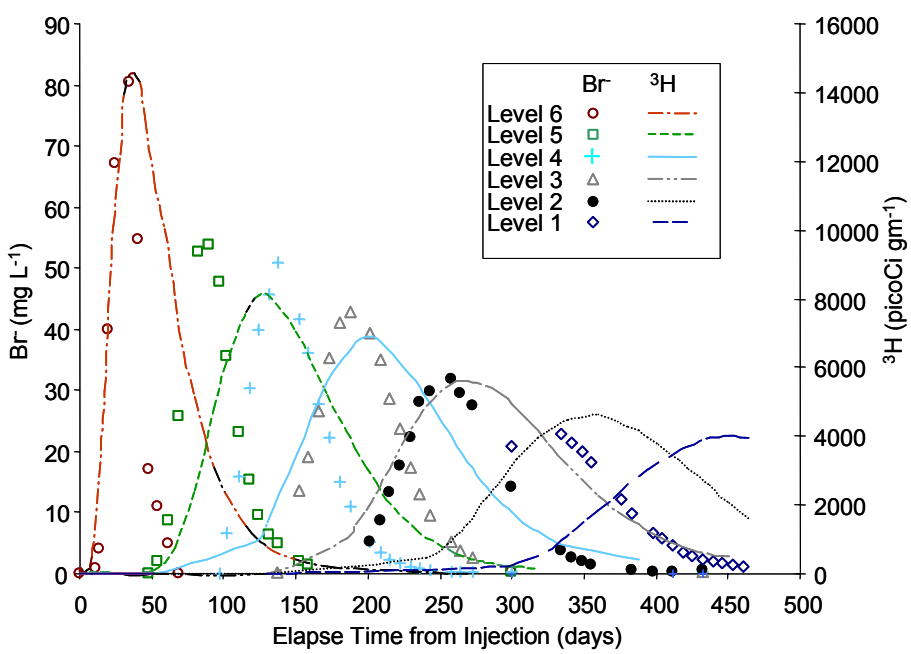

Figure 24. Bromide (Br^-) and tritium (^3H) breakthrough curves.

4.3.3 Carbon-14 Transport

Gas phase carbon-14 (^{14}C) breakthrough curves (Figure 25) display the same characteristic shape as the SF_6 curves (Figure 21) at virtually all levels in the column but lagged, which is consistent with gas-diffusion-dominated transport that is retarded by exchanges with other phases. ^{14}C concentrations at the nearest ports, for example, peaked after approximately one day, as opposed to about an hour for SF_6. ^{14}C was detected in both aqueous and gas phases at sampling ports located ~15-cm above and below the injection plane within 8 h (0.3 days) of the initial 1610 (± 16) microCi injection (Table 22). ^{14}C was dispersed throughout the column within 7 days (Figure 26), with a maximum ^{14}C surface flux (22.37 microCi m^{-2} day^{-1}) occurring within 25 days of the injection (Table 23 and Figure 27a). The surface flux peak was followed by an approximately exponential decline in released activity.

During the initial decline (i.e., from the peak through the steepest portion of the breakthrough curve tail), three reductions and rebounds (fluctuations) of ^{14}C flux were observed (Weeks 59.50, 63.63, and 72.56 in Figure 27). Failure of the mass flow controller to indicate deviation of the headspace ventilation rate resulted in artificial fluctuations of calculated CO_2 flux (Weeks 75 to 85 in Figures 19 and 27b). However, during headspace ^{14}C sampling periods, gas flow rates were validated using a method independent of the mass flow controller. Thus, the occasional loss of flow control is believed to be insignificant for ^{14}C flux calculations. This belief is supported by the apparent lack of correlation between ^{14}C and bulk CO_2 flux during the period of ventilation rate deviation (Weeks 75 to 85 in Figure 27a and b). Barometric pumping can affect ^{14}C flux, but barometric pumping is not apparent when comparing the ^{14}C flux and barometric pressure time series (Figure 27a and c). Phase partitioning effects can also affect ^{14}C flux; the correlation between reductions of ^{14}C and bulk CO_2 flux indicates phase partitioning as the cause of fluctuations in discharged ^{14}C (Table 23 and Figure 27a and b). While gas-phase $^{14}CO_2$ is assumed to diffuse in response to its own concentration gradient, independent of $^{12}CO_2$ and $^{13}CO_2$ partial pressure (Thorstenson et al. 1983), partitioning of $^{14}CO_2$ between aqueous and gas phases is not independent of CO_2 partial pressure (pCO_2). Fluctuations of pCO_2, in response to changes of sediment temperature (Figure 27d) and microbial CO_2 production, shift aqueous/gas phase $^{14}CO_2$ partitioning and consequently ^{14}C diffusion and discharge. This can be conceptualized by the reaction in Equation (13).

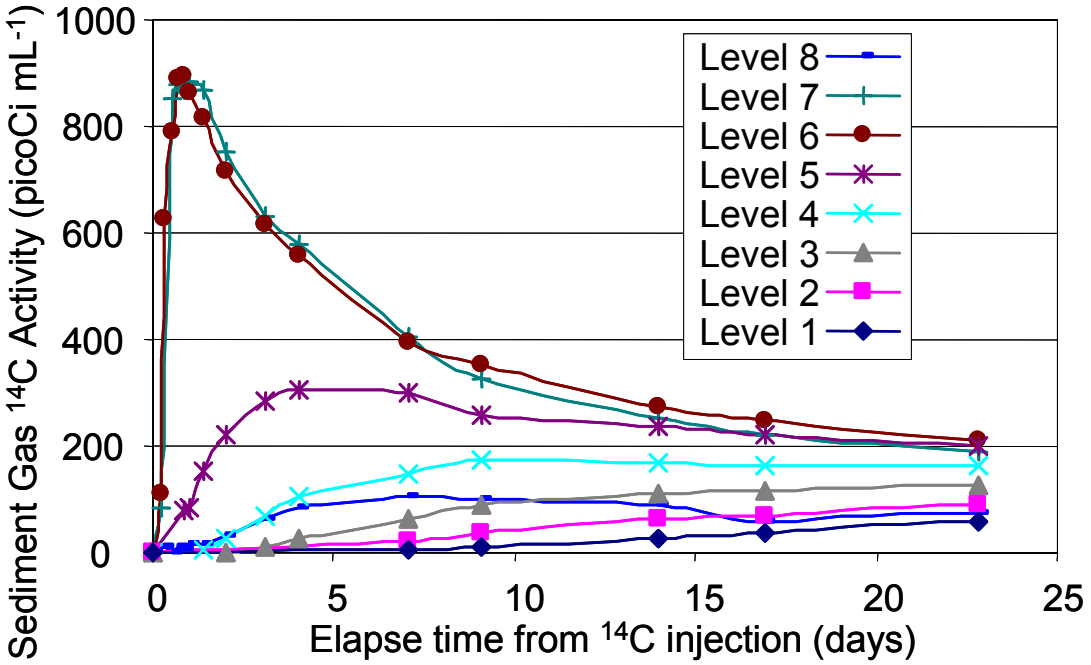

Figure 25. Measured sediment gas ^{14}C breakthrough curves at all eight column levels.

Table 22. Sediment gas and sediment water ^{14}C activity time series.

Elapse Time from ^{14}C Injection (days)	Sediment Gas, picoCi ^{14}C mL^{-1} Gas								Sediment Water, picoCi ^{14}C g^{-1} Water							
	Column Level								Column Level							
	1	2	3	4	5	6	7	8	1	2	3	4	5	6	7	8
0.0	0	0	0	0	0	0	0	0	0	0	0	0	0	0	0	0
0.2						110	85									
0.3						624		12						1168	3663	2
0.5						790	854	1						2245	5076	4
0.7						888	880	10						2937	5394	8
0.8					77	897	866	6					102	3124	5070	17
1.0					84	861	882	16					190	3149	4922	33
1.4				5	154	813	869	13					386	3029	4565	124
2			2	29	221	718	754	34				79	706	2833	3982	281
3			10	69	282	618	630	62			33	224	988	2581	3267	554
4			25	106	306	557	580	86			81	361	1112	2297	2818	761
7	5	20	65	147	299	395	404	104	9	71	244	602	1194	1823	2054	985
9	10	34	87	174	257	355	329	102	20	122	333	668	1146	1596	1801	976
14	25	62	112	167	235	274	254	90	72	233	444	719	1026	1296	1390	882
17	37	71	114	166	219	247	221	87	110	277	470	703	938	1114	1228	813
23	56	90	128	164	198	212	190	74	180	342	502	686	853	1001	984	661
52	91	99	105	110	115	107	84	31	352	435	466	511	541	584	507	326
130	72	70	68	63	59	51	36	13	318	326	326	329	348	279	234	143

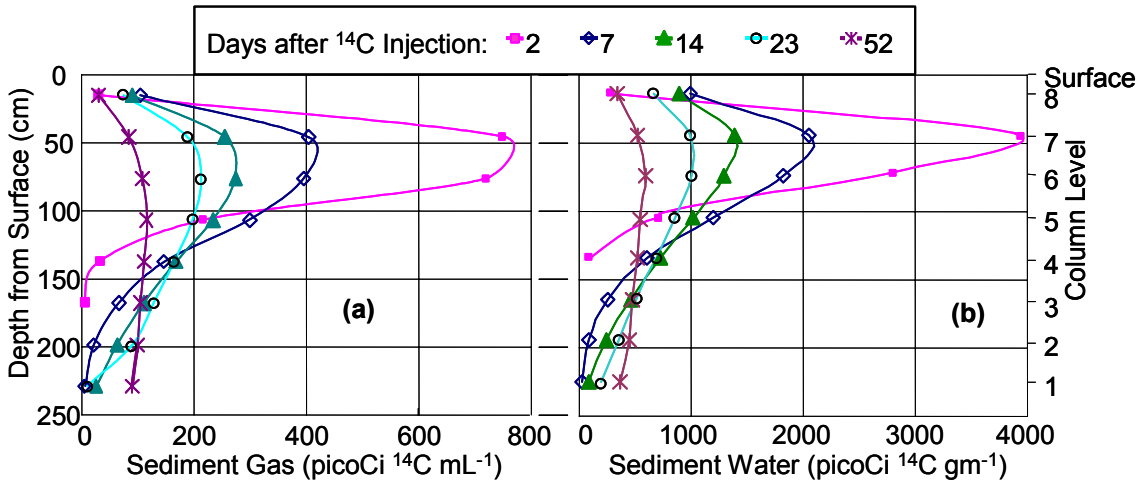

Figure 26. ^{14}C sediment gas (a) and sediment water (b) activity profiles.

Table 23. ^{14}C and bulk CO_2 surface flux data.

^{14}C Elapse Time from Start of Infiltration (weeks)	Elapse Time from ^{14}C Injection (days)	^{14}C Surface Flux (microCi ^{14}C m^{-2} day^{-1})	CO_2 Elapse Time from Start of Infiltration (weeks)	CO_2 Surface Flux (moles CO_2 m^{-2} day^{-1})
56.71	0.0	0.00	57.12	0.20
56.77	0.4	0.08	57.69	0.22
56.80	0.6	0.06	58.13	0.21
56.87	1.1	0.09	59.12	0.19
56.96	1.7	0.55	60.12	0.21
57.07	2.5	2.66	61.26	0.21
57.22	3.6	7.26	62.11	0.20
57.51	5.5	14.29	63.11	0.18
57.86	8.0	20.10	64.11	0.19
58.44	12.1	22.37	65.11	0.19
59.50	19.5	16.20	66.11	0.18
60.41	25.9	20.11	67.11	0.18
60.92	29.4	17.61	68.11	0.18
61.41	32.9	16.58	69.11	0.19
61.91	36.4	14.36	70.11	0.20
62.41	39.9	11.66	71.11	0.19
62.91	43.4	10.82	72.11	0.19
63.63	48.4	7.52	73.11	0.18
64.63	55.4	6.74	74.11	0.15
65.63	62.4	7.67	75.11	0.20
66.63	69.4	7.00	76.11	0.21
67.63	76.4	6.54	77.11	0.17
68.63	83.4	6.37	78.11	0.20
69.63	90.4	5.31	79.11	0.18
70.63	97.4	4.76	80.11	0.18
71.56	103.9	5.14	81.11	0.16
72.56	110.9	3.59	82.11	0.19
73.63	118.4	2.65	83.11	0.20
74.65	125.5	3.31	84.12	0.17
78.63	153.4	2.88	85.12	0.18
82.22	178.5	2.51	86.12	0.15
86.64	209.5	2.08	87.12	0.16
94.29	263.0	1.44	88.12	0.17
106.24	346.6	1.07	89.12	0.15
			90.12	0.16
			91.12	0.16
			92.12	0.15
			93.12	0.14
			94.12	0.15
			95.12	0.16
			97.12	0.15
			98.12	0.12
			99.12	0.11
			100.12	0.14
			101.12	0.16
			102.12	0.11
			103.12	0.14
			104.12	0.14
			105.12	0.18
			106.12	0.22
Intentionally Left Blank: End of Data			106.69	0.17

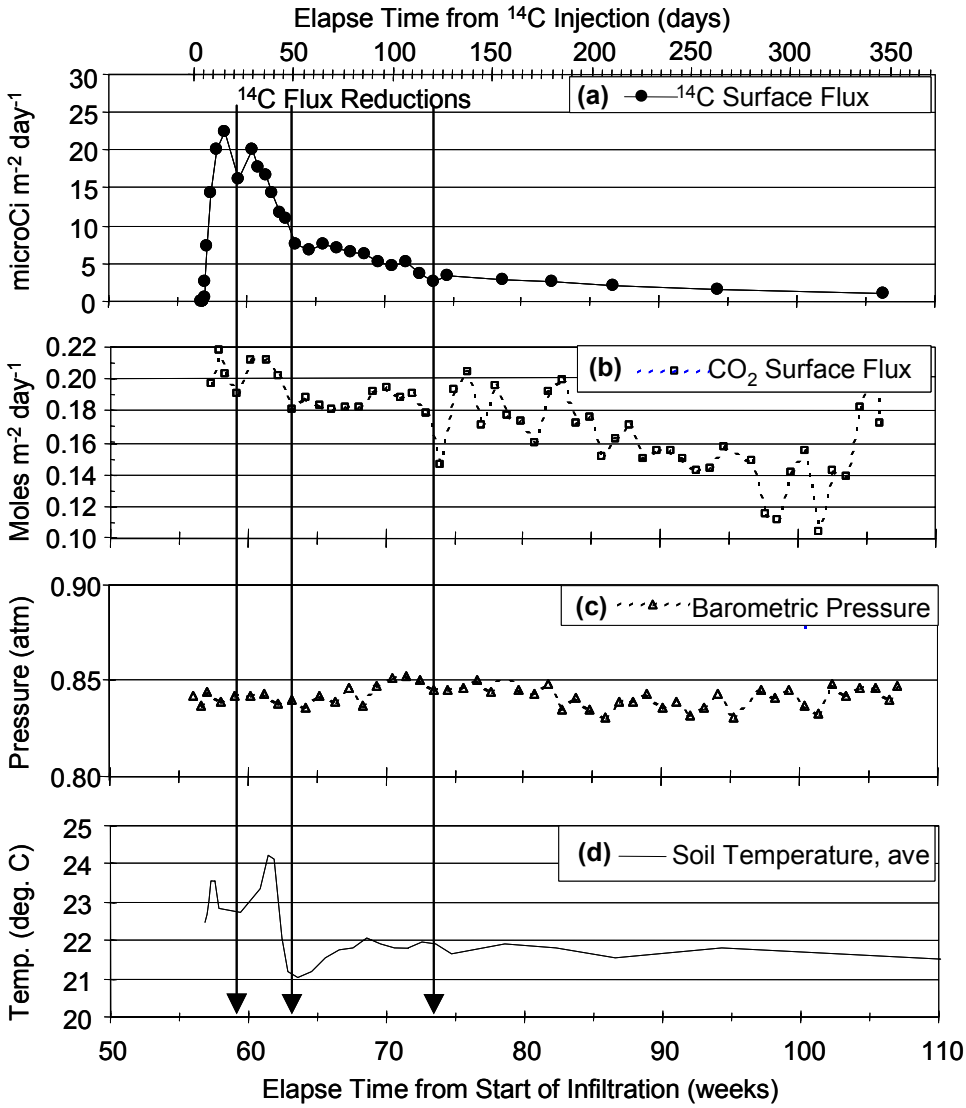

Figure 27. ^{14}C surface flux (a), CO_2 surface flux (b), barometric pressure (c), and average sediment temperature (d) time series.

$$CO_{2(g)} + H_2O \Leftrightarrow H^+ + HCO_3^- \tag{13}$$

As $CO_{2(g)}$ decreases, this reaction moves to the left, consuming H^+ and raising pH. Although gas-phase diffusion of $^{14}CO_2$ is independent of the gas-phase $^{12/13}CO_2$ concentration, the higher solution pH results in more partitioning of gas-phase $^{14}CO_2$ to the aqueous phase. Thus, when the CO_2 partial pressure in the column decreases, there is an increase in $^{14}CO_2$ partitioning to the aqueous phase, a decrease of $^{14}CO_2$ in the gas phase, and consequently a decrease in $^{14}CO_2$ flux out of the column. Because temperature plays a key role in microbial CO_2 production, and therefore CO_2 partial pressure, there is a positive correlation between $^{14}CO_2$ flux and sediment temperature in the column (Figure 27a and d). This relationship between pH and aqueous/gas phase ^{14}C partitioning is consistent with the observation that the aqueous/gas partition ratio (K_{ag}) increases near the top of the column as pH becomes greater and significantly more ^{14}C is contained in the aqueous phase than in the gas phase (Figure 28). As the fraction of injected ^{14}C remaining in the column declines, the response of ^{14}C flux to sediment temperature fluctuations becomes less apparent.

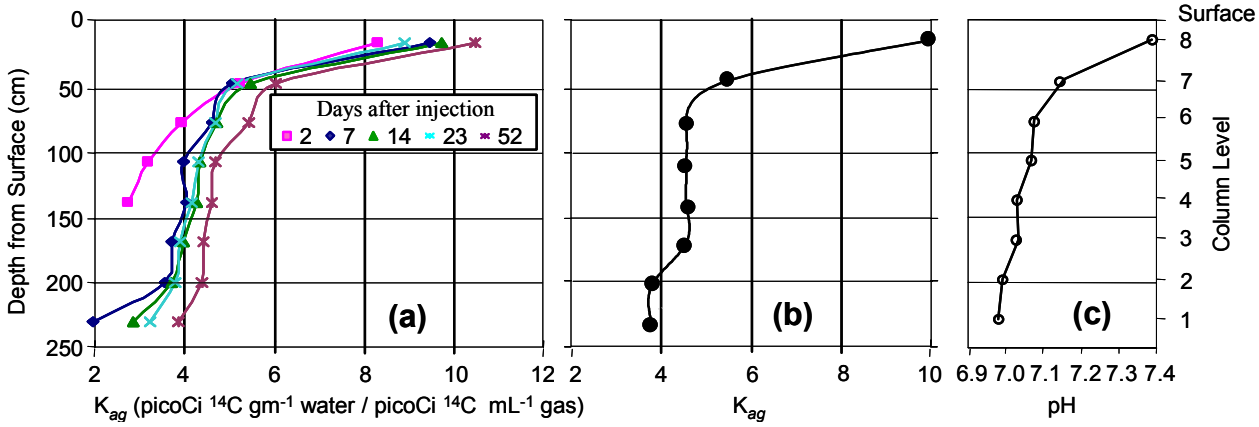

Figure 28. Early time aqueous/gas phase partition ratios (K_{ag}) based on ^{14}C activity partitioning (a) and carbonate equilibrium (b) with pH (c).

The simultaneous appearance of aqueous- and gas-phase activity at each column level (Figure 26) indicates diffusive transport with an aqueous/gas phase exchange. This exchange and solid-phase sorption are expected to retard ^{14}C transport. Therefore, accurate estimates of the aqueous/gas partition ratio, K_{ag}, and aqueous/solid distribution coefficient (K_d) are critical to predicting ^{14}C transport.

We calculate the dimensionless K_{ag} as the ratio of ^{14}C activity per unit volume of sediment water to the ^{14}C activity per unit volume of sediment gas. The aqueous/solid distribution coefficient, K_d, is calculated as the ratio of ^{14}C activity per unit weight of dry sediment to the ^{14}C activity per unit volume of sediment water. Column K_{ag} profiles for Days 2, 7, 14, 23, and 52 following the ^{14}C injection are presented in Figure 28a. These activity-based profiles are consistent with the K_{ag} profile (Figure 28b) calculated for measured pH (Figure 28c) using standard carbonate equilibrium expressions (Langmuir 1997). Therefore, we consider K_{ag} to be well constrained by both measured activity partitioning and measured pH and carbonate concentrations. K_{ag} increases near the top of the column (i.e., surface to Level 7) as pH becomes greater and significantly more $^{14}CO_2$ is contained in the aqueous phase than in the gas phase. Throughout approximately 90% of the column, pH is between 6.9 and 7.1; higher pH occurs only relatively near the surface. Excluding near-surface values, the average K_{ag} is thus approximately 4.5 (± 0.3), during the initial few weeks of the transport study, depending on the column height considered.

On July 29, 2003, approximately one year after the ^{14}C injection, we cored the column to measure the solid phase activity profile (Table 24 and Figure 29). The aqueous and gas phase activity profiles had been measured five days prior to coring (Table 25 and Figure 30). K_d was calculated for column levels not sampled by linear interpolation and/or extrapolation of measured solid phase activities. We calculated the ^{14}C activity mass balance by combining aqueous phase, gas phase, and average solid-phase activities (Table 25) with activities of material removed by sampling, effluent water, and surface flux (Table 26). The total activity removed by sampling represents a small fraction (1.8%) of the total injection; therefore, sampling activities are believed to have had an insignificant effect on ^{14}C movement. An activity mass balance of 93.1% was achieved, with 6.9% of the injected ^{14}C unaccounted for (Figure 31). The inability to account for 100% of the injected activity is believed due to the nonuniformity observed in surface samples (Figure 29), inaccuracies associated with activity interpolation/extrapolation, activity remaining within injection tubing, and cumulative measurement error. The relatively great variation of surface sample activity ($1.2 \times 10^{-4} \pm 33\%$ picoCi g^{-1}) is believed due to the formation of evaporation products (i.e., ^{14}C evaporites) at the sediment/atmosphere interface. The speciation of solid phase ^{14}C was not determined, so the potential contribution of biological ^{14}C uptake to surface sample variation is unknown.

Table 24. Solid phase ^{14}C activity measurements 50 weeks after ^{14}C injection (at end of study).

Core Point	Column Level	Depth from Surface (cm)	Solid Phase Activity (picoCi g^{-1} of dry sediment)
Core 1:	Surface	0.0	133.6
	8	15.2	126.6
	7	45.7	129.0
	6	76.2	119.7
Core 5:	Surface	0.0	80.1
	8	15.2	115.6
	7	45.7	125.2
	6	76.2	121.0
Core 9:	Surface	0.0	89.3
	8	15.2	130.3
	7	45.7	118.7
	6	76.2	Not determined
Core 13:	Surface	0.0	78.8
	8	15.2	122.2
	7	45.7	126.1
	6	76.2	109.9
Core 17:	Surface	0.0	230.7
	8	15.2	126.4
	7	45.7	118.9
	6	76.2	118.6
Core 21:	Surface	0.0	120.4
	8	15.2	121.8
	7	45.7	115.2
	6	76.2	Not determined
Porthole 3:	3	152	130.7
Porthole 2:	2	167	130.1

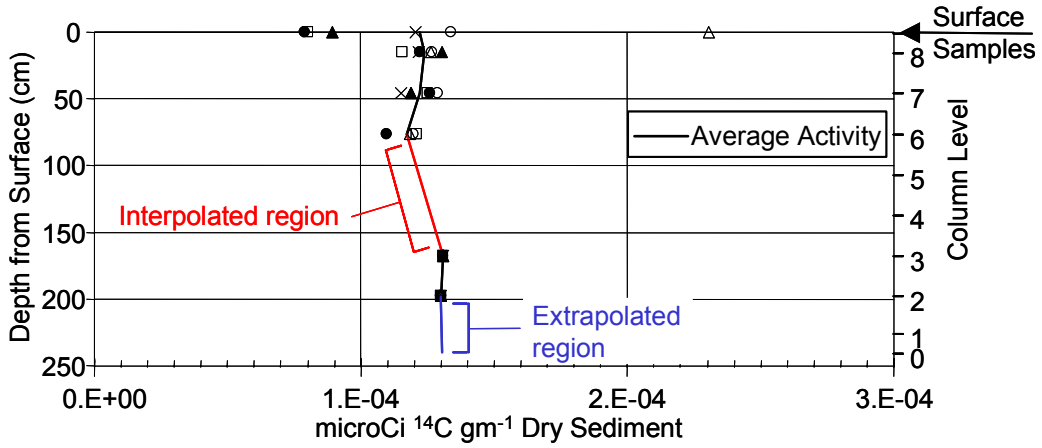

Figure 29. Solid phase ^{14}C activity profile at end of study.

Table 25. Aqueous, gas, and solid phase ^{14}C activity measurements at end of study.

Column Level	Depth from Surface (cm)	Aqueous Phase (picoCi g^{-1} water [7/24/03])	Gas Phase (picoCi mL^{-1} gas [7/24/03])	Average Solid Phase (picoCi g^{-1} dry sediment [7/29/03])
Surface	0.0			122.2
8	15.2	52	6	123.8
7	45.7	88	18	122.2
6	76.2	100	26	117.3
5	106.7	116	30	121.8 (interpolated)
4	137.2	136	34	126.2 (interpolated)
3	167.6	152	38	130.7
2	198.1	167	39	130.1
1	228.6	156	42	130.1 (extrapolated)
OC	243.8	143		130.1 (extrapolated)
OG	243.8	129		

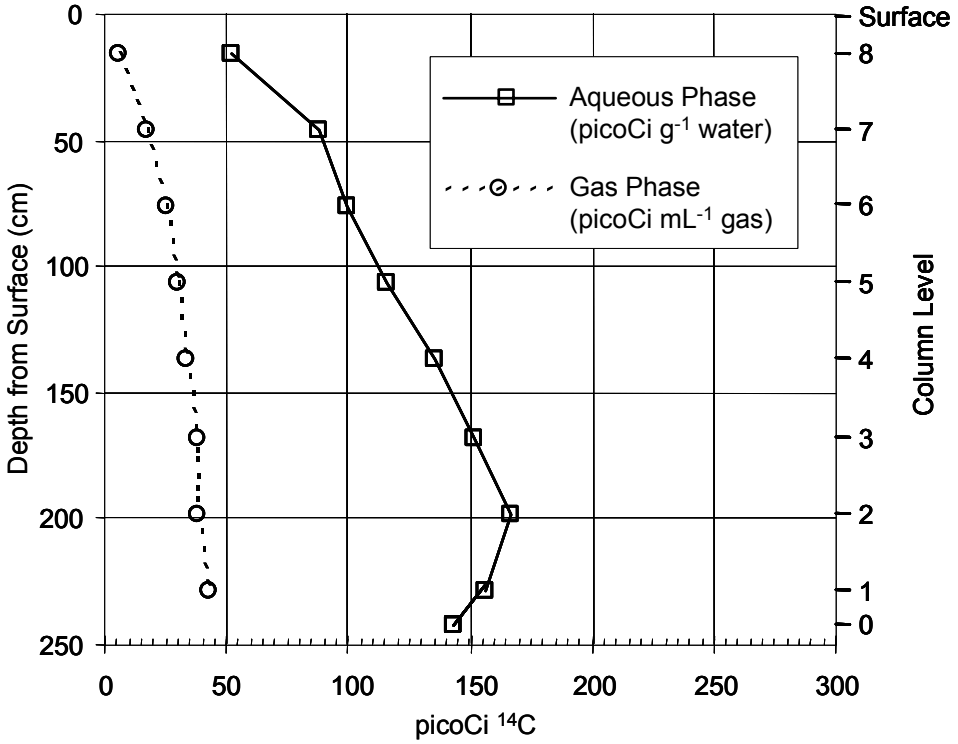

Figure 30. Aqueous and gas phase ^{14}C activity profiles at end of study.

Table 26. ^{14}C activity injected, released, removed, and retained (mass balance determination).

	^{14}C, picoCi ($\times 10^6$)
Activity Injected	1609.6
Released by Surface Flux	1062.8
Released in Effluent Water	60.2
Removed by Water Sampling	4.9
Removed by Gas Sampling	24.0
Retained in Solid Phase	283.6
Retained in Pore Water	50.7
Retained in Pore Gas	12.7
Sum of Released	1151.9
Sum of Retained	347.0
Sum of Released and Retained	1498.8
Activity Mass Balance	93.1%

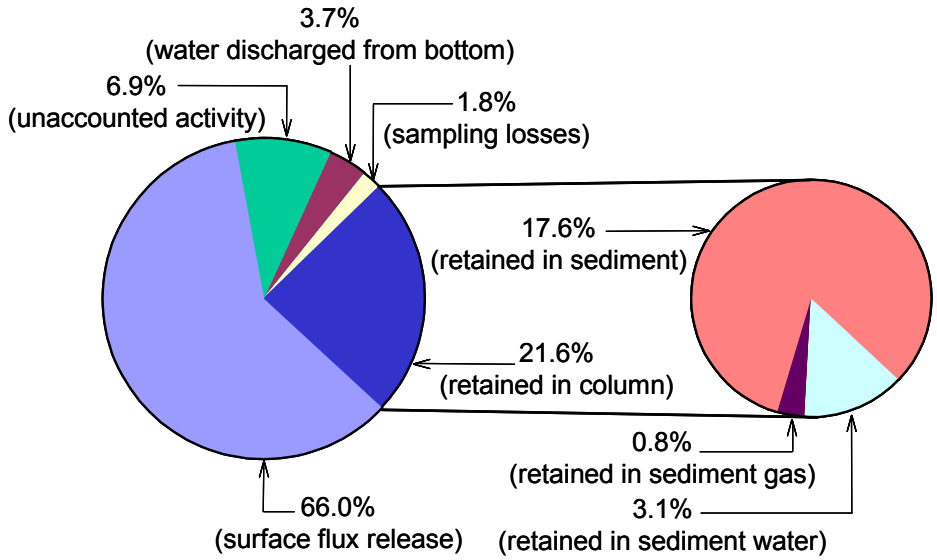

Figure 31. Graphic representation of ^{14}C activity mass balance.

After one year, ^{14}C migration from the column was by surface flux (66.0%) and discharge of water from the bottom of the column (3.7%). Of the total injected ^{14}C, 21.6% was found in the column with 81.5% of the residual sorbed to the solid phase.

After approximately one year, the activity-based K_{ag} profile (Figure 32a) was consistent with that calculated using activity partitioning and carbonate-equilibrium-based approaches ~50 weeks earlier (Figure 28a and b). Measured K_d values range from 0.8 L kg^{-1} near the bottom of the column to 2.4 L kg^{-1} near the top of the column with an average of 1.6 L kg^{-1} (Figure 32a). Much higher K_d values and a dependence on contact time were observed by Allard et al. (1981) who noted increasing adsorption over time in experiments with calcite, obtaining a K_d of 83 mL g^{-1} after six months contact time. However, our range of measured K_d values, after 1 year, is consistent with values (0.1 to 2.0 L kg^{-1}) derived for short-term and small-scale batch and column experiments using SDA sediments (Dicke and Hohorst 1997,[ee] Hull and Hohorst 2001). Similar to K_{ag}, K_d is relatively uniform throughout most of the column but increases near the top of the column, as sediment gas CO_2 concentrations decline and pH becomes greater (Figure 32a and b). These results indicate the need to incorporate effects of nonuniform pH on K_{ag} and K_d into contaminant transport models. For this reason, pH, bicarbonate, and $CO_{2(gas)}$ concentrations at the time of coring are given with activity-based calculations of K_{ag} and K_d (Table 27).

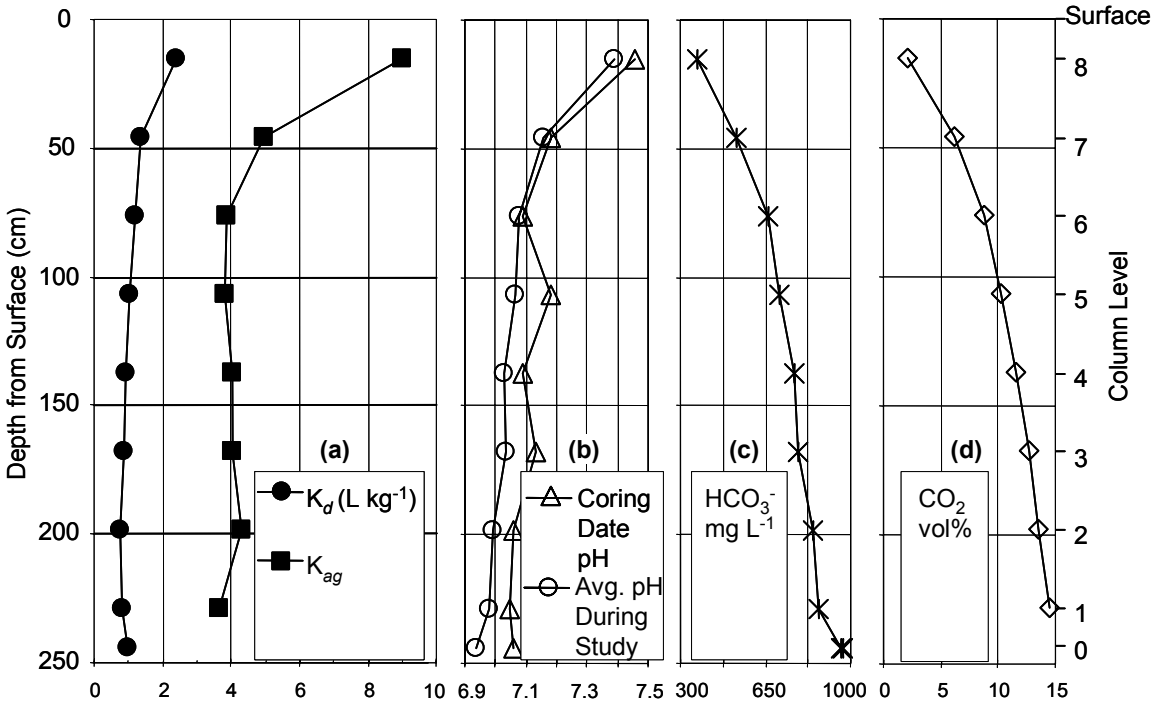

Figure 32. K_d, K_{ag} (a), pH (b), bicarbonate alkalinity (c), and CO_2 (d) profiles at time of coring (end of study).

ee. C*arbon-14 distribution coefficients measured from batch experiments on SDA sediments*, Idaho National Engineering and Environmental Laboratory internal report INEEL/INT-98-00068, EDF-RWMC-1011.

Table 27. K_d, K_{ag}, pH, CO_2, and bicarbonate measurements at time of coring (50 weeks after ^{14}C injection).

Column Level	Depth from Surface (cm)	K_d (L water kg^{-1} sediment)	K_{ag} (unitless)	pH (± 0.3%)	CO_2 vol% (± 2%)	HCO_3^- (mg L^{-1})
8	15.2	2.4	9.0	7.46	2.16	366
7	45.7	1.4	5.0	7.18	6.19	534
6	76.2	1.2	3.9	7.09	8.78	661
5	106.7	1.1	3.8	7.18	10.28	710
4	137.2	0.9	4.0	7.09	11.65	769
3	167.6	0.9	4.0	7.13	12.72	781
2	198.1	0.8	4.3	7.06	13.56	847
1	228.6	0.8	3.7	7.05	14.44	871
OC	243.8	0.9		7.06		964
OG	243.8			7.17		971

5. CONCLUSION

Previous efforts to predict ^{14}C migration from activated metals buried at the SDA were based on contaminant transport models that used transport parameters derived from short-term, bench-scale experiments. Those experiments had limited ability to represent the spatially and temporally varying conditions that affect ^{14}C behavior in the subsurface environment. Our primary goal was to determine ^{14}C transport parameters at spatial-temporal scales, and under geochemical conditions, more applicable to the subsurface environment at the SDA. Our results provide the basis for future modeling efforts to both predict the behavior of $^{14}CO_2$ released from activated metals at the SDA and to determine the ability of transport parameters derived from bench-scale experiments to predict ^{14}C behavior at scales approaching that of the field. Our secondary goal was to identify challenges of operating a near field-scale (meso-scale) unsaturated flow column.

To accomplish our goals, we conducted a set of unsaturated flow experiments to examine the movement of water, gas, conservative tracers, and ^{14}C in a 2.6-m high by 0.9-m diameter meso-scale column of surface sediments similar to those at the SDA. We injected a conservative gas tracer, sulfur hexafluoride, both before and after initiation of hydraulic flow and also injected conservative liquid tracers, bromide and tritium, after reaching a quasi steady-state flow. The transport test involved injection of aqueous 1610 (± 16) microCi ^{14}C-labeled bicarbonate 0.6-m below the sediment surface (i.e., the sediment/atmosphere interface). For ~12 months, we monitored headspace and pore gas CO_2 and O_2 concentrations, sediment surface $^{14}CO_2$ flux, pore gas and pore water ^{14}C migration, pore water chemistry, sediment water content, hydraulic head and/or matric potential, and sediment temperature profiles. During the ^{14}C transport experiment, aqueous/gas ^{14}C partitioning ratios (K_{ag}s) were calculated using two separate methods: aqueous- and gas-phase activity measurements and standard carbonate equilibrium expressions (Langmuir 1997) with measured pH. At the end of the ^{14}C monitoring period, we cored the column and measured solid-phase ^{14}C sorption for calculation of the aqueous/solid ^{14}C partition coefficient (K_d) and ^{14}C mass balance. Results of water content determinations and tracer experiments were used to characterize physical transport parameters affecting ^{14}C movement, including average linear seepage velocity, dispersivity, and aqueous- and gas-phase diffusion coefficients. These physical and phase partitioning parameters (i.e., K_{ag} and K_d) form the basis for subsequent transport modeling efforts.

Our results indicate a relatively constant volumetric water content (28% ± 3%) and an average linear seepage velocity of 0.52 cm day^{-1} during the ^{14}C transport experiment. An initial (packing) volumetric water content of ~10% was indicated by analysis of gravimetric, reflectometer, and sulfur hexafluoride tracer data. Results of post-study bulk density determinations, by sediment cores, are consistent with the average bulk density (1.31 ± 0.05 g cm^{-3}) calculated during column packing. Thus, settling did not occur in the column during these experiments. Sediment porosity (51%) was calculated using average bulk density with an assumed particle density of 2.65 g cm^{-3}.

Bromide (Br^-) breakthrough curves were fit to an analytical solution to the advection dispersion equation for equilibrium transport of a conservative ion slug (CXTFIT2, Toride et al. 1995). Analysis of the Br^- data indicates that hydraulic flow in the column was effectively one-dimensional with an average linear seepage velocity of 0.52 cm day^{-1}, an aqueous diffusion coefficient of 1.8×10^{-5} cm^2 sec^{-1}, and an average hydraulic dispersion coefficient of 5.7×10^{-6} cm^2 sec^{-1} during the transport experiments. Hydraulic dispersivity was effectively negligible, ranging from 0 to 7 mm.

We found transport of the tritium (^3H) tracer to be retarded and calculated a ^3H aqueous/solid partitioning coefficient of ~0.08 mL g^{-1}. Therefore, the ^3H data was not considered in estimation of aqueous transport characteristics in the column. ^3H retardation is significant because ^3H is commonly used as a conservative, nonreactive, tracer in aqueous system studies. Knowledge of the mechanisms causing ^3H retardation would provide understanding critical to use of ^3H as an aqueous tracer in unsaturated flow

studies. We are currently using data from this study to investigate ^{3}H fixation on clays and other common hydrated sediment minerals as the mechanism of retardation. Results of these investigations will be published later.

We performed a least-squares fit of sulfur hexafluoride (SF_6) breakthrough curves for the meso-scale column data using the standard Millington expression (Millington 1959) with an analytical solution to the continuity expression for unidirectional transport. These fits included sets of eight curves, each measured at two different water contents. A good coefficient of determination (0.86) was observed for these fits. Therefore, we conclude that the standard Millington expression with the commonly used *m* value (2.3 or 7/3) adequately describes SF_6 transport in SDA sediments. Additional analysis of these SF_6 tracer data indicated a gaseous diffusion coefficient of 1.1×10^{-1} cm^2 sec^{-1} during the ^{14}C transport experiment.

Gas-phase ^{14}C breakthrough curves at virtually all levels in the column display the same characteristic shape as the SF_6 curves, but lagged, which is consistent with gas-diffusion-dominated transport retarded by exchanges with other phases. $^{14}CO_2$ diffusion, with aqueous/gas phase exchange, allowed ^{14}C to distribute between pore-water and -gas volumes throughout the column within 7 days, with a maximum $^{14}CO_2$ surface flux (22.37 microCi m^{-2} day^{-1}) occurring within 25 days of the ^{14}C injection. After ~12 months, ^{14}C migration from the column was by surface flux (66.0%) and discharge of water from the bottom of the column (3.7%). At this time, 21.6% of the total injected activity was found in the column, distributed between aqueous, gas, and solid phases. Of this residual, 81.5% was sorbed to the solid phase. Mass balance calculations accounted for 93% of the injected ^{14}C activity. The inability to account for all of the injected activity is assumed due to variability of sediment surface sample activities ($1.2 \times 10^{-4} \pm 33\%$ picoCi g^{-1} sediment) resulting from the apparent formation of evaporation products (i.e., ^{14}C evaporites) at the sediment surface, activity remaining within injection tubing, and cumulative measurement error.

Our results indicate that migration of ^{14}C from the meso-scale column was predominantly by diffusive transport to the sediment surface; there was minimal aqueous phase transport or solid phase retention. Given that the column infiltration rate was greater than that estimated for the SDA (Case et al. 2000) and that the sediment type and geometry of the experiment are applicable to the SDA transport problem, we expect that $^{14}CO_2$ migration from activated metals buried at the SDA will also be dominated by gas diffusion with release primarily to the atmosphere rather than to the underlying Snake River Plain aquifer.

During the ^{14}C transport study, pore gas CO_2 concentration (pCO_2) fluctuated in response to changes in sediment temperature, which was the primary control of microbial CO_2 production in the column. We observed a positive correlation between pCO_2 fluctuations and diffusive ^{14}C transport. Though Thorstenson et al. (1983) found gas-phase $^{14}CO_2$ diffusion to be independent of pCO_2, we find that changes in pCO_2 affected pH sufficiently to affect aqueous/gas phase $^{14}CO_2$ partitioning and, therefore, diffusive transport. As a result, even short-term temperature fluctuations caused significant fluctuations in $^{14}CO_2$ flux from the column. Therefore, subsurface temperature should be considered when predicting ^{14}C behavior in the near subsurface where variation of temperature with season and/or climate has the potential to affect ^{14}C phase partitioning and transport.

Microbial consumption of natural organic matter and oxygen with respiration of CO_2 produced an approximately exponential increase in pCO_2 and a corresponding decrease in pH with depth. Typical pH values near the top and near the bottom of the column range from ~7.4 to ~6.9 (±0.3%), respectively. The effect of nonuniform pH is observed in measurements of K_{ag} and K_d. This nonuniformity increased both K_{ag} and K_d near the top of the column, as significantly more ^{14}C was measured in the aqueous phase than in either the gas or solid phase near the top of the column. During the initial few weeks of the transport

study, K_{ag} values ranged from ~9.0 near the top of the column to ~4.0 near the bottom, with an average of 4.5 (±0.3). After ~12 months, the activity-based K_{ag} profile was consistent with that calculated using activity-based and carbonate-equilibrium-based approaches ~12 months earlier. The consistency of activity-based and carbonate-equilibrium-based K_{ag} profile determinations suggests the ability to estimate K_{ag} based solely on carbonate equilibrium. K_d values ranged from 2.4 L kg^{-1} near the top of the column to 0.8 L kg^{-1} near the bottom, with an average of 1.6 L kg^{-1}. Much higher K_d values and a dependence on contact time were observed by Allard et al. (1981). They noted increasing adsorption over time in experiments with calcite, obtaining a K_d of 83 L kg^{-1} after six months contact time. However, our range of measured K_d, after a one year, is consistent with values (0.1 to 2.0 L kg^{-1}) derived for short-term and small-scale batch and column experiments using SDA sediments (Dicke and Hohorst 1997,[ff] Hull and Hohorst 2001). This result suggests that bench-scale measurements are a valid means of estimating aqueous/solid partitioning at the much larger spatial-temporal scales considered in this meso-scale experiment. However, the effect of nonuniform pH on K_d and K_{ag} has not been observed in previous bench-scale experiments. Therefore, bench-scale measurements may be a generally valid means of estimating phase partitioning parameters at larger scales but lack the spatial resolution necessary to observe the effect of environmental variables that control those parameters at larger scales.

We achieved our primary goal, to determine ^{14}C transport parameters at spatial-temporal scales, and under geochemical conditions, applicable to the subsurface environment at the SDA. However, establishing steady-state geochemical and hydraulic conditions did require considerable time. Though the high initial hydraulic flux (~5 L day^{-1} for 84 days) was effective in minimizing the time required to establish unsaturated flow and remove excess dissolved salts from the column, 45 weeks (313 days) of steady hydraulic flux (~1 L day^{-1}) was needed to stabilize the hydraulic potential gradient following the high flux period.

Maintenance of steady-state geochemical conditions (i.e., microbial CO_2 production and pore water pH) was hampered by the long-term depletion of microbial substrate (i.e., easily metabolized organic carbon). Due to rapid $^{14}CO_2$ discharge from the column, long-term changes in pH were insignificant to the ^{14}C transport portion of this study. However, substrate depletion would be a significant factor in designing transport experiments involving extended periods sensitivity to pH (e.g., for uranium). Though measurement of uranium mobility was an initial component of this study, and uranium was injected into the column, the effect of long-term pH changes on uranium mobility could not be observed because aqueous phase uranium was not detected at the lysimeter located ~15-cm below the injection plane. This suggests a uranium K_d greater than 2.5 L kg^{-1}. The extent of uranium migration and the uranium K_d are the focus of ongoing analysis of sediment core samples. These analyses are the subject of a forthcoming publication.

Meso-scale transport experiments are rarely conducted due to their length and considerable cost. However, meso-scale experiments are a valuable means of observing complex behavior under conditions applicable to the field. We demonstrated this value by measuring nonuniformities of K_{ag} and K_d and observing that sediment temperature controls $^{14}CO_2$ diffusion. These measurements and observations were possible because the meso-scale experiment allowed spatially- and temporally-varying conditions, as would occur in the field, to affect ^{14}C behavior. Furthermore, the consistency of the transport parameters we determined with those of previous bench-scale experiments provides increased confidence in the ability of bench-scale methods to predict contaminant behavior in the natural environment. This confidence is invaluable when making regulatory decisions concerning contaminant migration at the SDA and elsewhere.

---

ff. C*arbon-14 distribution coefficients measured from batch experiments on SDA sediments*, Idaho National Engineering and Environmental Laboratory internal report INEEL/INT-98-00068, EDF-RWMC-1011.

6. REFERENCES

Allard, B., B. Torstenfelt, and K. Andersson, 1981, "Sorption Studies of $H^{14}CO_3^-$ on Some Geologic Media and Concrete," *In* J. G. Moore (ed.) Scientific Basis for Nuclear Waste Management III, Plenum Publ. Corp, New York, p. 465–472.

Ames, L. L., and D. Rai, 1978, *Radionuclide Interactions with Soil and Rock Media*, Volume 1: Processes Influencing Radionuclide Mobility and Retention, Element Chemistry and Geochemistry, and conclusions and Evaluation, EPA 520/6-78-007A, prepared for the U.S. Environmental Protection Agency by the Pacific Northwest Laboratory, Richland, Washington.

Bond, W. J., B. N. Gardiner, and D. E. Smiles, 1982, "Constant-Flux Absorption of a Tritiated Calcium-Chloride Solution by a Clay Soil with Anion Exclusion," *Soil Science Society of America Journal*, Vol. 46, No. 6, pp. 1133–1137.

Case, M. J., A. S. Rood, J. M. McCarthy, S. O. Magnuson, and B. H. Becker, 2000, *Technical Revision of the Radioactive Waste Management Complex Low-Level Waste Radiological Performance Assessment for Calendar Year 2000*, INEEL/EXT-2000-01089, Idaho National Engineering and Environmental Laboratory, Bechtel BWXT, Idaho Falls, ID.

Hartsough, P. S., W. Tyler, J. Sterling and M. Walvoord, 2001, "A 14.6 kyr Record of Nitrogen Flux from Desert Soil Profiles as Inferred from Vadose Zone Pore Waters," *Geophysical Research Letters*, Vol. 28, No. 15, pp. 2955–2958.

Hull, L. C. and C. W. Bishop, 2003, *Fate of Magnesium Chloride Brine Applied to Suppress Dust from Unpaved Roads at the INEEL Subsurface Disposal Area*, INEEL/EXT-01-1173, Idaho National Engineering and Environmental Laboratory, Bechtel BWXT, Idaho Falls, ID.

Hull, L. C. and F. A. Hohorst, 2001, *Transport Models for Radioactive Carbon Dioxide at RWMC*, INEEL/EXT-01-00894, Idaho National Engineering and Environmental Laboratory, Bechtel BWXT, Idaho Falls, ID.

James, R. V. and J. Rubin, 1986, "Transport of Chloride-ion in a Water-Unsaturated Soil Exhibiting Anion Exclusion," *Soil Science Society of America Journal*, Vol. 50, No. 5, pp. 1142–1149.

Langmuir, D., 1997, *Aqueous Environmental Geochemistry*, Prentice-Hall, Inc., New Jersey.

McCarthy, J. M., B. H. Becker, S. O. Magnuson, K. N. Keck, T. K. Honeycutt, 2000, *Radioactive Waste Management Complex Low-Level Waste Radiological Composite Analysis*, INEEL/EXT-97-01113, Bechtel BWXT Idaho, LLC, September 2000.

Millington, R. J., 1959, "Gas Diffusion in Porous Media," *Science*, Vol. 130, pp. 100–102.

Olmsted, J. and G. M. Williams, 1994, "Chemistry: The Molecular Science," Mosby, p. 221.

Thibault, D. H., M. I. Sheppard, and P. A. Smith, 1990, *A Critical Compilation and Review of Default Soil Solid/Liquid Partition Coefficients, K_d, for Use in Environmental Assessments*, AECL-10125, Whiteshell Nuclear Research Establishment, Pinawa, Manitoba, Canada.

Thorstenson, D. C., E. P. Weeks, H. Haas, and D. W. Fisher, 1983, "Distribution of Gaseous $^{12}CO_2$ in the Sub-Soil Unsaturated Zone of the Western U.S. Great Plains," *Radiocarbon*, Vol. 25, pp. 315–346.

Toride, N., F. J. Leij, and M. T. van Genuchten, 1995, *The CXTFIT Code for Estimating Transport Parameters from Laboratory or Field Tracer Experiments*, Version 2.0. Research Rep. 137. U.S. Salinity Lab., USDA, Riverside, CA.

Walvoord, M. A., F. M. Phillips, D. A. Stonestrom, R. D. Evans, P. C. Hartsough, B. D. Newman and R. G. Striegl, 2003, "A Reservoir of Nitrate Beneath Desert Soils," *Science*, Vol. 302, No. 5647, pp. 1021–1024.

Appendix A

Measurement Accuracy

Appendix A

Measurement Accuracy

Associated Error Analyses

The relative accuracy of methods used for chemical and radiological determinations is expressed in terms of precision (i.e., uncertainty) and bias. The uncertainty associated with each measurement type is presented as the percent average-difference of standard and/or average duplicate sample measurements, Equation (A-1). Cumulative uncertainty and errors associated with standard laboratory procedures are not addressed.

$$\%\text{Uncertainty} = \left(\frac{\frac{\sum d_i}{n_i}}{\text{Value}} \right) * 100 \qquad \text{(A-1)}$$

where

%Uncertainty	=	percent of average difference
$\sum d_i$	=	sum of the differences between each measurement and the either the measurement-standard or the average value for duplicate samples (absolute values)
n_i	=	the number of observations (i.e., samples)
Value	=	the measurement-standard value or the average duplicate-sample value.

Aqueous Measurements

Uncertainties associated with aqueous species analyses are contained in laboratory reports and are not presented here. However, electro neutrality % errors are given in Table 16. Iron and carbonate were assumed to have a negligible charge balance contribution. Alkalinity was considered to be as bicarbonate in change calculations. Conductivity and pH measurement uncertainties were established in relation to duplicate sample analysis of conductivity and pH standards, Table A-1. The accuracy of alkalinity measurements may be accessed using an alkalinity standard. This assessment was not performed because turbidity and/or chlorine interference were not expected. Instead, we choose to determine the method error and compare it to the published error. The comparison was performed by blind analysis of duplicate samples. A maximum deviation from the mean of 10.3 ppm was measured. The HACH Company defines the method error as 10 ppm.

Table A-1. Alkalinity, electrical-conductivity, and pH measurement uncertainty.

	Performance Samples/ Sampling Days	% (±)
Alkalinity	15/1	10 ppm
Electrical-Conductivity (average)	10/193	1%
PH	43/286	0.3%

Gas Concentration Measurements

The uncertainty of SF_6 analysis is given by the manufacturer to be 1%. A duplicate sample was used as an additional measure of method precision. The duplicate was made using ~0.3 cm^3 of the certified SF_6 gas standard (99.995%) in a Tedlar bag containing ~3 L of UHP nitrogen gas. Five measurements produced a mean concentration of 107 ppmv. The uncertainty associated with SF_6 measurements is presented as the percent average-difference of each duplicate sample and the average duplicate sample value. The accuracy of O_2 measurements is established in reference to room air at 209,500 ppmv O_2 (i.e., the performance evaluation sample or PES). The uncertainty associated with O_2 measurements is presented as the percent average-difference of each calibrated PES measurement and the actual PES value.

The accuracy of CO_2 measurements is established in reference to low and high range PESs. The uncertainty associated with CO_2 measurements is presented as the percent average-difference of each calibrated PES measurement and the actual PES value. SF_6, O_2, and CO_2 measurement uncertainties are given in Table A-2.

Table A-2. SF_6, O_2, and CO_2 concentration measurement uncertainty.

Species	Performance Samples/ Sampling Days	% (±)
SF_6	15/1	1
CO_2 low range	76/500	1
CO_2 high range	76/500	1
O_2	76/500	0.2

Isotope Measurements

Accuracy of the liquid scintillation counting is often obscured by matrix quenching effects. To put it simply, quenching is an interference that can bias measurement results and prevent direct comparison of samples to standards. To minimize quenching and enable sample and standard comparisons, isotope standards were prepared in a matrix consistent with sample matrices. Nevertheless, quenching was found to introduce a low measurement bias. Analysis of carbon-14 (^{14}C) and tritium (^{3}H) standards produced measurements of 5.9% and 16.2% below actual values, respectively. Method bias was also verified by independent laboratory analyses (INTEC/CCP). ^{14}C and ^{3}H activities presented here were corrected for measurement biases of 5.9 and 16.2%, respectively. Background activities were considered insignificant and were not included in activity calculations. The uncertainty associated with ^{14}C and ^{3}H measurements is presented as the percent average-difference of duplicate sample measurements and the average sample measurement. Measurement uncertainties are presented along with background activities in Table A-3.

Table A-3. Sample background activities.

	Carbon-14 (microCi g^{-1})	Tritium (microCi g^{-1})
Sediment Water Background	4E-06	8E-06
Head Gas Background	4E-06	5E-06
Sediment Gas Background	4E-06	5E-06
Dry Sediment Background	6E-06	not determined
Uncertainty (31 samples/ 177 days)	1%	1%

Carbon-14 Soil Surface Flux Measurements

The uncertainty of ^{14}C surface flux determinations is related to headspace flow (ventilation) rate, CO_2 trap flow rate, and CO_2 trap efficiency measurements. The uncertainty of each aforementioned measurement is presented to aid interpretation of the ^{14}C surface flux data, Table A-4. The uncertainty introduced into surface flux determinations by headspace and CO_2 trap flow measurements is presented as the average percent-difference of individual and the average flow ratios (i.e., Q_{total}/Q_{trap} in Equation (A-2)). The uncertainty of CO_2 trap efficiency measurements is presented as the average percent difference of individual and average trap efficiency determinations (i.e., this is the CO_2 trap efficiency term in Equation (1)). Additionally, the uncertainty of headspace ventilation rates is presented as the average percent-difference of individual and average headspace ventilation rate measurements. The period of flow control loss, during the later portion of the transport study, is not included in these calculations. ^{14}C activity flux, F_{14c}, is given by

$$F_{14C} = \frac{Act_{Sample} * Q_{Total} * m_{Trap}}{\Delta t * Q_{Trap} * \left(\frac{EFF}{100\%}\right)} \tag{A-2}$$

where

Act_{Sample}	=	activity per gram of aliquot, microCi g^{-1}
C	=	conversion factor, 4.5E-7 microCi disintegration^{-1} min^{-1}
DPM	=	disintegration's per minute (liquid scintillation counts)
m_{Sample}	=	mass of aliquot, g
F_{14C}	=	^{14}C flux, microCi day^{-1}
m_{Trap}	=	total mass of CO_2 trap solution, g
Q_{Total}	=	total headspace flow (ventilation), liters min^{-1}
Q_{Trap}	=	CO_2 trap flow (split of total headspace flow), liters min^{-1}
Δt	=	period of CO_2 trapping, days
EFF	=	CO_2 trap efficiency, %.

Table A-4. Uncertainty of ^{14}C surface flux measurements.

	Flow Ratio, Q_{total}/Q_{trap} (L min^{-1} Total/ L min^{-1} Trap)	Headspace Ventilation Rate (L min^{-1})	Trap Efficiency (%)
Measurements/Days	12/182	12/182	12/182
Mean Value	1.83	7.06	96.0
Uncertainty (%)	2.7	0.1	1.4

Appendix B

Sample Preparation Procedures

Appendix B

Sample Preparation Procedures

Head Gas Samples (CO_2 Trap System) for Liquid Scintillation Counting (LSC)

You will need the 2M NaOH solution to be analyzed, concentrated nitric acid, ethanol, nano-pure DI water, 20 mL scintillation vials w/lids, a 250 mL disposable beaker, a disposable dropper, paper wipes, analytic balance, fume hood, and appropriate PPE.

1. Prep CO_2 trap samples for ^{14}C counting

    a. Label sample vial lids (do not mark the vial's sides).

    b. Place 5g (± 0.01) of DI water in the sample vial, record weight.

    c. Place a 5g (± 0.01) aliquot of 2 M NaOH trap solution (sample) in the vial, record sample weight.

    d. Add 10 mL of Ultima-Flo AF scintillation cocktail to sample aliquot in vial. To prevent phase separation, do not exceed this final molarity (i.e., 0.5 M NaOH).

    e. Tightly cap vial and wipe clean with ethanol.

2. Prep CO_2 trap samples for tritium counting

    a. Label sample vial lids (do not mark the vial's sides).

    b. Place a 2.9 g (± 0.01) aliquot of 2 M NaOH trap solution (sample) in the vial, record sample weight.

    c. In a fume hood, add 500 µL of concentrated nitric acid (HNO_3) to NaOH sample in vial. This will lower the pH to ~2, thus liberating CO_2 from solution. Caution: CO_2 gas will be violently liberated. Leave vial in fume hood until the liberated CO_2 gas has been evacuated from the solution and the vial. Limit sample evaporation by leaving lid on vial loosely.

    d. Add 13 mL of Ecolume scintillation cocktail to the acidified sample. To prevent phase separation, do not exceed 3.0 g of aqueous sample per 13 mL of cocktail.

    e. Tightly cap vial and wipe vial clean with ethanol.

Soil Water Samples for LSC and Kinetic Phosphorescence Analysis (KPA)

You will need a 30 mL disposable syringe for each lysimeter sampled, a 0.2 µm syringe filter for each syringe, 5 M NaOH, 10% nitric acid, ethanol, paper wipes, 20 mL scintillation vials w/lids, 50 and 300 µL disposable pipetters (one each), analytic balance, fume hood, and appropriate PPE.

1. Prep soil water samples for ^{14}C counting

    a. Label sample vial lids (do not mark the vial's sides).

b. Place 2 g of 5 M NaOH in a sample vial. This is done to trap CO_2 in solution.

c. Immediately after sample extraction, place an 8 g (± 0.01) aliquot of sample water in vial, record weight.

d. Add 10 mL of Ultima-Flo AF scintillation cocktail to the sample in vial. To prevent phase separation, do not exceed this final molarity (i.e., 0.5 M NaOH).

e. Tightly cap vial and wipe clean with ethanol.

2. Prep soil water samples for tritium counting

a. Label sample vial lids (do not mark the vial's sides).

b. Place a 2.9 g (± 0.01) aliquot of sample water in a vial, record weight.

c. In a fume hood, add 50 µL of 10% HNO3 to the sample water. This will lower the pH to ~2, thus liberating CO_2 from solution. Leave vial in fume hood until the liberated CO_2 gas has been evacuated from the solution and the vial. Limit sample evaporation by leaving lid on vial loosely.

d. Add 13 mL of Ecolume scintillation cocktail to the acidified sample. To prevent phase separation, do not exceed 3.0 g of aqueous sample per 13 mL of cocktail.

e. Tightly cap vial and wipe vial clean with ethanol.

3. Prep soil water samples for uranium analysis by KPA

a. Label sample vials.

b. Place 10 g of sample water in a vial (± 0.01).

c. In a fume hood, add 100 µL of 10% HNO_3 to sample water. This will lower the pH to ~2 (assures U suspension). Record pre- and post-acidification dilution volumes for future calculation of concentration.

Note: To make respective background and blank samples, substitute surrogate vadose zone and DI water for the sample aliquots above.

Soil Gas Samples for LSC

You will need a 1 L Tedlar gas bag for each gas port sampled, a 20 mL disposable syringe, a 16 G to 25 G hypodermic needle, a 200 mL gas syringe, 0.5 M NaOH, 10% nitric acid, ethanol, paper wipes, 20 mL scintillation vials w/lids, a 50 µL disposable pipetter, analytic balance, fume hood, and appropriate PPE.

1. Prep of soil gas sample bag and collection of sample

a. Label sample bag.

b. Weigh empty sample bag, record weight.

c. Inject ~16 cm^3 of 0.5 M NaOH into the empty sample bag. Make sure that the bag's valve is closed. Take care not to pierce the side of the bag opposing the septa.

d. Reweigh the sample bag and NaOH, record weight.

e. Draw exactly 200 mL of gas sample into the gas syringe and transfer to the sample bag immediately.

f. Add free space to the bag by adding ultra pure nitrogen gas (~500 mL). Take care not to over fill and rupture the bag.

g. Tighten and lock the bag's valve, then shake the sample bag vigorously until small NaOH droplets are dispersed about the bag's inner surfaces (~15 s).

h. Let CO_2 dissolve into NaOH droplets for a minimum of 15 min before removing sample aliquots. The sample solution will evaporate through the bag material at a relatively high rate, so do not store sample in bags.

2. Prep soil gas samples for ^{14}C and tritium counting

a. Label sample vial lids (do not mark the vial's sides).

b. Weigh empty vials with lids, record weight.

c. Open the bag's valve and lightly squeeze:

(1) 10 g (± 0.01) of the sample/NaOH solution into a vial labeled for ^{14}C counting.

(2) 2.9 g (± 0.01) of the sample/NaOH solution into a vial labeled for tritium counting. After adding sample to each vial, immediately place the lid on vial and tighten.

d. Weigh the vials and contents, record weight.

e. Add 10 mL of Ultima-Flo AF scintillation cocktail to the vials for ^{14}C counting. Wipe the vials clean with ethanol.

The soil gas tritium samples require one additional step:

f. In a fume hood, add 125 µL of concentrated HNO_3 to the sample water. This will lower the pH to ~2, thus liberating CO_2 from solution. Leave vial in fume hood until the liberated CO_2 gas has been evacuated from the solution and the vial. Limit sample evaporation by leaving lid on vial loosely.

g. Add 13 mL of Ecolume scintillation cocktail to the vials for tritium counting. To prevent phase separation, do not exceed 3.0 g of aqueous sample per 13 mL of cocktail.

h. Wipe vials clean with ethanol.

Carbon-14 and Tritium Performance Evaluation Samples (PES)

We are using a ^{14}C standard solution (HOHOC14ST021202; 506.60 d/m/g; analysis date 11/19/96), a tritium standard solution (Amersham TRY68, 11.87 microCi/g; analysis date 6/1/81), 5M NaOH, 10%

nitric acid, ethanol, paper wipes, 2 0 mL scintillation vials w/lids, 50 and 1000 µL disposable pipetters (one each), surrogate ground water, analytic balance, fume hood, and appropriate PPE.

1. Prep of soil water and gas trap ^{14}C PES

   a. Label sample vial lid (do not mark the vial's sides).

   b. Place 5 g (± 0.01) of 2 M NaOH in a sample vial.

   c. Add 2 g (± 0.01) of surrogate vadose zone water (DI H_2O for gas trap standards) to the vial.

   d. Add 2.9 g (± 0.01) of ^{14}C and 0.005 g (± 0.001) of tritium standards to the vial, record weight and activity of standards added.

   e. Add 10 mL of Ultima-Flo AF scintillation cocktail to this 1M solution. To prevent phase separation, do not exceed this final NaOH molarity.

   f. Tightly cap vial and wipe clean with ethanol.

2. Prep of soil water tritium PES

   a. Label sample vial lid (do not mark the vial's sides).

   b. Place 2.9 g (± 0.01) of ^{14}C and 0.005 g (± 0.001) of tritium standards in the vial.

   c. In a fume hood, add 50 µL of 10% HNO_3 to the vial, record weight, age, and activity of standards used. Leave vial in fume hood until CO_2 gas has been evacuated from the solution and the vial. Limit sample evaporation by leaving lid on vial loosely.

   d. Add 13 mL of Ecolume scintillation cocktail to the acidified solution. To prevent phase separation, do not exceed 3.0 g of aqueous sample per 13 mL of cocktail.

   e. Tightly cap vial and wipe vial clean with ethanol.

   Note: To make respective PES background/blanks, substitute surrogate vadose zone or DI water for the standard solutions above.

Preparation of Sediment Samples for Carbon-14 and Uranium Analysis

You will need the sediment samples to be analyzed, 2M HCl, 2M NaOH, 125 mL serum bottles with septa and crimp lids, 5 mL test tubes, tweezers, 250 mL disposable beakers, ~2 mL disposable transfer pipettes, 30 cc disposable syringes, 0.2 um syringe filters, ethanol, nano-pure DI water, 20 mL scintillation vials w/lids, paper wipes, analytic balance, fume hood, plastic-backed plotter paper, shaker table, metal drying pans, sample drying oven, 26G hypodermic needle connected to a ridged tube (~30 mm long with 1 mm ID) and appropriate PPE.

1. Extract ^{14}C and uranium from sediment samples.

   An aggregate gaseous, aqueous, and solid phase ^{14}C activity is measured for bulk sediment samples. The contribution of gaseous ^{14}C to aggregate activity is assumed to be insignificant. Delineation of aqueous and solid phase activity is achieved by splitting each sample prior to analysis. Aggregate aqueous and solid phase ^{14}C activity is measured and sample water content is

determined. Knowledge of *in situ* aqueous phase activity is combined with sample water content to subtract aqueous phase activity from the aggregate. Split water contents are determined, simultaneously with procedures below, using a drying oven in a fume hood and standard laboratory techniques.

a. Label serum bottles.

   (1) Add 20 mL (± 0.1) of 2M HCl to serum bottle.

   (2) Add 5 mL (± 0.1) of 2M NaOH to test tube.

b. Place 5 mL test tubes in serum bottles, resting upright against the bottle's side.

c. Tare balance for serum bottle, septa, and crimp lid.

d. Add 5 g (~40 mm long by ~10 mm diameter piece) of sediment sample to acid in serum bottle (immediately affix septa and crimp lid to prevent escape of CO_2 gas), record weight of sediment sample. Note: Slightly shaping sediment sample will facilitate adding the sediment to the serum bottle.

e. Place serum bottle on shaker table and mix slurry for 24 h at 100 RPM.

f. Check serum bottle gas pressure to verify that CO_2 gas is fully dissolved in base. Hold index finger over the ridged tubing end, containing a water droplet, and insert the hypodermic needle into the bottle septa. Slowly move index finger to vent the tubing and watch water droplet movement. Continue mixing until gas pressure is negative (i.e., water droplet moves toward the bottle). Do not allow water droplet to be drawn from the ridged tubing into the serum bottle.

2. Prep carbon-14 samples for scintillation counting

a. Label scintillation vial lids for ^{14}C counting (do not mark the vial's sides).

b. Place 5 g (± 0.01) of DI water in the scintillation vials.

c. Transfer 5 g ^{14}C samples (i.e., the NaOH solution in serum bottle test tubes) to scintillation vials using transfer pipettes.

d. Add 10 mL of Ultima-Flo AF scintillation cocktail to the ~10 g sample aliquot. To prevent phase separation, do not exceed an aliquot molarity of 1M NaOH (0.5 final molarity).

e. Tightly cap vial, shake vial to mix contents, and wipe vial clean with ethanol.

3. Prep uranium samples for analysis

a. Label scintillation vials for uranium samples.

b. Remove and discard empty test tube from serum bottle using tweezers.

c. Decant sediment-acid slurry supernatant into disposable 250 mL beaker.

d. Draw supernatant into a 30 cc syringe. Do this soon after decanting to minimize evaporative loss.

e. Dispense filtered supernatant from syringe into scintillation vials for analysis.